EXPLORING AN UNSTRUCTURED LATTICE REPRESENTATION FOR CARBONATE RESERVOIR CHARACTERIZATION

A Thesis

by

ASHWIN LAKSHMI PASUMARTI

Submitted to the Office of Graduate and Professional Studies of
Texas A&M University
in partial fulfillment of the requirements for the degree of

MASTER OF SCIENCE

Chair of Committee,	Michael J. King
Co-Chair of Committee,	Akhil Datta-Gupta
Committee Member,	Michael Pope
Head of Department,	Dan Hill

August 2014

Major Subject: Petroleum Engineering

ABSTRACT

Carbonates for flow simulation purposes are typically characterized as grid-blocks of varying permeability, with a finer grid employed where heterogeneity is greatest. However, this manner of representation is more suited to sandstone reservoirs, as transport in carbonate reservoirs is usually far more un-geometric due to the complex types of carbonate rock pore-spaces. Far from simply flow between inter-granular pore-spaces, diagenetic processes produce carbonate reservoirs with permeability heterogeneity mainly within three distinct but yet interacting geologic features - Matrix, Vugs and Fractures – very often with each feature occurring at various length scales. This project will explore the merits of an unstructured means of representing carbonates via a lattice-network of pore-volumes connected in space in directions and connectivity properties driven by the rock fabric, as opposed to being limited by the rigid geometry of grid-blocks. With this goal in mind, some aspects related to a lattice-based characterization will be studied.

Firstly, the geologic context that motivates a non-grid based approach to carbonate reservoir modeling will be discussed in the literature review. Secondly, convective and diffusive calculations on a grid will be compared to their equivalents on a lattice in order to establish the applicability of the lattice-system. Convective time-of-flight on a grid is calculated using Pollock's method, while an approximation using the average pore-volumes between nodes will be employed on the lattice. Diffusive time-of-flight on a grid is populated using the Fast Marching Method (FMM), whereas Dijkstra's Algorithm

is more appropriate for a lattice. Thirdly, μ-CT-scan data of a rock sample from an outcrop will be used to build an equivalent unstructured lattice-representation of the media at that length scale, and explored for convective and diffusive flow properties. This will be performed by using the AVIZO Suite to first binarize the μ-CT data into pore space and non-pore space, and then skeletonizing it to convert the pore-space into an unstructured set of nodes – carrying volumes – and bonds – each carrying a mean length and radius. These properties will then be used to calculate the transmissibility and diffusive time-of-flight across each bond. Once these are known, convective and diffusive floods can be initiated and the appropriate responses studied to learn about the rock properties. This project is envisaged also as laying the groundwork for a long term goal of unstructured lattice-based carbonate reservoir characterization.

DEDICATION

To my Mother

for her *infinite* love, care, concern and prayer.

ACKNOWLEDGEMENTS

First and foremost, I would like to thank my committee chair, Dr. Michael King, who has been an immense mentor and an inspiration for me with his keen insight. I am very grateful for the numerous hours he dedicated as we pondered over the results, often late into the evenings. I hope to be able to adopt his eye-for-detail and the sheer enthusiasm for his work into my career.

I would like to also thank Dr. Akhil Datta-Gupta for his guidance and for leaving an indelible mark upon me with his all of his classes. Every lecture truly felt illuminating. I must certainly thank Dr. Michael Pope and late Dr. Wayne Ahr as well; whose Carbonate Reservoirs class changed my perspective towards the subject and geology altogether.

A special thanks as well to all the members of the Model Calibration and Efficient Reservoir Imaging (MCERI) research group for all the great conversations – intellectual or light-hearted – that both broadened my mind and humbled me in equal measure. Finally, this journey was all that much more fun because of all the enduring and meaningful friendships I've had the privilege of making along the way.

The support of Qatar National Research Funds (QNRF) for the project titled "Geology-Based Reservoir Model Building for Carbonate Reservoirs" (Project Number: B648A) and Dr. Anuj Gupta's research group at Texas A&M University, Qatar (TAMUQ) is acknowledged.

NOMENCLATURE

c_t	Total compressibility; psi^{-1};
h	Thickness; ft;
k	Permeability; md;
$\vec{\vec{k}}$	Permeability tensor; md;
q	Darcy flux; RB/day;
r	Radius of investigation; ft;
t	Time; hours;
p	Pressure; psi;
A	Cross sectional area; ft^2;
L	Length; ft;
V_p	Drainage volume; ft^3;

Subscripts

i	Index
w	Well

Greek variables and operators

α	Hydraulic diffusivity, ft / $\sqrt{hrs}$
τ	Diffusive time of flight, $\sqrt{hrs}$
μ	Fluid viscosity, cp

ϕ	Porosity
∇	Gradient

Abbreviations

PV	Pore volume
PSS	Pseudo Steady State
FMM	Fast Marching Method
MP	Match Point

TABLE OF CONTENTS

Page

Page

LIST OF FIGURES

Page

Page

Page

Page

Page

Page

Page

LIST OF TABLES

Page

CHAPTER I

INTRODUCTION

Carbonate reservoirs continue be important as they contain nearly 50% of the world's conventional hydrocarbon reserves (Palaz and Marfurt 1997). Several of the largest reservoirs in the world, both in size and quantity of oil reserves, formed in carbonate rocks, as summarized in Schlumberger's (2007) survey (Figure 1). Carbonate reservoirs are typically characterized by immense geologic and petrophysical heterogeneity with the most challenging reservoirs displaying nearly unpredictable connectivity even at multiple length-scales. Since permeability-porosity relationships are almost non-existent in a spatial sense, and only relationships within an individual rock-fabric for a given length-scale (from an extremely broad spectrum) are relevant, classical methods of characterization grafted from those applied to Sandstone reservoirs often fail or are poorly suited to carbonate reservoirs (Lucia et al. 2003). This chapter will briefly discuss the complexities of carbonate pore-spaces in the hope of suggesting that a grid-based approach is too simplistic and also to motivate a lattice-based and unstructured representation as more naturally suited to flow in carbonate rocks. Subsequently, conventional means of characterizing carbonates will also be discussed. Next, some of the earlier work done on pore-network extractions on μ-CT scan data will be mentioned. Finally, the approach and the deliverables of the subsequent chapters will be discussed.

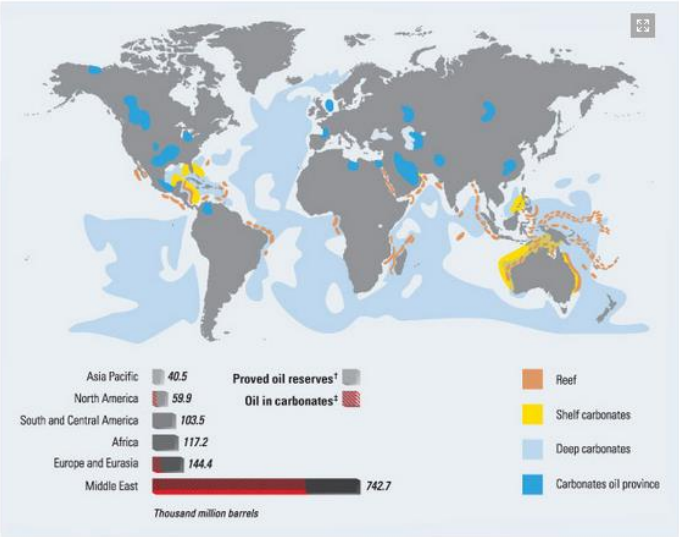

Distribution of oil from carbonate sources around the world.

† BP Statistical Review, 2007

‡ Schlumberger Market Analysis, 2007

Figure 1 – Shows the occurrences of conventional carbonate reservoirs around the world and their importance owing to their OOIP. (Schlumberger 2007)

1.1 Literature Review

In this section, we briefly review aspects of carbonate geology in particular that relate to the complexity of pore-spaces, and the multiple-length scales of connectivity inherent in carbonate rocks. This is not meant as an exhaustive study of the carbonate reservoir characterization, but rather to suggest that while the grid-block representation is a natural method for sandstones, it is inadequate for carbonates. By highlighting the unstructured-ness of connectivity in carbonate rocks, we wish to motivate the idea of a lattice-based approach to characterizing carbonates. A few of the conventional means of characterizing the heterogeneity in carbonates, as well as some of the work done on extracting pore-networks from CT and μ-CT scan data are discussed.

1.1.1 Brief Overview of Carbonate Geology and the Complexity of Pore-Spaces

Carbonate rocks are distinct from siliciclastic rocks in several ways. Most importantly, they are not composed of grains and minerals originating from the process of weathering and the subsequent transport and deposition of parent rocks. Instead, carbonate basins form in regions where biologically-originated matter, (e.g., skeletal remains, fecal pellets, etc.) are deposited. After deposition, the pore spaces may then undergo immense size and shape changes via *in-situ* biological activities as organisms eat and excrete the material or burrow and bore through the rock. Changes may also occur through chemical reactions resulting in dissolution, cementation, recrystallization or replacement of the carbonates. Carbonate rocks are extremely susceptible to this entire process of transformation – termed diagenesis – that both creates and destroys different types of pore-spaces and connectivity (Ahr 2008). It is the diagenetic transformations that make carbonate rock pore-spaces starkly and uniquely different from siliciclastic rocks.

Sandstone rocks have primarily inter-particle/granular porosity. In inter-particle porosity, pore-shapes are essentially the "negative" of sedimentary grains (Choquette and Pray 1970), and can conveniently be thought of as a continuum. Studies of the geometry of pore-spaces in sphere packs and sandstone rocks have shown that they are similar and concluded that interparticle porosity relates well geometrically to the particle sizes and orientation (texture and fabric). This in turn allows interparticle-porosity to be very closely related to permeability (Berg 1970). The grain size and the level of sorting in the grains together can thus be used as a good indicator of the permeability. Essentially, heterogeneity in a sandstone reservoir stems from regions of differing rock

texture/fabric, each of which can be related to its own porosity value, which in turn is a good predictor of bulk permeability. Additionally, since the *type* of porosity in sandstones is homogenous throughout the reservoir, this means that permeability estimate`s from any small volume, e.g., a core sample, can be conveniently used to represent much larger volumes, so long as the rock texture is the same ("rock type" in the language of reservoir models). Overall, these facts serve to justify the use of gridblocks as a very natural method of upscaling and representing flow in sandstones.

Carbonate pore-spaces on the other hand are not always interparticle. Post deposition, diagenesis creates additional and complex types of pore spaces/connectivity, even across several length-scales in carbonate rocks. Essentially, heterogeneity in carbonate rocks stems not only from differing texture and fabric, but from the type (and length-scale) of pore-spaces as well. The complexity of pore-spaces has led to several classification schemes identifying the different types of pore-spaces.

It has been suggested that all hydrocarbon producing carbonates carry one or some combination of as many as 8 porosity types (Longman 1981):

1. Intra-granular/Intra-particle: Porosity *inside* a constituent particle.
2. Inter-granular/Inter-particle: Porosity *between* particles.
3. Dissolution *enhanced* Inter and Intra granular/particle: porosity that is formed by dissolution that acts around the boundary of the pore-spaces described above.
4. Inter-crystalline: Porosity between crystals formed as a result of chemical diagenesis. (most commonly in dolomite)

5. Moldic: Porosity formed by grains/constituents being leached out completely by (selective) dissolution.
6. Vuggy Porosity: irregular holes of a size visible to the naked eye formed by dissolution of the rock. These can range in length-scales, from Micro-Vugs formed by dissolution of crystals to often even the size of large caves.
7. Fracture Porosity: Porosity formed as a result of *in-situ* stress-fields causing the rock to fail in defined directions.
8. Stylolitic Porosity: porosity formed as dissolution occurs at thin seams between beds of rock under pressure.

A seminal classification scheme (Figure 2) that highlights nearly all the different kinds of porosities observed in carbonate rocks and grouped based on their fabric selectivity was created by (Choquette and Pray 1970). This classification scheme introduces several additional pore types, such as fenestral and burrow, several of which create connectivity at multiple length scales.

A far simpler classification of carbonate pore-types was suggested by (Lucia 1995) which characterized porosity as either vuggy or inter-particle. Lucia suggested that all connectivity in carbonate rocks was some combination of non-touching Vugs (vuggy porosity) feeding inter-particle pores, or via Vugs that are themselves touching at point contacts (Figure 3).

A new classification scheme that built upon the pore-types identified by the Choquette and Pray was attempted by (Lønøy 2006). This classification scheme further divides

each pore-type based on the size of the pores and the type of distribution in pore-sizes obtained and suggests the strength of the porosity-permeability relationship for sub-classification (Figure 4).

Since carbonate rocks carry pore-types similar to sandstones only at deposition, and a different classification or "rock-typing" scheme, according to three genetic end-member processes that create and destroy pore-spaces has been suggested (Ahr 2008). This is shown in Figure 5. In effect, he suggests that as the impact of diagenetic and/or fracturing processes becomes greater, pore-space connectivity becomes that much more unstructured and further away from the interparticle and intra-particulate nature of porosity that depositional processes create.

In siliciclastic rocks, diagenesis is limited to compaction and expulsion/absorption of water, which reduces the size of the inter-particle porosity. For carbonate rocks however, diagenetic processes are almost exclusively responsible for creating *new* types of pore spaces and increasing/destroying the existing porosities in the rock. Figure 6 shows the principle environments, summarized by (McIlreath and Morrow 1990) in which the influx of water occurs and initiate different diagenetic processes. This figure also highlights the potential length-scales of connectivity associated with each environment, where pore-spaces can range from the size of caves in the mixing zone, to the size of small burrowing animals in the beach environment. Considering that a carbonate rock may be put through several environments in its burial history, several stages of diagenesis can occur and create or destroy connectivity at multiple length-scales.

In summary, fluid flow in carbonate rocks occurs through interacting networks of vugs, fractures and the matrix itself, each with potentially several associated length scales, and thus not strictly through a continuum.

Figure 7 highlights these three features in a photograph of an outcrop of the Jebel Fuwairit Beach Bar Complex, courtesy of Dr. Anuj Gupta's group at Texas A&M University, Qatar Campus. This figure highlights a parallel set of fractures that connects large pore-volumes to each other, as well as a distribution of vugs that can act as storage receptacles both into the matrix and into the fractures themselves. The outcrops in this region are considered to be analogous to many of the Carbonate Reservoirs in the Middle-East, particularly the Jurassic Arab and Triassic Khuff formations (Gupta and Poppelreiter 2010), and are very suggestive of the immense heterogeneity associated with them. A comparison of thin sections from the matrix portion of the carbonate rock (Figure 7) with a sandstone rock is shown in Figure 8. This indicates that the porosity in sandstone is only intergranular, whereas in the carbonate rock it is both intergranular and intra-granular, as well as a potentially connected system of micro-vugs and inter-crystalline porosity, even within the matrix. Figure 2 and Figure 3 together show how length-scales of connectivity in carbonate rocks can be tremendously heterogeneous.

Thus the porosity and permeability in carbonate rocks isn't easily studied using a continuum approach. A μ-CT scan of the matrix portion of the rock from Qatar will be studied in Chapter 3. This discussion highlights how a grid-based representation is not naturally useful for understanding fluid flow in carbonate rocks.

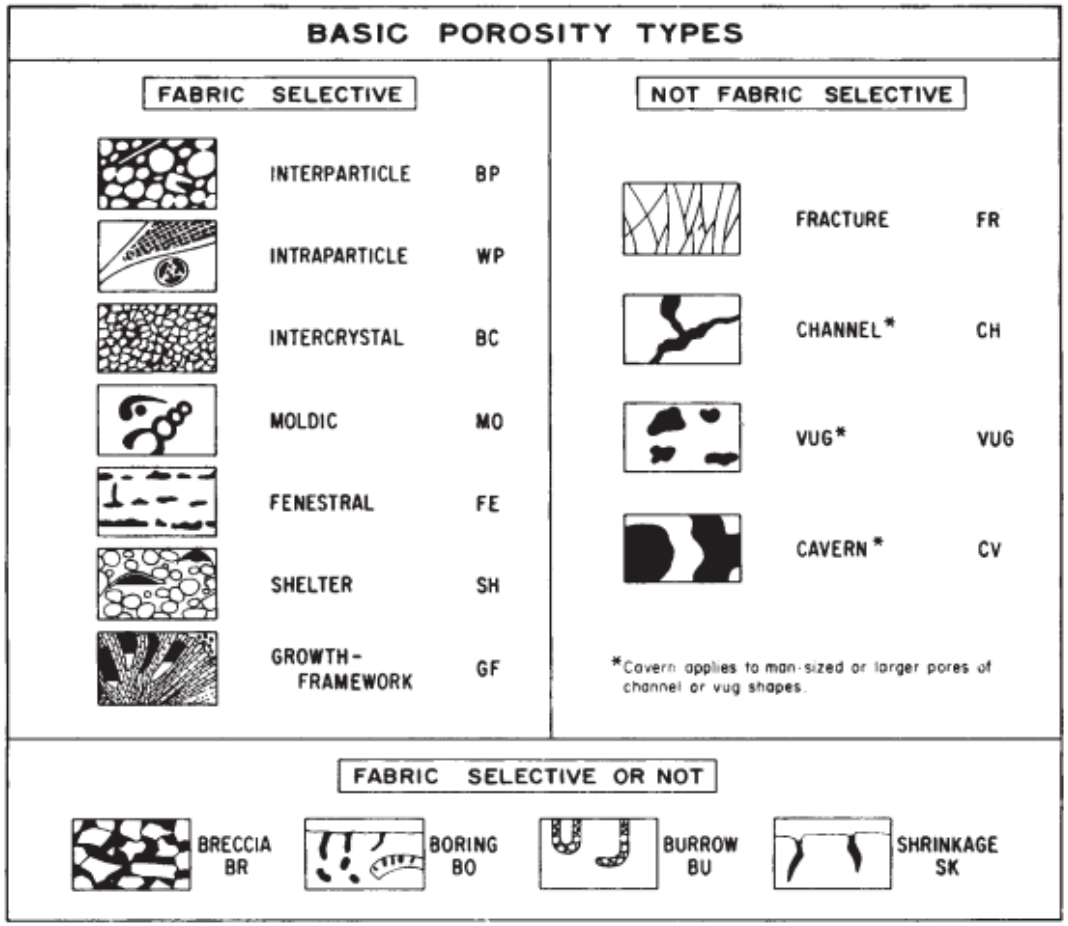

Figure 2 – Shows the Choquette and Pray classification of all the different kind of pore-spaces found in carbonate rocks (Choquette and Pray 1970).

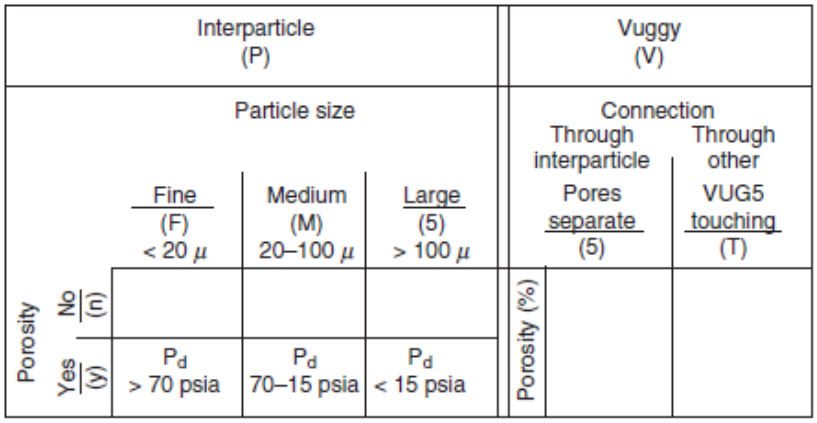

Figure 3 – Shows Lucia's classification of carbonate pore-types into two simple categories of vuggy porosity and inter-particle porosity.

Pore Type	Pore Size	Pore Distribution	Pore Fabric	R^2
Interparticle	Micropores (10–50 μm)	Uniform	Interparticle, uniform micropores	0.88
		Patchy	Interparticle, patchy micropores	0.79
	Mesopores (50–100 μm)	Uniform	Interparticle, uniform mesopores	0.86
		Patchy	Interparticle, patchy mesopores	0.85
	Macropores (>100 μm)	Uniform	Interparticle, uniform macropores	0.88
		Patchy	Interparticle, patchy macropores	0.87
Intercrystalline	Micropores (10–20 μm)	Uniform	Intercrystalline, uniform micropores	0.92
		Patchy	Intercrystalline, patchy micropores	0.79
	Mesopores (20–60 μm)	Uniform	Intercrystalline, uniform mesopores	0.94
		Patchy	Intercrystalline, patchy mesopores	0.92
	Macropores (>60 μm)	Uniform	Intercrystalline, uniform macropores	0.80
		Patchy	Intercrystalline, patchy macropores	
Intraparticle			Intraparticle	0.86
Moldic	Micropores (<10–20 μm)		Moldic micropores	0.86
	Macropores (>20–30 μm)		Moldic macropores	0.90
Vuggy			Vuggy	0.50
Mudstone microporosity	Micropores (<10 μm)		Tertiary chalk	0.80
			Cretaceous chalk	0.81
		Uniform	Chalky micropores, uniform	0.96
		Patchy	Chalky micropores, patchy	

*Partly based on Choquette and Pray (1970) and Lucia (1983, 1995, 1999). Porosity-permeability coefficients of determination (R^2) are based on samples from the present study.

Figure 4 – Shows Lønøy 's classification scheme taking into account both the different types of porosity and the length-scale of the porosity (Lønøy 2006).

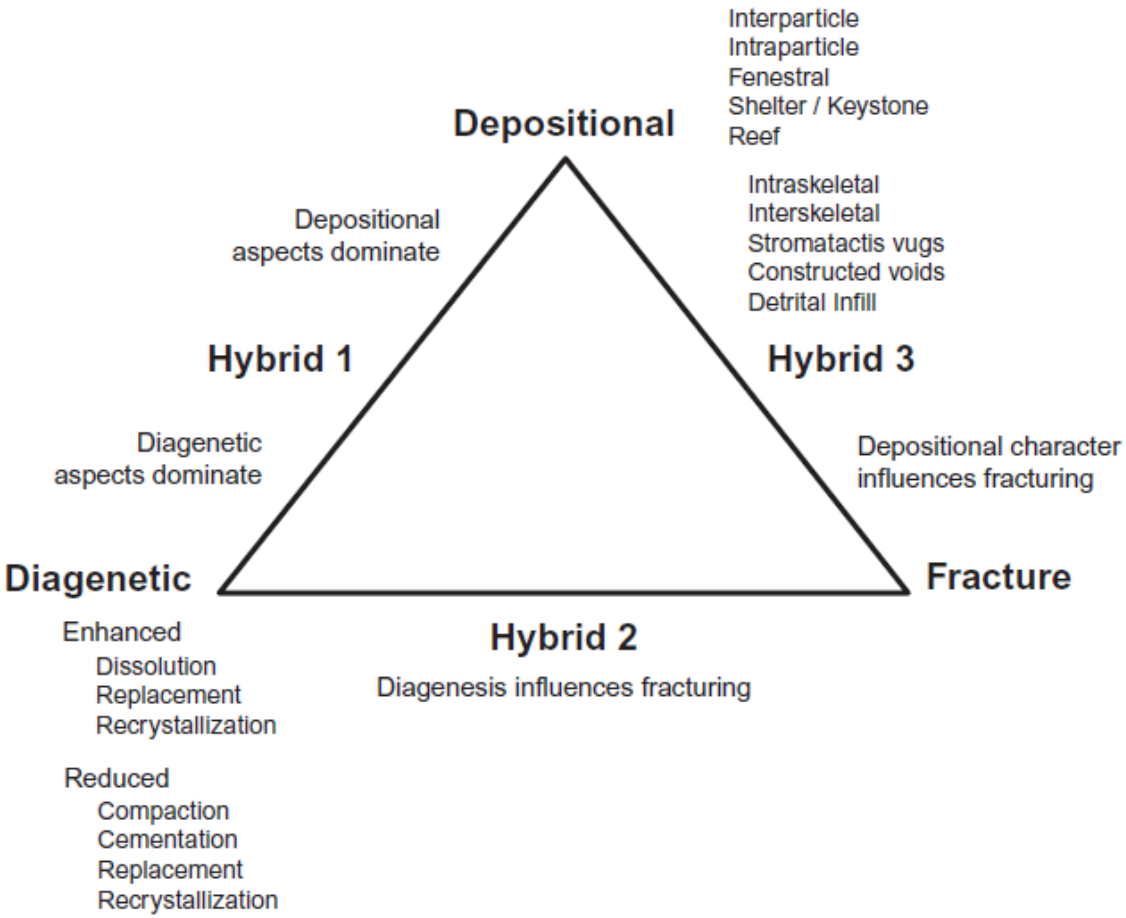

Figure 5 – Shows Ahr porosity classification scheme and suggests that porosity in carbonate rocks be classified based on how strong the influence is of three end-member groups (Ahr 2008)

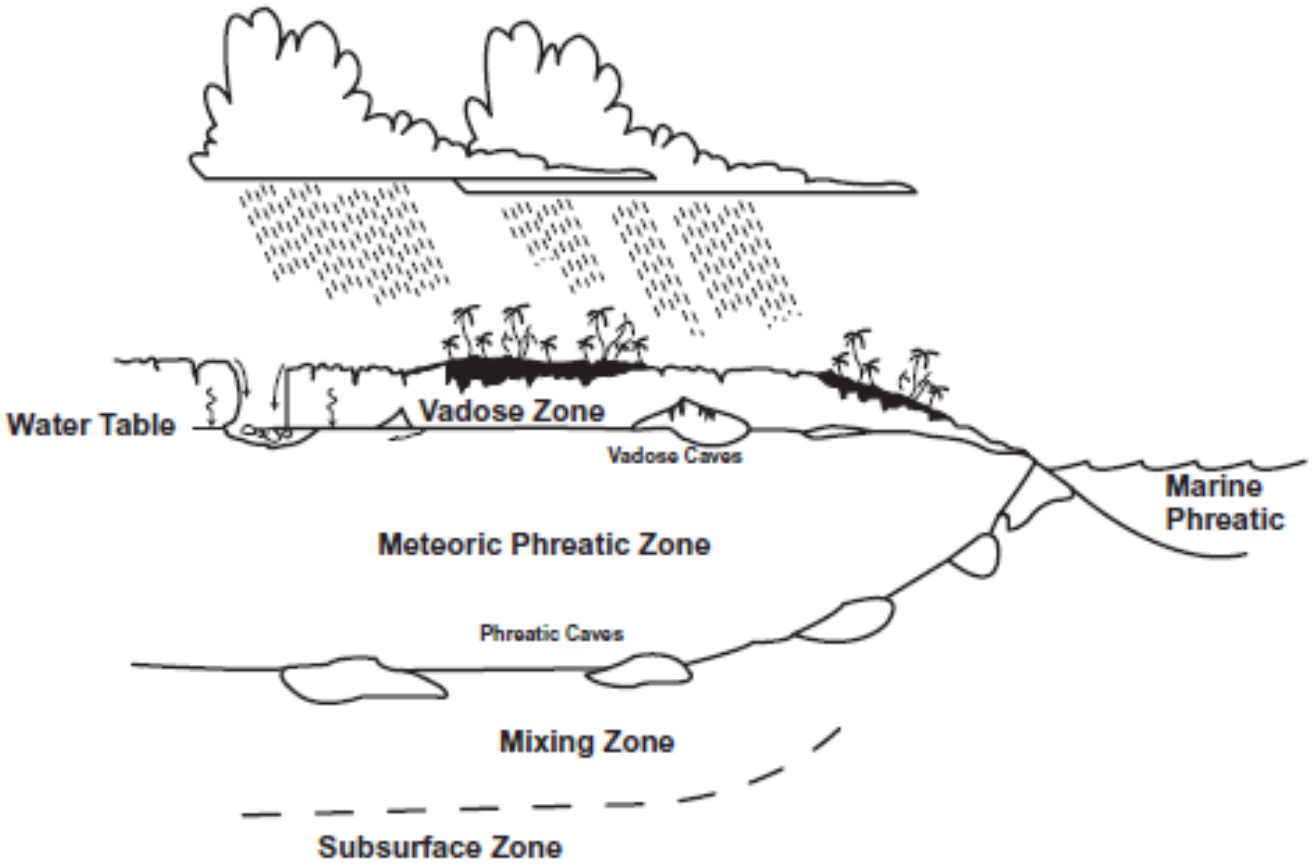

Figure 6 – Shows the principle diagenetic environments where carbonates undergo transformation (McIlreath and Morrow 1990).

.

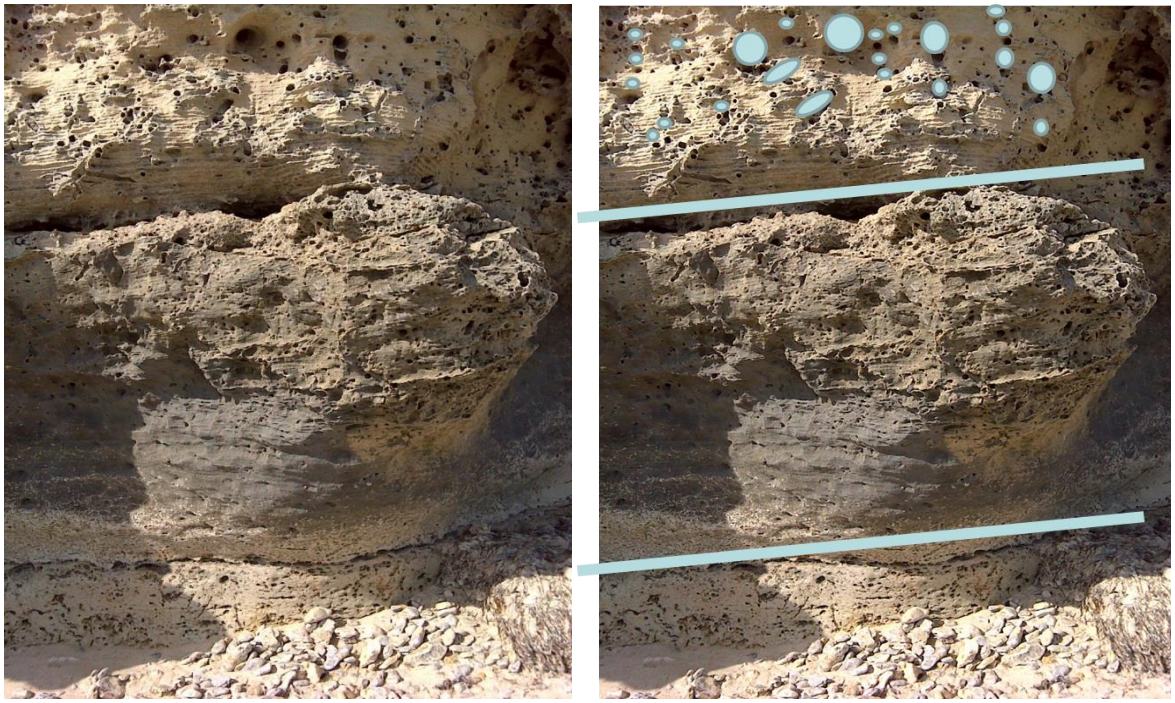

Figure 7 – A particularly complex carbonate rock that was subjected to intense diagenesis, producing a dense mesh of vugs and a parallel set of fractures. This is a photograph of the Jebel Fuwairit Beach Bar Complex in Qatar.

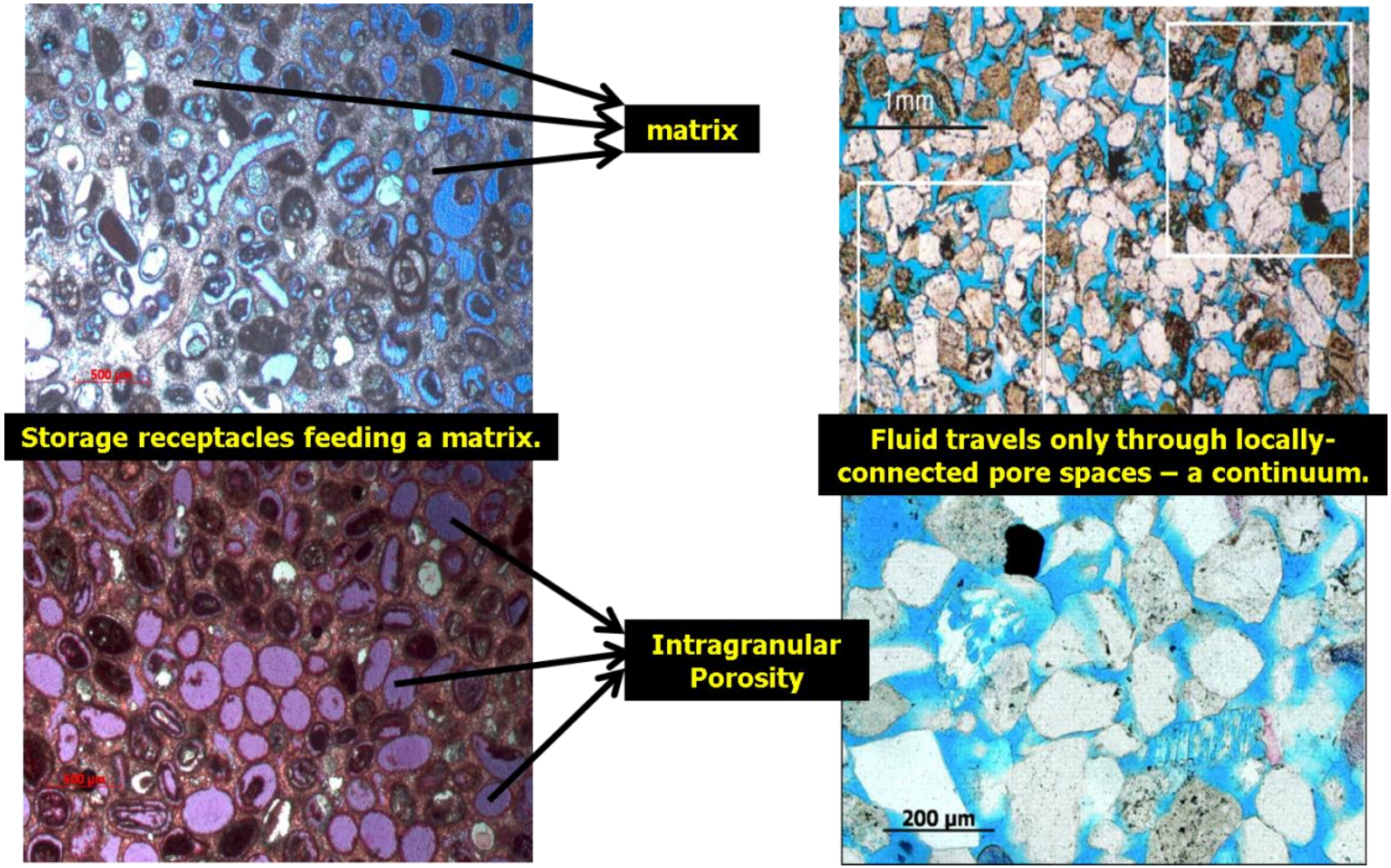

Figure 8 – Thin-section comparison of the typical porosity in Sandstone and Carbonate. This suggests that a continuum description, while natural for sandstone reservoirs may not be so for most carbonate reservoirs.

1.1.2 Conventional Means of Characterizing Carbonates

The difficulties in characterizing carbonate reservoirs have led to many different approaches and work-flows that integrate multiple sources of data. However, most of them echo the workflow for sandstones by ultimately deriving porosity-permeability relationships for a given rock-type.

For instance, a method using Middle Eastern carbonate data combining Nuclear/NMR resistivity logs and (borehole) image data to determine the rock facies and its corresponding fraction of vuggy, intergranular and intragranular porosities was used to correlate and calculate a synthetic bulk permeability that includes the contributions of both vug and matrix porosity at different length scales (Ramakrishnan et al. 2001).

A particularly complex carbonate reservoir including vuggy and fractured porosity was studied by Iwere et al. (2004) . They created a static model for dual-porosity simulation by choosing to extract a bulk matrix porosity-permeability transform by identifying and extracting secondary-porosity values from a sequential testing program of mercury and air-brine capillary pressure tests.

An integrated characterization workflow for characterizing many of the hydrocarbon reservoirs in Abu Dhabi, was applied onto an analogous outcrop of the reservoir at Wadi Rahabah (Vaughan et al. 2004). They reduced the outcrop into four facies not based on pore-type, but based on depositional texture (size of visible grains) since the porosity type was dominantly inter-particle. This allowed them to effectively use a bulk porosity-

permeability transform for each facies. The outcrop was gridded into blocks, with the thickness and facies of each, allocated according to the observations at the outcrop.

A very vuggy and naturally fractured reservoir with a complex diagenetic history – the formation underwent karsting and vug development, as well as fractures enhanced by solution that connected the vugs and effectively created a triple porosity system – was modelled with both a dual porosity single permeability (DPSP) and a dual porosity dual permeability (DPDP) model (Gurpinar et al. 1999). They went through a meticulous process that involved studying the vug connectivity and its relationship to fracture connectivity. Subsequently they determined fracture porosity and a connected vug porosity and used whichever was greater as the fracture porosity in the DPSP simulator. The matrix porosity used was in addition to the non-connected vuggy porosity and non-vug matrix porosity (log-derived).

In summary, reducing carbonate reservoirs to average values of permeability/porosity either for a single or dual porosity model, for the purposes of building an equivalent grid-based representation is a well-studied solution, albeit borrowed from the methodology for modelling siliciclastic reservoirs.

1.1.3 Prior Work on Pore-space Modelling

It is relevant to discuss some of the prior work done on pore-space flow modelling and permeability prediction from CT and μ-CT scan data. As will be mentioned in the next section, we will also be seeking to extract permeability of a μ-CT sample, by representing the rock sample in an unstructured manner and using both convective and diffusive flow tests.

A 3-dimensional network cell model was created by effectively reducing the X-ray CT scan sample to a grid system of cells connected by simple rectangular geometry (Narayanan and Deans 1988). Porosities were assigned to each cell based on the porosity distribution obtained from the sample on a pixel-by-pixel basis. The authors then proceeded to solve for the steady-state pressure distribution in the system. The concentration of a tracer in each cell was subsequently used to study the flow-paths in the sample.

3D pore-scale modelling of sandstones has also been attempted by first stochastically generating a set of spherical grains from a given grain size distribution, and then accounting for the processes of deposition of the individual grains by adjusting the grain sizes for sedimentation, compaction and clay-coating diagenesis that reduces pore-space (Bakke and Øren 1997). The authors verified the final model by comparing the calculated porosity values to that from a cross-section from a CT-scan. They then proceeded to extract a skeleton from this synthetic model and reduced it to a node-and-

bond model. Flow simulations were then employed assumed Poisuille flow between nodes. We will be following a similar workflow for our research.

A similar process-based generation of a synthetic μ-CT scan for a was also attempted on a carbonate sample (Biswal et al. 2009). The authors first employed a continuum deposition of points in a cube via a probability density function derived from a 2D image. Each point was then associated with an object which had three properties: size, orientation, and type of crystal. A geologic analysis of the 2D image was then performed in order to extract probability distributions for each property, which were then applied onto the deposited points. Although this was performed only for a carbonate rock that retained only intergranular and interparticle porosity, they showed that porosity estimates from such a μ-CT sample and laboratory results were comparable.

A novel workflow that used multi-point statistics from 2D thin section images of a subsurface carbonate rock to stochastically reconstruct a synthetic 3D μ-CT equivalent of the rock has also been attempted and validated (Al-Kharusi and Blunt 2008). A network extraction algorithm was then used to extract a topologically representative pore-network in 3D and reduce it to a system of nodes and bonds. They concluded that there was excellent agreement between permeability, capillary pressure and relative permeability curves predicted using the network model with those measured in the lab.

A means of reconstructing a stochastic network such that it can be upscaled to larger length-sizes while preserving the flow characteristics observed at smaller length-scale has also been illustrated (Jiang et al. 2012). The authors discussed a method of extracting

a pore-network from any given length-scale representation of data following which they extracted statistics of the nodes (radius, volume, co-ordination number) and bond (volume, length, radius and shape-factor). This information was then used to reconstruct the rock over a larger volume than the original set of images. They showed that permeability capillary pressure and relative permeability curves obtained from such a system was in good agreement with a laboratory measurement.

This literature review suggests that flow properties extracted from pore-level data is representative of the rock at larger length scales as well.

1.3 Proposed Solution and Methodology

The heterogeneous nature of connectivity in carbonate reservoirs can be better represented via an unstructured lattice that removes the constraint of geometry from each node. An example of this form of representation in a sandstone-reservoir that has been reduced to an unstructured lattice of nodes and bonds is shown in Figure 9. Each node carries only the pore-volume of the whole reservoir compartment it represents and no other geometric information. Each node is connected to its neighboring compartment by a bond that carries the transmissibility between the two compartments. In this way the length-scale of connectivity is not bound by the geometry of the cell and instead by the flow behavior observed at the compartment length-scale in the reservoir. Additionally, since this system still carries transmissibilities and volumes, it still fits into the language of reservoir simulators. For carbonates, this would demand the creation of three separate such unstructured skeletons, one for the matrix, vug and fracture system in the rock, as

well as (upscaled) inter-skeleton transmissibilities. This manner of representation is potentially the long-term target of this research. The study performed in this thesis is viewed as a first step toward this goal.

This project consists of two bodies of work geared at first illustrating the applicability of an unstructured and lattice representation of connectivity.

First, convective and diffusive calculations performed on a grid will be compared with their equivalents on a lattice, in order to establish the veracity of the lattice approach. Convective time-of-flight and diffusive time-of-flight (τ), as well as drained pore-volumes with respect to τ and time $V_p(\tau)$ and $V_p(t)$ will be compared.

Secondly, the pore-space extraction work flow suggested in the literature will be employed on a μ-CT scan of a carbonate sample, which will subsequently be represented as an unstructured lattice of nodes and bonds. Both convective and diffusive flow calculations/visualizations will be carried out on this sample in order study the connectivity and extract a permeability value. This will illustrate the usefulness and applicability of the lattice representation, and demonstrate a connectivity-driven approach as opposed to a cell-driven approach.

1.4 Summary

The discussions of this chapter are summarized below.

1. While sandstone pore-spaces are always intergranular or interparticle, this is usually not the case for carbonate rocks, which have far more complicated and unstructured pore-connectivity. This makes a lattice representation more suited for flow in carbonate rocks than a grid representation.

2. Permeability prediction from pore-space extraction was shown to produce results that corroborate laboratory tests.

3. Convective and diffusive calculations performed on a grid will be compared with their equivalents on a lattice, in order to establish the veracity of the lattice approach.

4. An unstructured lattice-system will be employed onto the pore-space extracted from a μ-CT sample for flow calculations and illustrate the approach.

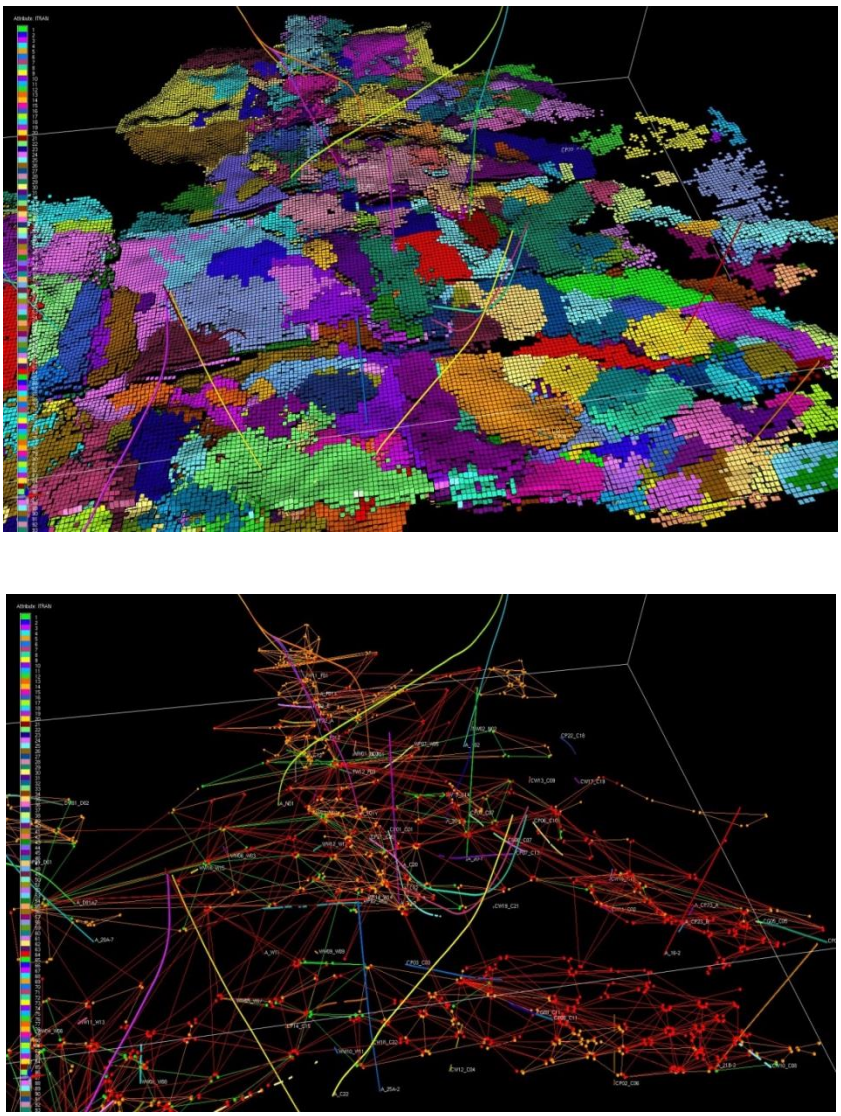

Figure 9 – Shows a gridded sandstone reservoir (TOP) and its equivalent as an unstructured lattice at the reservoir flow-unit scale (BOTTOM). Each node carries only the pore-volume of a reservoir compartment (colored), and carries the transmissibility to each other compartment that it connects.

CHAPTER II

GRID-BASED VS. LATTICE-BASED CALCULATIONS

This chapter establishes whether convective and diffusive calculations on a grid are comparable with their equivalents on a lattice. Specifically, the convective time-of-flight from each cell to a producer calculated using Pollock's algorithm will be compared with a simple approximation for flow between nodes. This comparison will be performed on the highly heterogeneous SPE10 dataset. The Fast Marching Method (FMM) is applicable on grids whereas Dijkstra's algorithm is more suitable on a lattice. The diffusive times-of-flight (τ), to a producer calculated using FMM and Dijkstra's algorithm will be compared. The geometric approximation developed by (Xie et al. 2012) and (Zhou 2013) employs a calculation for the drained pore-volume with respect to τ, $V_p(\tau)$, to estimate the pressure derivative. A comparison will also be made for $V_p(\tau)$ and $V_p(t)$ calculated using both algorithms.

2.1 Background

In this section, the calculations relating to the convective and diffusive times of flight calculations will be discussed.

2.1.1 Convective Time-of-Flight Calculation via Pollock's Method

The convective time-of-flight relates to the transit time of a particle from a point in space on a streamline to an injector (source) or producer (sink). First, a pressure solution is performed to find the pressure at the center of every gridblock, and volumetric fluxes through every face of the grid-block are calculated using Darcy's law. To find the time-of-flight from the center of a block to the producer or injector, a streamline is traced using Pollock's algorithm (Pollock 1988) from one of its faces and the time taken to traverse each grid-block is cumulatively added. Pollock's algorithm uses a sub gridblock velocity model that assumes that the velocity varies linearly between the values on the appropriate pair of cell faces (Goode 1990). A 2D example calculation is shown in Figure 10.

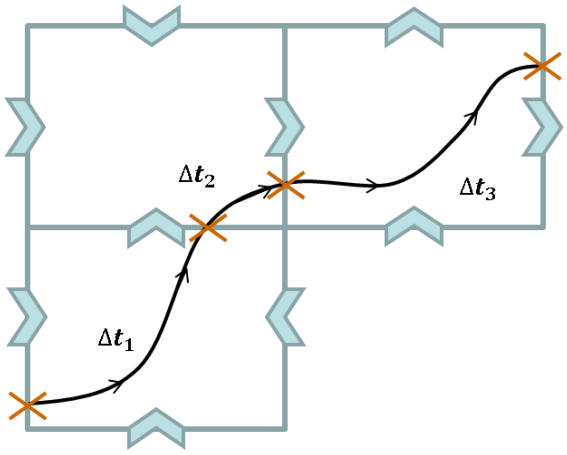

Figure 10 – Shows how streamlines are traced in a 2D example for calculating times-of-flight.

The velocity inside a cell at any given point (x, y) is given by **Eq. 2.1 – 2.4** below.

$$u_x = u_{x1} + c_x(x - x_1) \quad (2.1)$$

$$u_y = u_{y1} + c_y(y - y_1) \quad (2.2)$$

$$c_x = \frac{(u_{x2} - u_{x1})}{\Delta x} \quad (2.3)$$

$$c_y = \frac{(u_{y2} - u_{y1})}{\Delta y} \quad (2.4)$$

Where:

$u_{x/yi}$ = velocity in x or y direction, i=1, 2 based on which grid face in each direction.

Pollock's algorithm works by finding the minimum positive time-of-flight to each exit face (i). Considering a particle starting at an arbitrary location inside the cell (x_0, y_0), the time of flight to each face may be computed as:

$$\frac{\Delta\tau_{xi}}{\phi} = \frac{1}{c_x}\ln\left(\frac{u_{xi}}{u_{x0}}\right) \quad (2.5)$$

$$\frac{\Delta\tau_{yi}}{\phi} = \frac{1}{c_y}\ln\left(\frac{u_{yi}}{u_{yo}}\right) \quad (2.6)$$

$$\Delta\tau = minimum\ positive\ (\Delta\tau_{x1}, \Delta\tau_{x2}, \Delta\tau_{y1}, \Delta\tau_{y2}) \quad (2.7)$$

Where:

ϕ = porosity of the cell.

$\Delta\tau_{yi}$= time of flight to the face yi, i=1, 2 based on the grid face in each y direction.

$\Delta\tau_{xi}$= time of flight to the face xi, i=1, 2 based on the grid face in each x direction.

Once the time-of-flight to the exit point is known, the exit co-ordinates are determined by the following equations:

$$x = x_0 + u_{x0}\left(\frac{e^{\frac{c_x \Delta\tau}{\phi}} - 1}{c_x}\right) \quad (2.8)$$

$$y = y_0 + u_{x0}\left(\frac{e^{\frac{c_y \Delta\tau}{\phi}} - 1}{c_y}\right) \quad (2.9)$$

Once these exit co-ordinates are determined, they become the new origin points for tracing in the next cell. The times-of-flight accumulated for a streamline traced in this manner to a producer for an initial point in the center of each cell constitutes the time-of-flight to the producer for every cell. Similarly, if streamlines are traced counter to the velocity, then one obtains the time-of-flight to the injector.

2.1.2 Approximate Convective Time-of-Flight Calculation on Lattice

The convective time-of-flight on the lattice however, does not involve tracing the trajectory of the particle within each cell, since the cell/node does not carry any geometric information other than a volume. The time-of-flight is hence simply the time taken to travel from the center of one cell to another by **Eq. 2.10 - 2.11** and as suggested by Figure 11. Once the time-of-flight to each connecting node is determined, the time-of-flight chosen is once again simply the minimum positive of all the choices. Similarly, the accumulative times-of-flight from the center of the cell to the center of a producer cell constitutes the time-of-flight to the producer for every cell on the lattice.

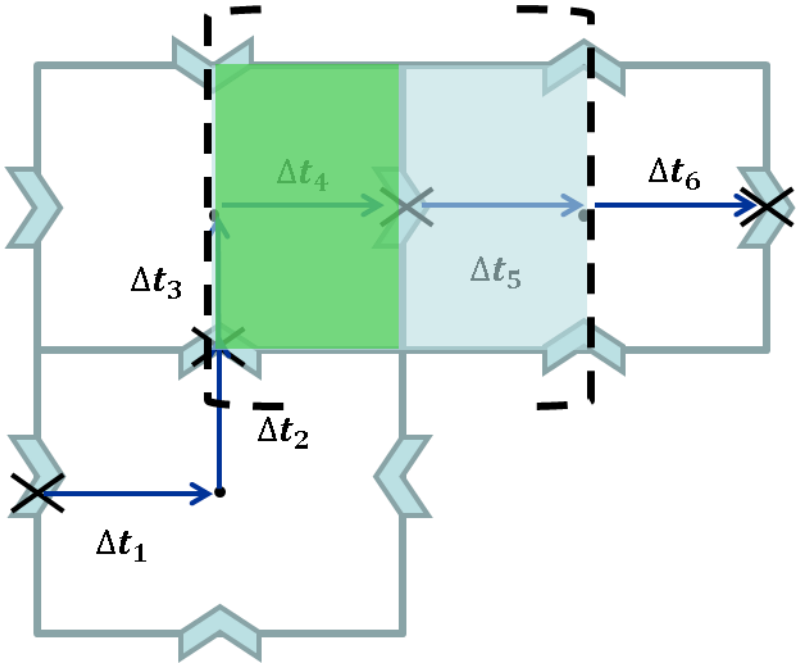

Figure 11 – Shows the approximation for times-of-flight in the lattice-sense. An example calculation for the highlighted region is shown below.

$$\Delta t_4 + \Delta t_5 = \frac{PV_{i+1/2} + PV_{i-1/2}}{Q_i} \quad \ldots\ldots (2.10)$$

$$Q_i = Transmissibility * \Delta P \quad \ldots\ldots (2.11)$$

Where:

$PV_{i+1/2}$ = ½ of the pore volume of cell to the right of the face.

$PV_{i-1/2}$ = ½ of the pore volume of the cell to the left of the face.

Q_i = flux in the i direction.

2.1.3 Concept of Diffusive Time-of-Flight

The radius of investigation has been defined as the distance of peak pressure disturbance from an impulse source or sink (Lee 1982). This quantity is described by **Eq. 2.12** for a 2D homogeneous reservoir:

$$r = \sqrt{\frac{kt}{948\phi\mu c_t}} \quad (2.12)$$

Where:

r, radius of investigation (ft);

k, permeability (md);

t, time (hours);

ϕ, porosity (fraction);

c_t, total compressibility (psia^{-1});

This definition was generalized into a depth of investigation for heterogeneous reservoirs using the concept of diffusive time of flight, τ (Kulkarni et al. 2000; Vasco et al. 2000). τ represents the propagation time of the pressure wave into the reservoir, and also represents the distance into the reservoir as well. Figure 12 illustrates the concept of diffusive time of flight in heterogeneous reservoirs as a spatial co-ordinate.

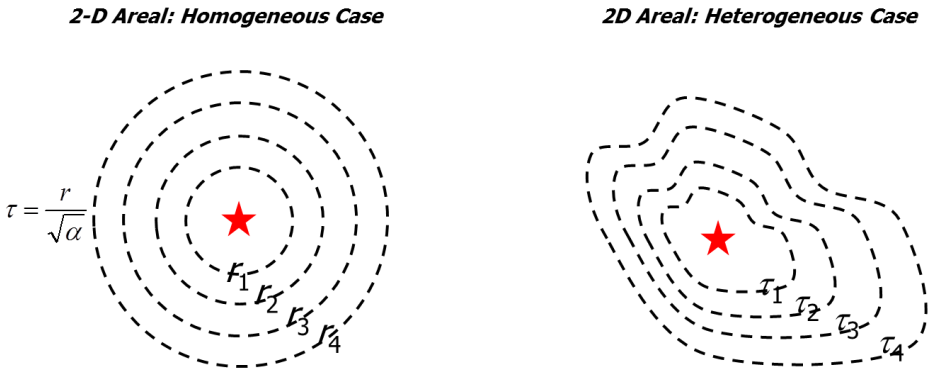

2-D Areal: Homogeneous Case

2D Areal: Heterogeneous Case

Figure 12 – Shows τ as a spatial coordinate (Datta-Gupta 2013).

The contours of τ can be obtained by solving the Eikonal equation shown in **Eq. 2.13** which is a high frequency asymptotic solution of the diffusivity equation (Datta-Gupta and King 2007; Vasco et al. 2000)..

$$\sqrt{\alpha(x)}|\nabla\tau(x)| = 1 \ldots\ldots\ldots\ldots\ldots\ldots\ldots\ldots\ldots (2.13)$$

Where:

$\tau(x)$, diffusive time of flight;

$\alpha(x)$ is the diffusivity given by

$$\alpha(x) = \frac{k(x)}{\phi(x)\mu c_t} \ldots\ldots\ldots\ldots\ldots\ldots\ldots\ldots\ldots (2.14)$$

The Eikonal equation indicates that the pressure ‘front’ propagates in the reservoir with a velocity equal to the square root of diffusivity. Diffusive time of flight along a ray path can be calculated using the following equation:

$$\tau(r) = \int_0^r \frac{1}{\sqrt{\alpha}}\, dr' \ldots\ldots\ldots\ldots\ldots\ldots\ldots\ldots\ldots (2.15)$$

Where,

r, distance from a source/sink;

2.1.4 The Fast Marching Method and Dijkstra's Algorithm

The Eikonal equation may be very efficiently solved using Fast Marching Methods (FMM), as they are a non-iterative single pass calculation, and can be constructed sequentially from small τ to large τ (Sethian 1999). Dijkstra's algorithm is more appropriate on a lattice, whereas the generalized (FMM) is applicable on grids. The distinction between Dijkstra's Algorithm – which is *a* Fast Marching Method – and *the* Fast Marching Method used for grid-blocks is clarified below.

An illustration of the manner by which a FMM populates a mesh given a seed node for diffusive time-of-flight is shown in Figure 13 and is described by the steps below (Xie et al. 2012):

1. Label the seed node as an accepted node with $\tau = 0$
2. Mark all neighboring nodes A, B, C, D and calculate the diffusive time of flight to all the neighboring nodes
3. Accept the node with minimum diffusive time of flight
4. Include the new neighboring nodes for accepted node consideration with minimum diffusive time of flight

Repeat steps 2 to 4 until all the nodes in the mesh are accepted.

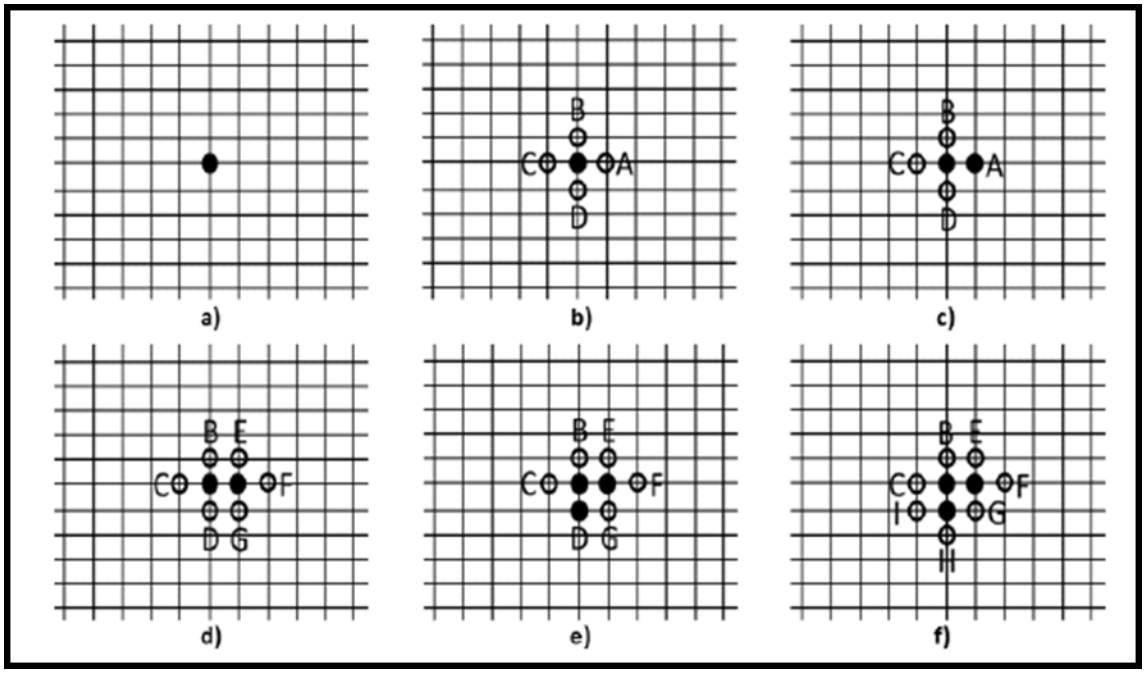

Figure 13 – Illustrates the manner by which FMM populates a mesh (Sethian 1999).

The general form of **Eq. 2.13** for anisotropic permeability and its solution was discussed by (Zhang et al. 2013). This is the solution described as *the* Fast Marching Method to populate diffusive times-of flight on a grid. Assuming that the principle directions of the permeability tensor are aligned with cell edges (tangent vectors). The equation with the permeability tensor $\bar{\bar{k}}$ is written as:

$$\nabla\tau \cdot \bar{\bar{k}} \cdot \nabla\tau = \emptyset\mu c_t \ldots\ldots\ldots\ldots\ldots\ldots (2.16)$$

Eq. 2.16 can also be re-written in the following form:

$$\sum_{i=1}^{3} \frac{k_i}{t_i^2} \left(\frac{\partial \tau}{\partial \hat{x}_i} \right)^2 = \emptyset \mu c_t \dots\dots\dots\dots\dots\dots\dots\dots\dots\dots\dots\dots\dots\dots\dots\dots\dots\dots\dots\dots\dots\dots\dots\dots\dots\dots (2.17)$$

Where:

k_i = permeability in i direction, i=1, 2, 3 or I, J, K

t_i = length of tangent vectors in i direction, i=1, 2, 3 or I, J, K.

This equation is now discretized such that it lends itself easily to solution via the FMM recommended by (Sethian 1999). A 2D construction for unknown $\tau_{i,j}$ is illustrated by Figure 14 and described by the equations below.

$$\frac{\left(\tau_{i,j} - \tau_{i-1,j}\right)^2}{S_I^2} + \frac{\left(\tau_{i,j} - \tau_{i,j-1}\right)^2}{S_J^2} = 1 \dots\dots\dots\dots\dots\dots\dots\dots\dots\dots\dots\dots\dots\dots\dots\dots\dots\dots\dots (2.18)$$

$$S_I = \frac{l_{I+}(i-1,j)}{\sqrt{\alpha_I(i-1,j)}} + \frac{l_{I-}(i,j)}{\sqrt{\alpha_I(i,j)}} \dots\dots\dots\dots\dots\dots\dots\dots\dots\dots\dots\dots\dots\dots\dots\dots\dots\dots\dots\dots\dots (2.19)$$

$$S_J = \frac{l_{J+}(i,j-1)}{\sqrt{\alpha_I(i,j-1)}} + \frac{l_{J-}(i,j)}{\sqrt{\alpha_I(i,j)}} \dots\dots\dots\dots\dots\dots\dots\dots\dots\dots\dots\dots\dots\dots\dots\dots\dots\dots\dots\dots\dots (2.20)$$

Where:

α_i = diffusivity in i direction, i = I, J

$l_{i\pm}$ = half-length from cell-center to the appropriate face, i = I, J

Essentially, a quadratic solution is solved in **Eq. 2.18** for unknown $\tau_{i,j}$. Multiple-solutions will be obtained depending on the number of *pairs of neighbor nodes* available. The smallest of the solutions is updated as the solution for $\tau_{i,j}$. The fast

marching methodology described by Figure 13 can thus be applied to rapidly populate the unknown diffusive times-of-flight on a grid.

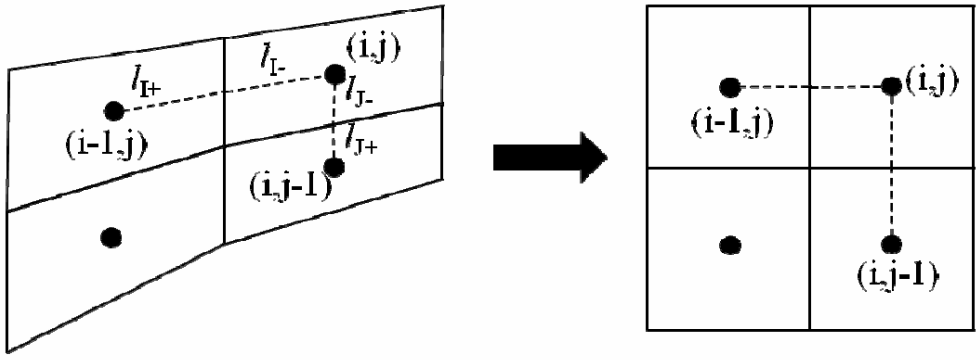

Figure 14 – Shows the discretization of Eq. 2.17 on a 2D corner point grid isoparametric mapping. (Zhang et al. 2013). Essentially, two neighbors are used to determine the diffusive time-of-flight for unknown τ (i, j).

Dijkstra (1959) method for solving the Eikonal equation on the other hand is simpler and involves only a linear – rather than a quadratic – equation for unknown τ. This means that Dijkstra's method involves only 1 neighbor in the calculation, i.e.: the FMM reduces to Dijkstra's when only 1 gradient is available. Essentially, this involves choosing the smallest amongst the available options of $\delta\tau$, and from only 1 neighbor node:

$$\delta\tau = \delta r\sqrt{\frac{\phi\mu c_t}{k}} \quad \ldots\ldots\ldots\ldots\ldots\ldots\ldots\ldots\ldots\ldots\ldots\ldots\ldots\ldots (2.21)$$

The simplicity of this construction makes it very suitable for calculations on an unstructured lattice.

2.2 Comparison of Convective Times-of-Flight between Grid and Lattice

Figure 15 compares the Convective Time-of-Flight from the center of every cell to the producer calculated on a grid and on a lattice. The red color indicates long times-of-flight and the green suggests a low value. The pockets of blue indicate stagnation points in the reservoir.

We observe that the lattice calculation picks up the heterogeneity albeit with a lower-resolution. Specifically, the high and low permeability regions as well as the stagnation points of the reservoir occur in the same areas of the reservoir in both calculations. Numerically as well the calculations are of similar orders of magnitude. We conclude that the convective time-of-flight calculation on a lattice compares favorably to that on a grid.

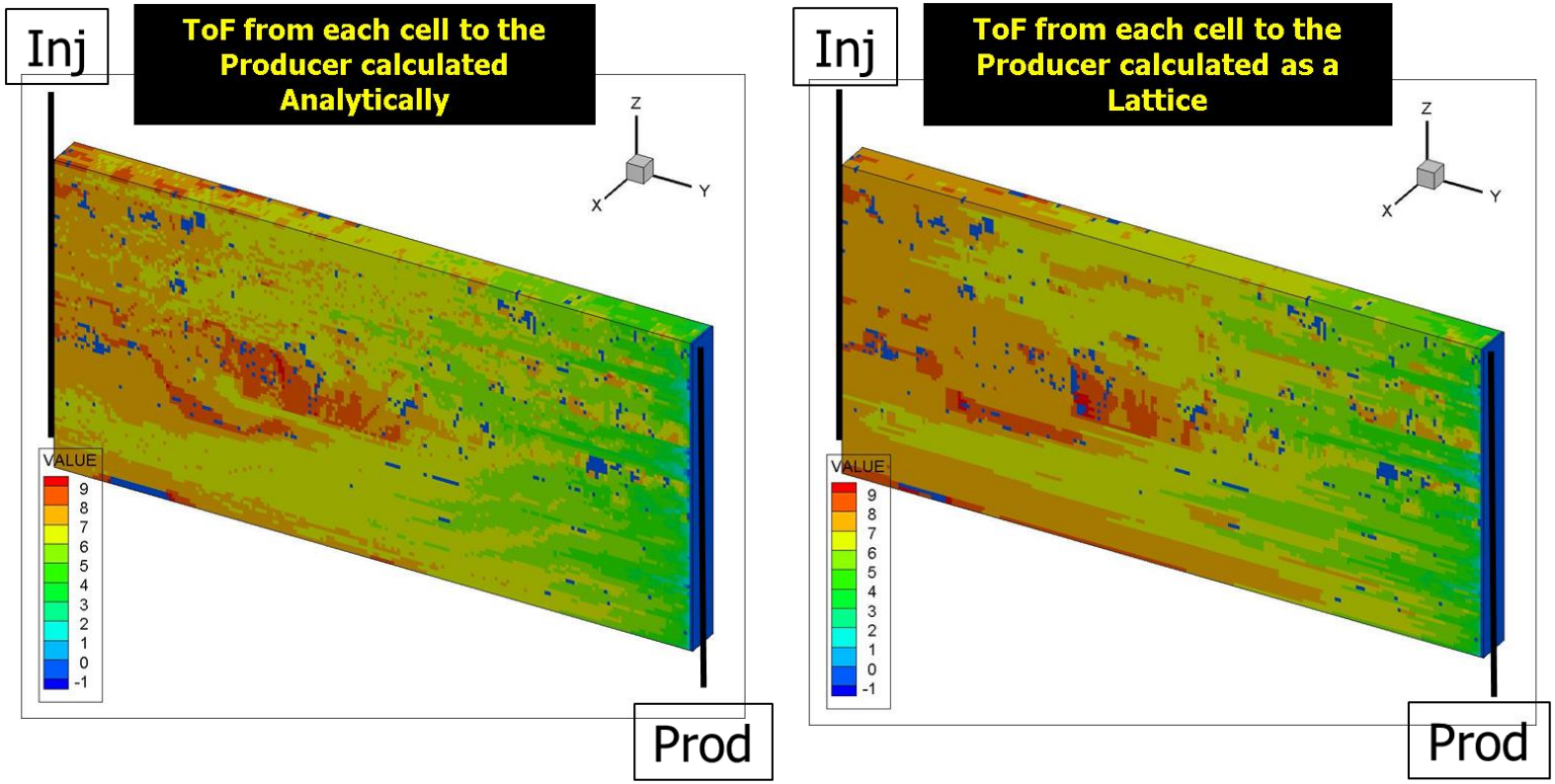

Figure 15 – Compares the Convective Time-of-Flight to the producer calculated using Pollock's algorithm (LEFT) on a grid with the approximation on a lattice system (RIGHT).

2.3 Comparison of Diffusive Time-of-Flight between Grid and Lattice

Figure 16 shows that Dijkstra's solution for the Diffusive Time-of-Flight for a constant permeability case carries a strong grid orientation effect when compared to the FMM. Figure 17 however, shows that as heterogeneity and anisotropy become more dominant, that the grid-orientation impact is reduced and produces a more comparable solution to the FMM. We again conclude that the Diffusive Time-of-Flight calculation via Dijkstra's method on a lattice compares favorably to that on a grid via the FMM.

2.4 Comparison of Drainage Volumes between Grid and Lattice

An analytical relationship between the drained pore-volumes $V_p(\tau)$ and $V_p(t)$ was suggested by (Zhou 2013) and is described by **Eq. 2.22**. In the lattice or grid sense this reduces to the approximation as described by **Eq. 2.23**. These equations are repeated from **Eq. 3.18 and Eq. 3.21** respectively. Section 3.5.1 in Chapter 3 contains a detailed discussion of these equations and their implications, but the final results are reproduced below for reference.

$$V_p(t) = \int_0^\infty dV_p(\tau) e^{-\frac{\tau^2}{4t}} \quad \ldots\ldots (2.22)$$

$$\mathrm{V_p(t)} \cong \sum_{\mathrm{j}} \mathrm{PV_j e^{-\frac{\tau_j^2}{4t}}} \quad \ldots\ldots (2.23)$$

Figure 18 and Figure 19, show that both methods produce similar results for $V_p(\tau)$ and $V_p(t)$. The grid-orientation effect observed in Figure 16 is accountable for the large difference in the value of $V_p(\tau)$ using Dijkstra's and the FMM, for homogeneous

permeability. The FMM, in fact produces a result that is nearly identical to the analytical value for the homogeneous case. This difference significantly reduced as the grid-orientation effect is reduced with greater heterogeneity.

2.5 Summary

The observations of this chapter are summarized below.

1. Lattice-based calculations for convection and diffusion are comparable to those performed using grid-based calculations.

2. There is a grid-orientation effect in the lattice calculations via Dijkstra's algorithm, but its impact is reduced as the heterogeneity increases.

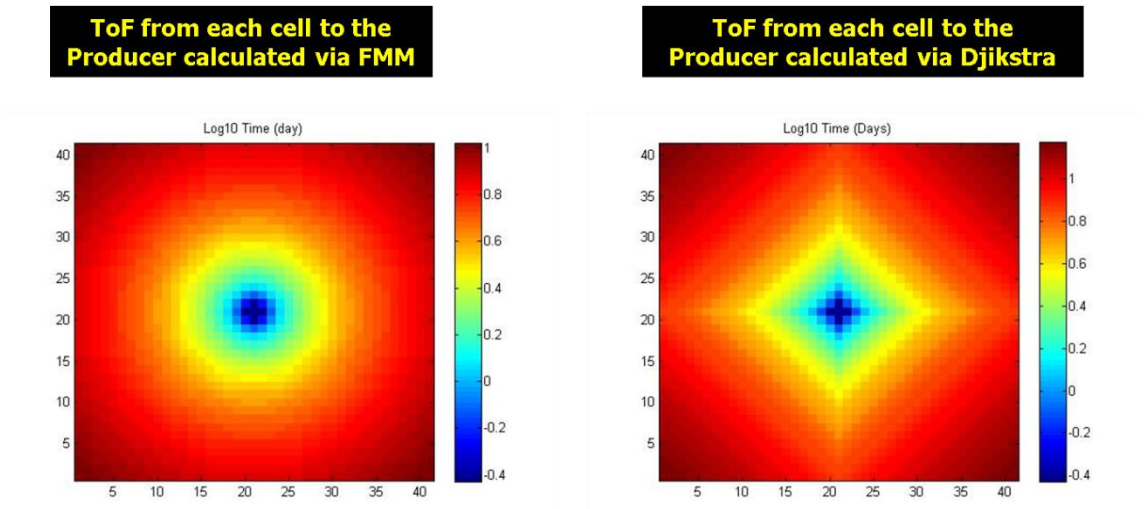

Figure 16 – Compares the Diffusive time-of-flight calculated via the FMM to Dijkstra, for homogeneous permeability.

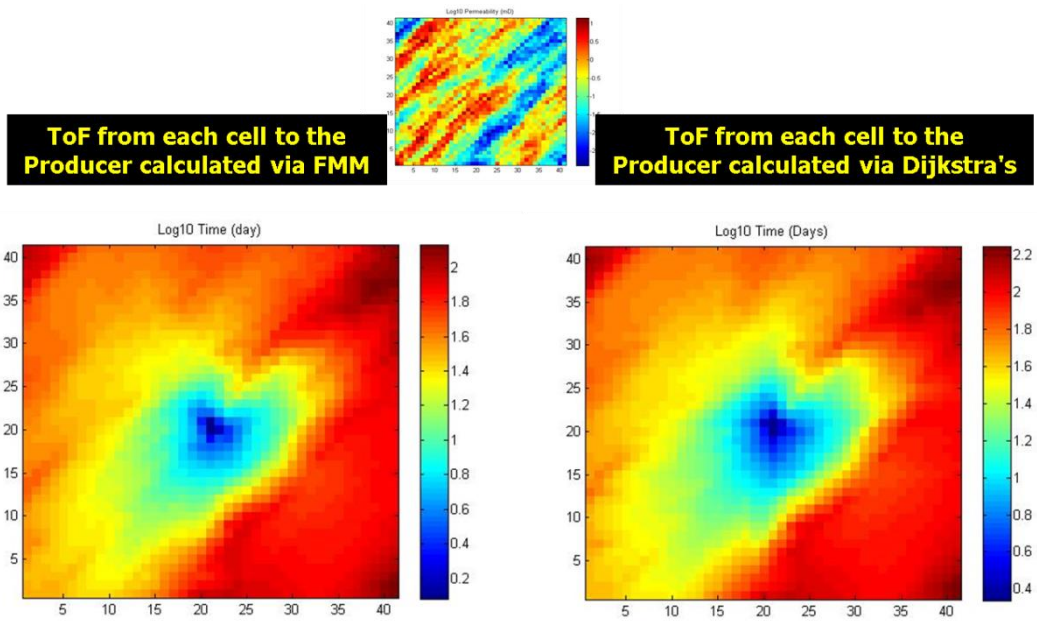

Figure 17 – Compares the Diffusive time-of-flight calculated via the FMM to Dijkstra, for heterogenous anistropic permeability.

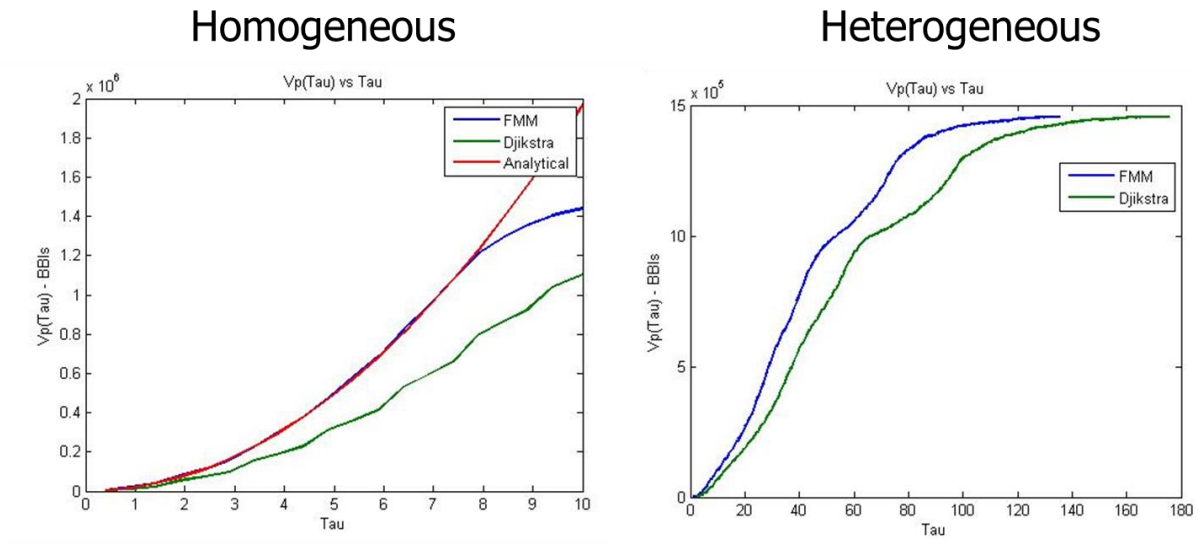

Figure 18 – Compares the Vp (τ) calculated using the FMM to that obtained from Dijkstra's method, for both cases of homogeneous (left) and heterogeneous permeability (right).

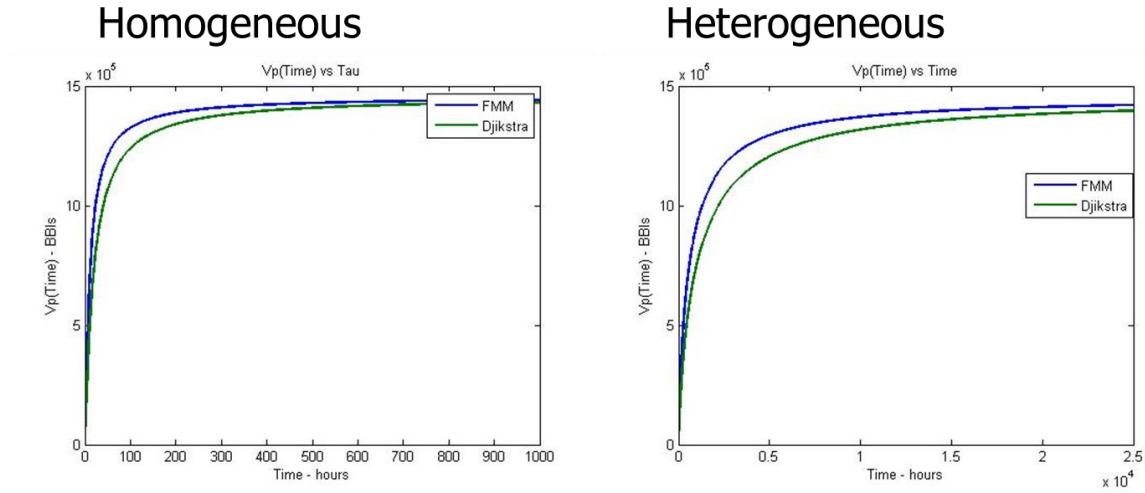

Figure 19 – Compares the Vp (t) calculated using the FMM to that obtained from Dijkstra's method, for both cases of homogeneous (left) and heterogeneous permeability (right).

CHAPTER III

MICRO-CT SCAN DATA ANALYSIS

This chapter describes the analysis performed on a μ-CT scan data of a carbonate sample. First the methodology applied in converting the digital rock-sample into an equivalent unstructured lattice of nodes and bonds is described, following which the implications of the resulting data statistics will be discussed. Subsequently, the lattice will be employed to perform convective and diffusive calculations. Specifically, a digital core-flood will be employed to extract a convective permeability, and a diffusive process will be initiated in order to extract diffusive transport quantities. This chapter will thus strive to illustrate the immense heterogeneity of carbonate rocks and also illustrate the suitability of an unstructured lattice-based representation for such a system.

3.1 Data Preparation

Dr. Anuj Gupta's group at TAMUQ gathered outcrop samples from the Jebel Fuwairit Beach Bar Complex. A slice from a μ-CT scan with 1X zoom of one such sample is shown in Figure 20 below. A sub-volume of the scan data far enough away from the edges, but still of dimensions comparable to the original core was used to minimize data artefacts. The inner-square shows the extent of data within the core used. The dimensions of this sub-volume used are approximately **7.5 X 6.5 X 8.5 millimeters**. AVIZO Fire suite was used for all the Digital Rock Physics functions. Specifically, our

purpose was to reduce the rock to a lattice of nodes and connections – effectively extracting the pore-connectivity skeleton of the core sample.

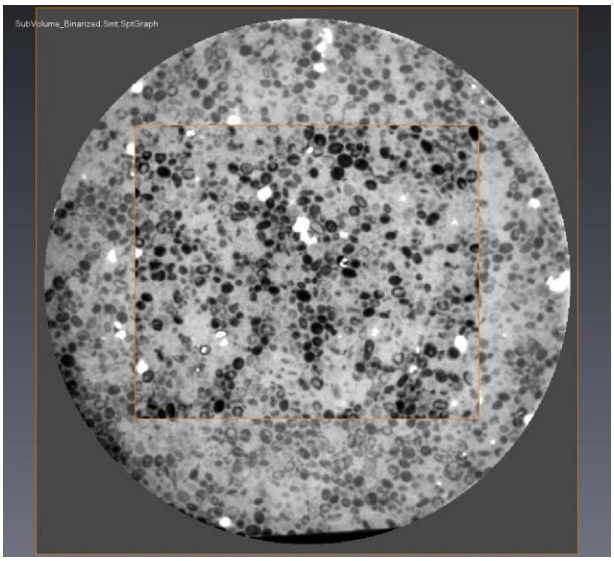

Figure 20 – Shows a slice of the 3D μ-CT scan data-stack used to extract the connectivity skeleton. The inner-rectangle shows the areal extent of the core used in the analysis.

3.1.1 Image Pre-Processing

AVIZO comes with several built-in tools that may be used in a trial-and-error basis in order to process the images for further analysis. For the μ-CT scan above, the best results were obtained by first using the *3D-Adaptive Histogram Equalization* module to heighten the contrast between matrix, cement and pore, followed by the *Unsharp Masking* module to sharpen the edges of the pore. The raw and processed images are shown in Figure 21.

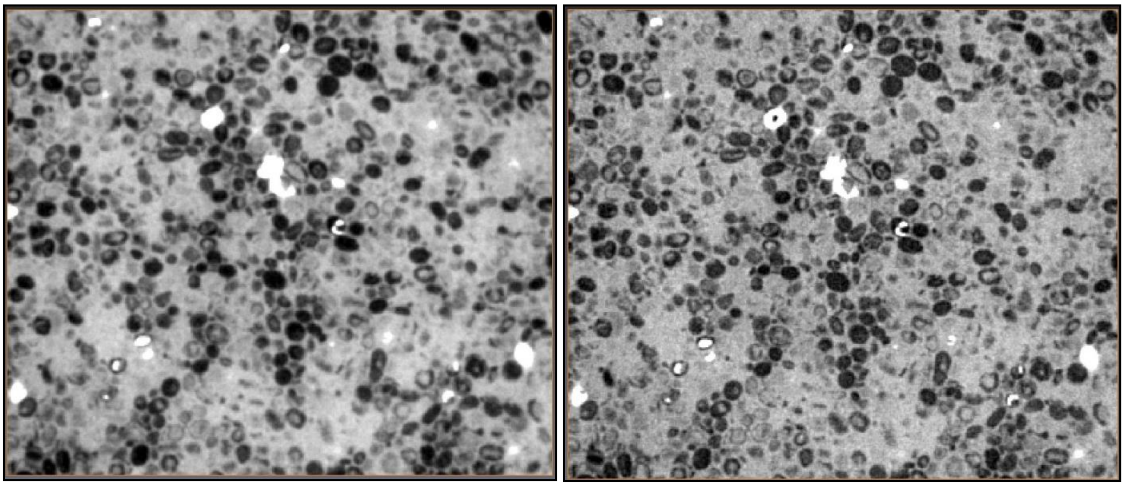

Figure 21 – Shows the raw image on the LEFT and the processed image on the RIGHT.

Upon processing the data, the boundaries of the matrix, cement within the pore and the pores themselves are more pronounced, and have a more distinct range of voxel intensity. This also lends itself to clearer interpretation of the geological history of the rock.

3.1.2 Binarization

The rock can now be effectively binarized into pore and non-pore. AVIZO enables the user to interactively choose the range of voxel intensity which relates to the pore, and affect the binarization accordingly. The segmented images are shown in Figure 22 below.

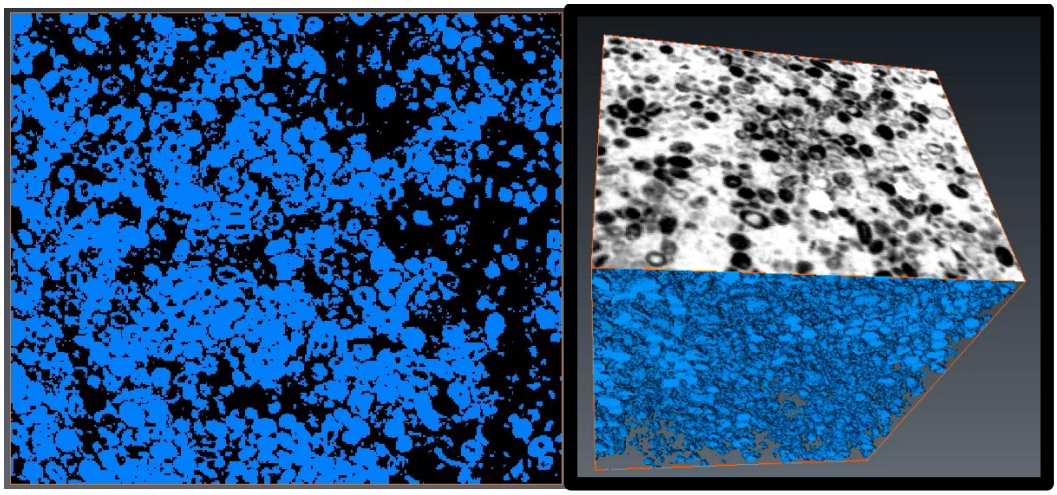

Figure 22 – Shows a slice of the µ-CT stack binarized into pore, in blue, and non-pore in black (LEFT). The whole body of pores in the core is shown in a 3D rendering (RIGHT).

Figure 23 also shows the result of employing a series of segmentation and separation algorithms after binarization. This removes the connectivity between pores and serves to highlight how the pore-shapes have been significantly altered from their original elliptical shapes as a result of diagenesis.

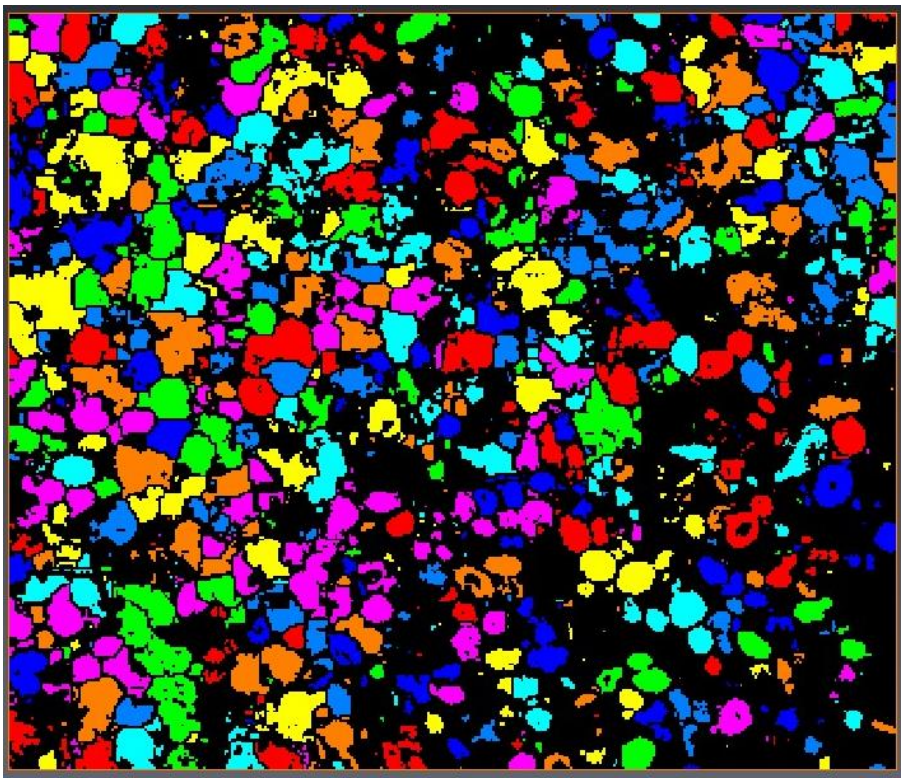

Figure 23 – Shows the pores separated from each other so that the random manner in which diagenesis has altered the original pores is highlighted. The colored portions refer to the pore-spaces, with adjacent pores assigned different colors.

3.1.3 Skeletonization

The Skeletonization module of AVIZO was employed in order to extract the nodes and the connections. First a distance map of the segmented image is calculated where the distance to the nearest boundary voxel is computed. This distance image-map is then thinned until a string of connected voxels remain, effectively extracting the pore-throats of each connection between the pores. A 3D rendering is shown in Figure 24 below. The rock at μ-CT scale has hence been broken into a set of nodes oriented randomly in space, with the number and strength of connections/bonds between them dictated by the rock-

fabric. Effectively we now have node volumes, and pore-throat attributes like radii and length.

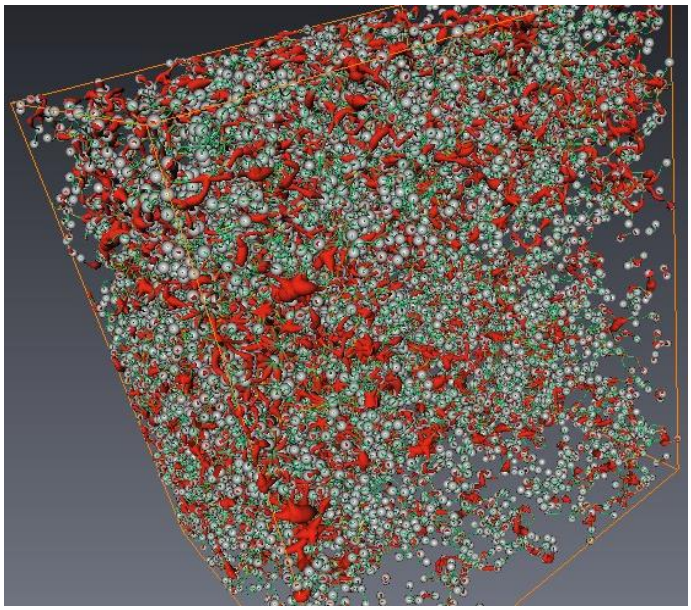

Figure 24 – Shows the result of the Skeletonization module applied to the data stack after binarization, highlighting the bonds and nodes.

3.1.4 Conclusions from µ-CT Scan Images

This is an example of a meteorically leached and extensively cemented, bioclastic peloidal grainstone. The bioclasts consist mostly of rounded/elongated and micritzed peloids. This rock was subject to diagenesis, first via a leaching process which formed moldic/intragranular pores, followed by growth of calcite cementation. The binarized slices appear to indicate that much of the permeability/connectivity is via pores that are connected via point contacts at the tips of the peloids. However, this seems to have

occurred fairly extensively so we expect effective porosity to remain fairly high and more importantly, permeability to be very high.

Extensive diagenesis has left the connectivity of each pore far from uniform in all directions and is fairly random. As such “pores” here is used fairly loosely, as in several locations the diagenetic process has left several pores neither completely leached out nor fully cemented inside. “Pores” which subsequently becomes nodes after skeletonization, simply refer to volumes.

Dr. Anuj Gupta’s group report that the Jebel Fuwairit outcrop is a formation similar to most gulf coast reservoirs, and may even be an analogue for the Khuff and Arab formations (Gupta and Poppelreiter 2010). Both of these are highly prolific and contain a vast quantity of gulf oil. The Khuff Formation reservoirs typically are characterized by porosities exceeding 30% and permeabilities of around 3000 md. The Arab Formation may be an even closer analogue as it not only forms the largest accumulations of Qatar, but also is comprised of peloidal, oolitic limestone. Typically, these have porosities of nearly 30% and where the grains are more rounded and sorted, permeabilities often exceed 5000 – 6000 md (Nairn and Alsharhan 2003). This is a very similar description to the observations of our μ-CT sample, and we expect permeability in subsequent analyses to be very high as well.

We recognize as well also, that any skeleton extracted from this core-data would be representative of the connectivity only within the matrix, i.e., only for this length-scale. To fully characterize the outcrop, pore (vug)-connectivity skeletons from the

successively lower resolutions (length-scale) – as appropriate – would need to extracted and then superposed upon one-another after determining *inter-skeleton* transmissibilities. While this is outside the scope of this particular study, it is envisaged as the final end-product of this research.

3.2 Data Statistics

A MATLAB toolbox was developed to import the skeletonization data from AVIZO for further analysis. The data statistics themselves serve to illustrate the level of heterogeneity –"unstructuredness" – occurring in even such a small volume of carbonate rock.

We seek to first establish the unstructured nature of the connectivity in carbonates by examining the connectivity characteristics of the nodes. In a grid-block based system with 6 locally-neighboring connections, a connectivity matrix – essentially a transmissibility matrix with a value of 1 for every connection and 0 for every non-connection – tends to be perfectly banded with 6 diagonal bands, with a connection in each of the 6 directions. However, since our lattice-representation is unstructured, and the rock fabric itself dictates the connections, each node may have more or less than 6 neighboring connections. This also means that each node need not only be connected to its "immediate" or locally neighboring nodes, but that each connection can be across any length. Essentially, we don't expect "banded-ness" in the connectivity or transmissibility matrix of a carbonate rock.

Figure 25 shows the connectivity matrix between the 83,623 nodes in this particular μ-CT scan. As expected, the unstructured-ness of the connections means that a neat & hexa-diagonally banded matrix is not obtained, and in fact several nodes have well more than 6 connections, and the connections are not necessarily the nearest neighbors as well. The close-up shown in Figure 25 is misleading as it gives the impression that a vast majority of the nodes have more than 10-12 connections, when in-fact this is an optical illusion due to the sheer size of the matrix (83623 X 83623). Figure 26 shows a histogram and CDF of the co-ordination number that tells the true story. The mean number of connections per node is 3, and 90% of the nodes have 5 or fewer connections. Yet since the number of nodes is so large, the number of nodes that have a large number of connections (10 or more) is still significant.

The unstructured-ness of the connectivity in the carbonate rock sample is further shown by the very broad spread of connection-lengths as highlighted in Figure 27. 90% of connections are under 1000 μm in length but the mean length is an order of magnitude smaller at 100 μm. This illustrates that the connections in carbonate rocks are not solely to *immediate* neighbors.

Figure 28 shows the histogram and CDF of bond radii. Nearly half of all connections in this rock appear to have a radius between 10 -11 μm. While the actual value of this radius may potentially be attributed to resolution limitations in the scan, it is quite possible that this refers to the size of the connections formed as the diagenetic processes dissolved and connected the point-contact tips of the oval-shaped peloids. While this

may be suggesting something about the fabric-selectivity of the diagenetic process that affected the rock, the randomness of the same diagenetic processes is also illustrated by two further observations. Firstly, the other half of all the connections have quite a broad spread of bond-radii, ranging from 12 – 60 μm. Secondly, within this window, the mean radius is around 15 μm. Effectively, there is bimodality in the distribution of connection radii. Figure 29 shows that this is mirrored even in the distribution of (equivalent) pore diameters. Similar to bond-radii, we observe that the more than half the pore-diameters are less than 30 μm, and in the other half there is a much broader spread with a second mode around 350 μm. As expected, pore throats have smaller radii than pores. However, we also note that there are extremely broad range of length scales associated with the pore-diameters – the two modes of the pore-size distribution are an order of magnitude different from each other – since they are not strictly grains, and instead moldic and vuggy porosity produced by diagenesis. Because of the bimodality in the pore-diameters and the pore-throats, we conclude that this rock is well sorted within two separate ranges.

Several crossplots were attempted, all of which failed to be useful in yielding a useful relationship between the variables. Acknowledging that the bond radii is related to the permeability and the total volume connected by either end of the bond is related to the porosity of the sample for instance; a crossplot relating the two was attempted but failed to show any relationship between the two. This is expected as the diagenetic processes that leach the peloids and subsequently re-crystallize within them, creating and plugging the pore-throats and pore-spaces, is not selective based on the size of the pellet. The

bond radius is dependent on the size of the point contact between the peloids, and since the orientation and size of the peloids are random (although most peloids less than 1 mm in size), we expect this is to be reflected in any relationship relating porosity to permeability. Similarly, a crossplot between bond radii and bond length did not highlight any trend, which is expected as the nature of the leaching and crystallization process that creates the connections between pores is more or less random.

Porosity calculated as a ratio of the sum of all node-volumes and the total rock volume, was determined to be 27.8%.

It is worth noting again that this level of heterogeneity is observed in just a cubic sample of carbonate rock a few millimeters in dimension. These findings serve to reinforce the idea that diagenetic processes produce a carbonate rock with a broad length-scale of connectivity, and further justify how a lattice-representation of the flow-paths is a more natural way to represent the rock in terms of nearest neighbor heterogeneity.

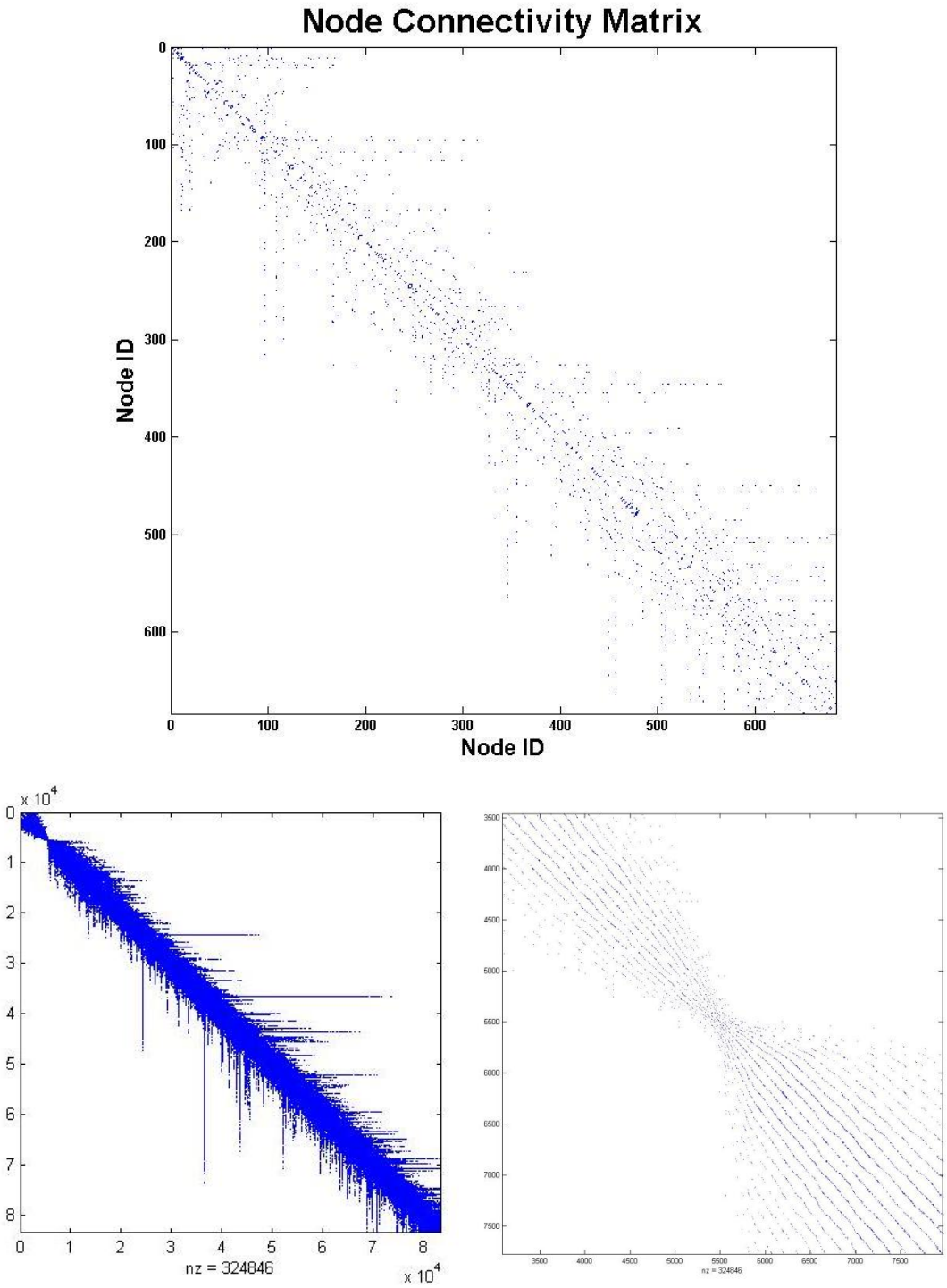

Figure 25 – Shows the Connectivity matrix for a portion of the sample on the TOP. The BOTTOM shows the matrix for the whole µ-CT scan sample on the LEFT, and a closer look at another portion of the matrix on the RIGHT.

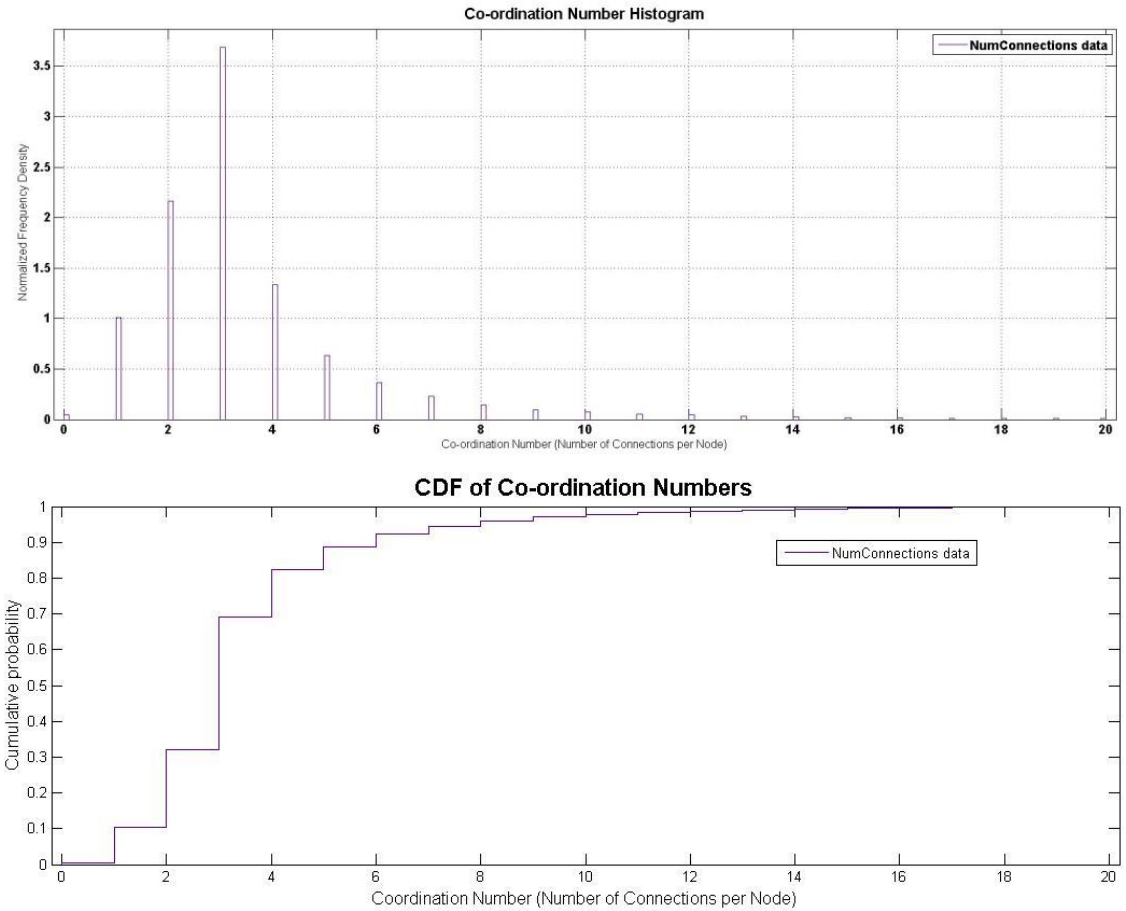

Figure 26 – Shows how the average number of connections per node is 3, and that most nodes have 5 or less connections. Note also that this carbonate rock still has a broad spread of connection numbers.

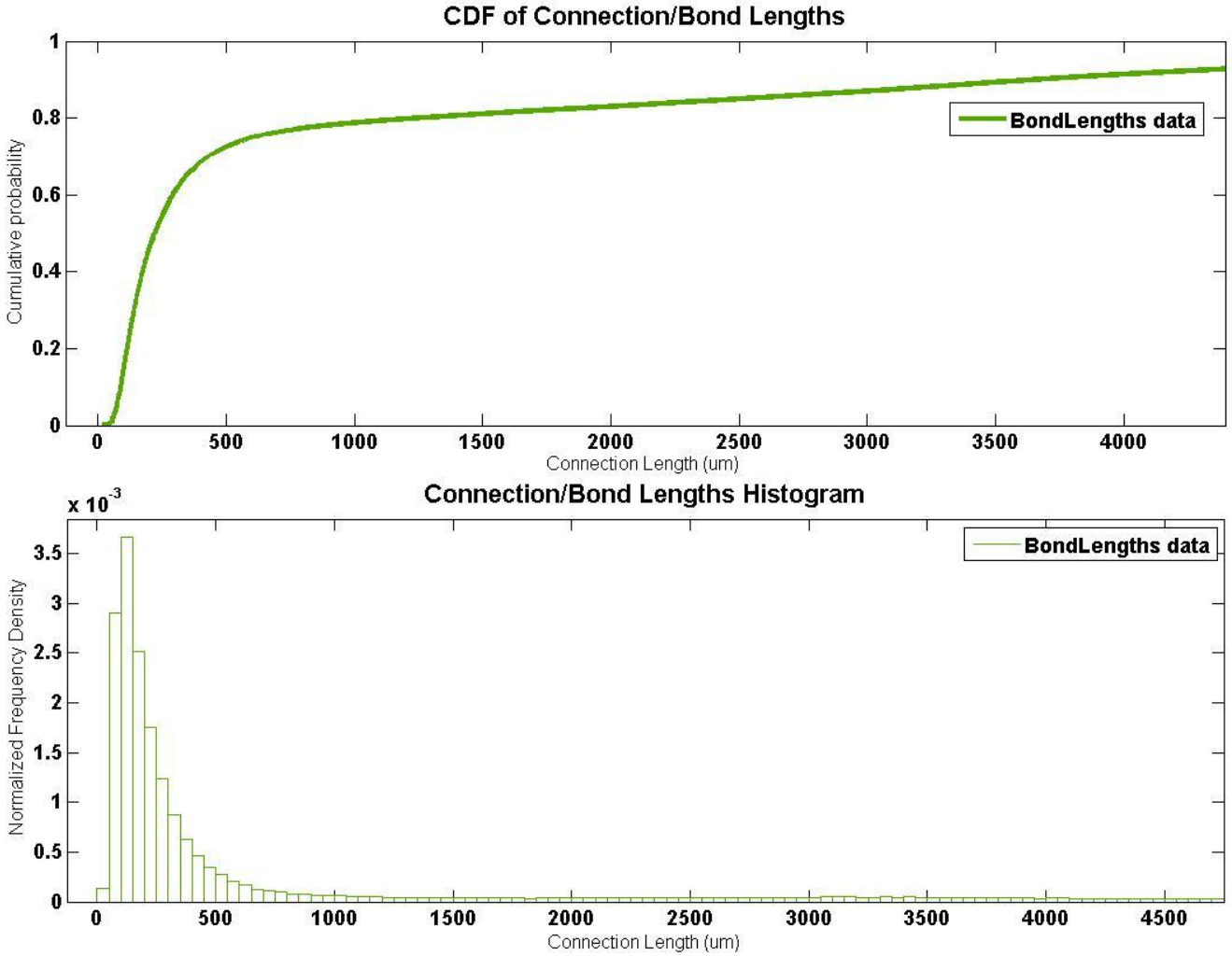

Figure 27 – Shows the broad spread of Bond Lengths, ranging from 100 to 1000 um, to point out the unstructured connectivity present even in a µ-CT length-scale size of carbonate rock.

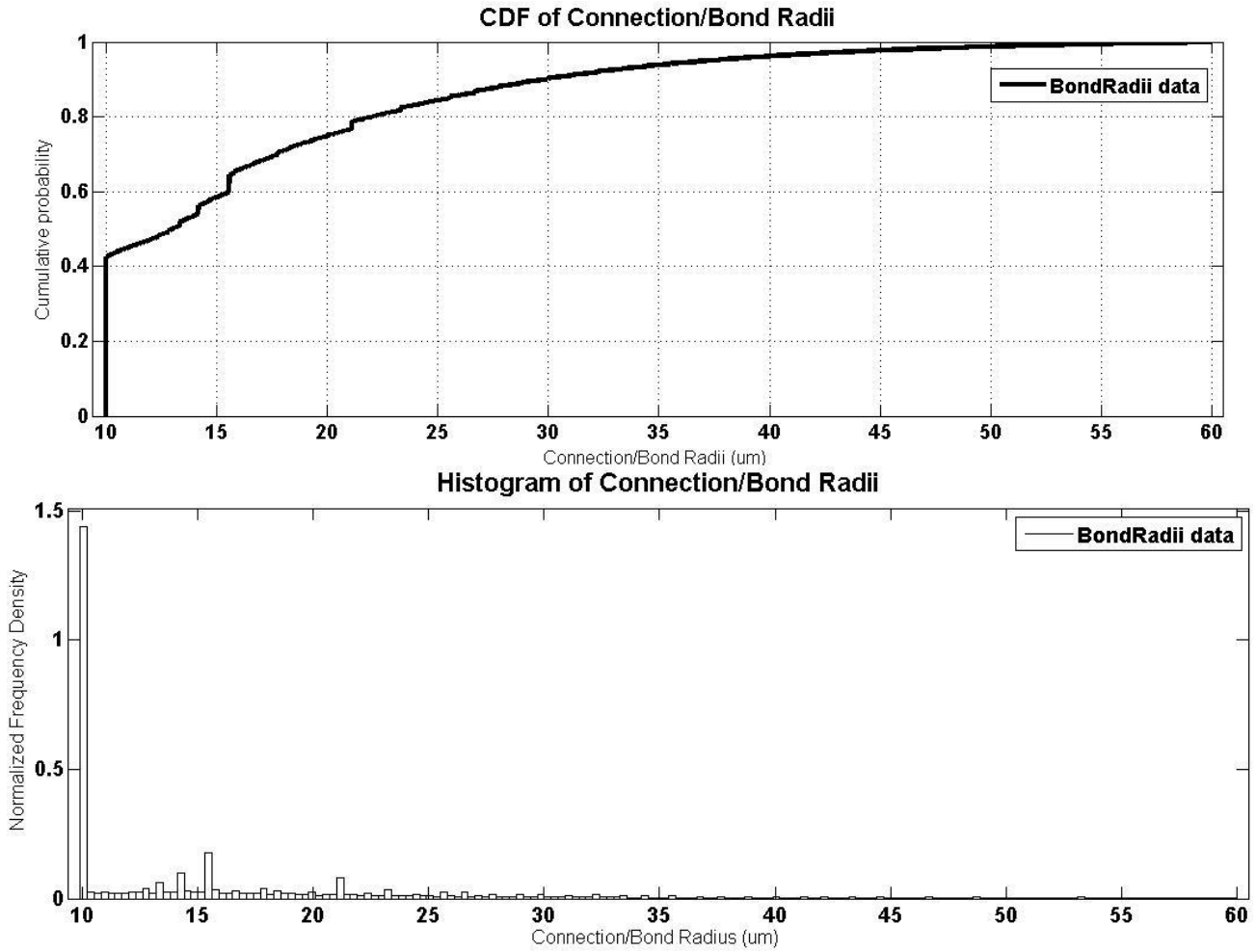

Figure 28 – Shows how the mean radius of a connection is around 10 to 12 um. We observe that a large spread of bond radii as well, and bimodality in the distribution – a significant portion of connections have radii around 15 to 20 um.

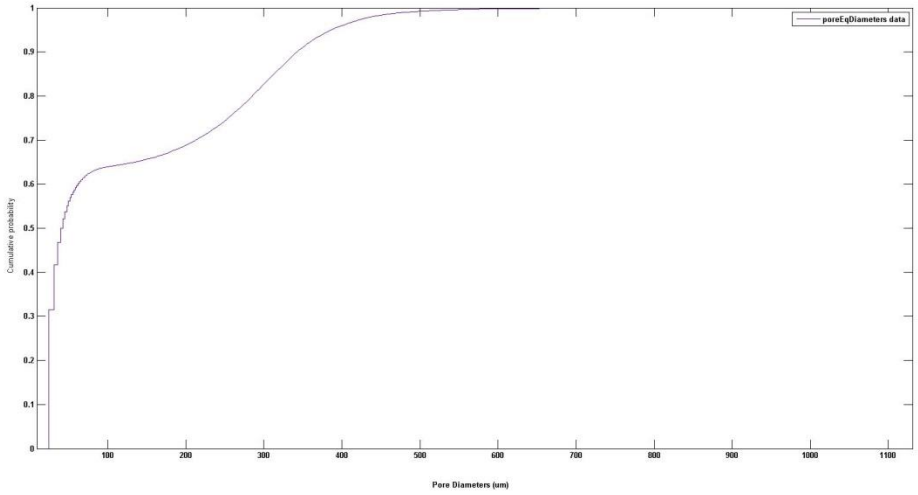

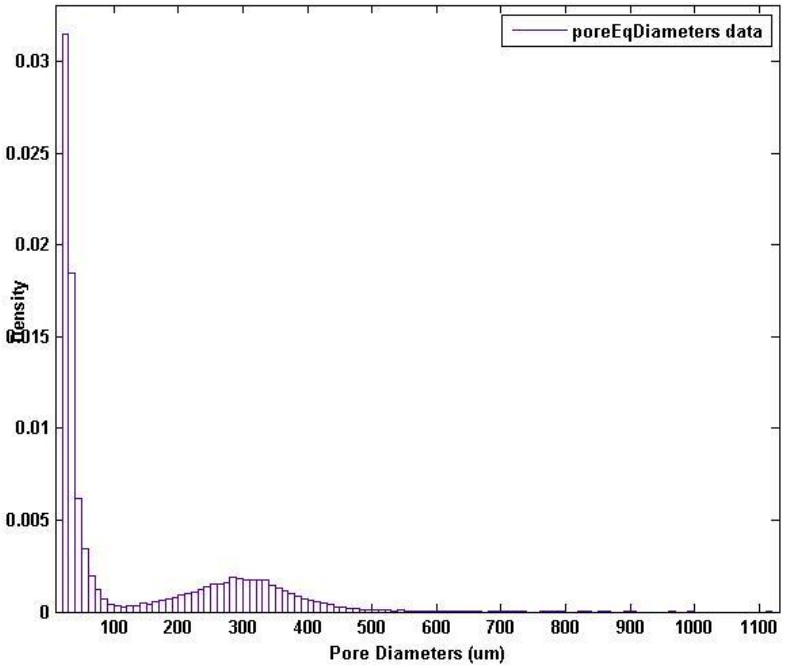

Figure 29 – Shows the bimodality in the distribution of pore-sizes.

3.3 Transmissibility and Diffusivity

The skeleton with nodes and connections can be further examined for flow properties. For convective processes, each connection / bond between the nodes needs to carry transmissibility, while for diffusive processes each connection should have an associated diffusivity.

Since each of the bonds produced from the skeletonization procedure in AVIZO is essentially a tortuous tube carrying a length and a radius, Poisuille flow is a reasonable approximation for flow between each node. The Hagen-Poisuille equation relates the pressure drop, flow rate and the geometric properties of tube via the following equation.

$$Q = \frac{\boldsymbol{\pi} R^4}{8\mu L}\Delta P \quad \ldots\ldots\ldots\ldots\ldots\ldots\ldots\ldots \text{(3.1)}$$

Where:

R = radius of tube;

μ = viscosity of fluid;

L = Length of tube;

ΔP = Pressure differential across both ends of the tube.

This is very analogous to Darcy's equation:

$$Q = 6.3283e - 3 * \frac{kA}{\mu L}\Delta P \quad \ldots\ldots\ldots\ldots\ldots\ldots\ldots\ldots \text{(3.2)}$$

Where:

k = permeability of porous media, md;

A= Cross-sectional area of the flow, ft^2;

μ = viscosity of fluid, cp;

L = Length of media, ft;

ΔP = Pressure differential across both ends of the media, psi.

Q = ft^3 / day

The permeability of the tube is thus:

$$k_{tube} = 1.0132e3 * \frac{R^2}{8} \quad (3.3)$$

Where:

k = permeability of tube, md;

R= Mean radius of tube, μm;

Since the concept of grid-block geometry does not apply between nodes, this allows us to define transmissibility simply using the permeability from Poisuille flow as:

$$Q = T * \Delta P = \frac{\boldsymbol{\pi} R^4}{8\mu L} \Delta P$$

$$T = 6.3283e - 3 * \frac{\boldsymbol{\pi} R^4}{8\mu L} \quad (3.4)$$

Where:

R= mean radius of connection, ft;

μ = viscosity of fluid, cp;

L = mean length of connection, ft;

ΔP = Pressure differential across both ends of the media, psi.

Each tube's permeability can then be used to calculate its diffusivity.

$$\alpha = \frac{k}{\phi \, \mu c_t} \ldots\ldots\ldots\ldots\ldots\ldots\ldots\ldots\ldots\ldots\ldots\ldots\ldots\ldots\ldots\ldots\ldots\ldots\ldots\ldots\ldots\ldots\ldots\ldots\ldots\ldots\ldots\ldots\ldots\ldots\ldots\ldots\ldots. (3.5)$$

Where:

α = Diffusivity

k = permeability of connection, md

Φ = porosity of tube = 1.

c_t= compressibility, 1/psi

For our purposes, we use the diffusivity to calculate the diffusive time-of-flight from one end of the tube to the other:

$$\tau = \frac{L}{\sqrt{\alpha}} = \sqrt{\frac{c_t \mu}{c \; k}} * L \ldots\ldots\ldots\ldots\ldots\ldots\ldots\ldots\ldots\ldots\ldots\ldots\ldots\ldots\ldots\ldots\ldots\ldots\ldots\ldots\ldots\ldots\ldots\ldots\ldots\ldots\ldots\ldots (3.6)$$

Where:

τ = Diffusive time-of-flight of connection, $\sqrt{hr}$

L = length of connection, ft

c_t= compressibility, 1/psi

μ = viscosity of fluid, cp;

c = constant = 2.63678e-4

k= permeability of connection, md

Finally, since the AVIZO skeletonization module works by employing a thinning algorithm, the same pairs of nodes sometimes are connected by multiple connections. For the purposes of simulation, only 1 connection was accepted between the same pair of nodes, and of the available connections the one with the highest mean radius – highest permeability – was chosen. The volume of the "over-looked" connections was still added to the volume of the node.

3.4 Convective Permeability

A steady-state, incompressible, single-phase *digital*, core-flood was performed on the sample by finding all the nodes on two parallel edge faces (to a tolerance distance) and setting them at a constant pressure with a pressure differential between the two faces. In this way permeability in all three directions may be examined. Figure 30 shows the nodes chosen for a flood in the Z direction.

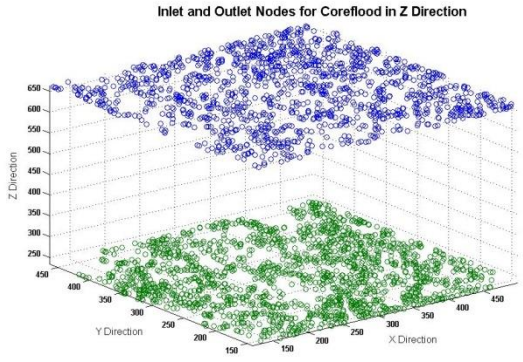

Figure 30 – Shows the position of the inlet and outlet nodes for coreflooding, set to a constant pressure to find the permeability in the Z direction.

The standard way of solving for pressure in every node, is to set up the solution as follows:

$$AX = B \quad \ldots\ldots (3.7)$$

Where:

A = Transmissibility matrix, each element has unit of ft^3/psi

X = Vector of unknown pressures at every node, psi

B = Vector of fluxes into/out of every node, ft^3

The transmissibility matrix is structurally identical to Figure 25, carrying the information of which nodes each is connected to, and with what transmissibility, with the exception of a main diagonal term that contains the sum of all the transmissibilities out of each node. This is suggested by the equation for flux continuity for any given node:

$$Q_i = \left(\sum_{1}^{n} T_{i,j}\right) * P_i - T_{i,1} * P_1 - T_{i,2} * P_2 - T_{i,3} * P_3 \ldots\ldots - T_{i,k} * P_k \ldots\ldots\ldots\ldots\ldots\ldots (3.8)$$

Where;

i / j = index of node, $i \neq j$

k = total number of nodes, $k \neq i$

n = total number of connections out of node i.

$T_{i,j}$ = Transmissibility between node i and node j, ft^3/psi

Q = flux into/out of each node, ft3

P_i = Pressure of node i, psi

The transmissibility properties of the connections within the two faces limit the amount of fluid-flow that will occur. Once the total flux entering/exiting the system is determined, a convective permeability is easily obtained by assuming Darcy's equation again with the appropriate cross-sectional area and length. Table 1 summarizes the results determined for each direction.

Direction	Permeability, md
x	1367
y	1682
z	1219

Table 1 – Shows the permeability obtained from a convective core-flood in each direction.

From the values found for the three directions, **the average is 1423 md**.

The high permeability values are not surprising. However, that such a high value of permeability would be found from such a small sample volume and the level of heterogeneity suggested by the data statistics suggests that there is more information to be gleaned about the transport properties of the rock sample. While a coreflood relates to the steady-state properties of the sample, diffusive processes pick up both the transient and steady-state aspects of the rock sample, and hence potentially reveal more about the fluid flow characteristics through the sample volume.

3.5 Diffusive Properties

Diffusive processes are a highly effective way to the study the transient flow characteristics of the rock sample. For our purposes, the diffusive time-of-flight to a set of seed nodes (pressure source/sink nodes) was populated on the lattice via Dijkstra's method. This was then converted to a "well-test" response using the geometric pressure approximation (Zhou 2013), for subsequent analysis. In our case, we will reconcile the pressure-transient response with the ability to actually visualize the moving drainage volumes inside the μ-CT sample to better study the sample.

3.5.1 Background

A novel semi-analytical approach for the estimation of drainage volume, pressure and rate response without the need for a conventional numerical simulation was proposed by (Xie et al. 2012). The authors expressed the diffusivity equation in terms of drainage volume as shown below.

The diffusivity equation in radial form is given by

$$\frac{1}{A(r)}\frac{\partial}{\partial r}\left(\frac{k}{\mu}A(r)\frac{\partial p(r,t)}{\partial r}\right)=\phi c_t\frac{\partial p}{\partial t} \dots\dots\dots\dots\dots\dots\dots\dots\dots\dots\dots\dots\dots\dots\dots\dots\dots\dots\dots\dots\dots (3.9)$$

The inwardly-directed Darcy flux is given by

$$q(r,t)=\frac{kA(r)}{\mu}\frac{\partial p(r,t)}{\partial r} \dots\dots\dots\dots\dots\dots\dots\dots\dots\dots\dots\dots\dots\dots\dots\dots\dots\dots\dots\dots\dots\dots\dots\dots\dots . (3.10)$$

Flux is inward for a producer and the sign is positive. We will solve these equations for the pressure draw-down during production. Combining **Eq. 3.9 & 3.10**, we obtain:

$$c_t \frac{\partial p}{\partial t} = \frac{1}{\phi A(r)} \frac{\partial q}{\partial r} \quad (3.11)$$

Or,

$$c_t \frac{\partial p}{\partial t} = \frac{\partial q}{\partial V_p(r)} \quad (3.12)$$

This implies that the pressure contours, $p(r,t)$ depend on r only. Extending the above equations in terms of the spatial τ coordinate results in **Eq. 3.13 & Eq. 3.14**:

$$c_t \frac{\partial p}{\partial t} = \frac{\partial q}{\partial V_p(\tau)} \quad (3.13)$$

$$q = c_t \frac{dV_p}{d\tau} \frac{\partial p}{\partial \tau} \quad (3.14)$$

(Xie et al. 2012)'s geometric pressure approximation is shown in **Eq. 3.15** as:

$$c_t \frac{\partial p}{\partial t} = -\frac{q_w}{V_p(t)} \quad (3.15)$$

The drainage volume $V_p(t)$ is obtained by evaluating the drainage volume $V_p(\tau)$ at the depth of investigation $\tau(t)$. However, the authors recognized that there was some ambiguity in this definition. Zhou (2013) proposed an improved geometric pressure approximation given by **Eq. 3.16**.

$$c_t \frac{\partial p}{\partial t} = \frac{\partial q}{\partial V_p(\tau)} \cong -\frac{q_w}{V_p(t)} e^{-\frac{\tau^2}{4t}} \dots\dots\dots\dots\dots\dots\dots\dots\dots\dots\dots\dots\dots\dots\dots\dots\dots\dots\dots\dots\dots\dots\dots\dots\dots (3.16)$$

Integrating the above equation from a finite volume of $V_p(t)$ to infinity where q=0, we get:

$$q(\tau, t) = \frac{q_w}{V_p(t)} \int_{V_p(\tau)}^{\infty} dV_p(\tau) e^{-\frac{\tau^2}{4t}} \dots\dots\dots\dots\dots\dots\dots\dots\dots\dots\dots\dots\dots\dots\dots\dots\dots\dots\dots\dots\dots\dots (3.17)$$

The boundary condition at the wellbore ($V_p(\tau) = 0; q = q_w$) now provides the equation for $V_p(t)$.

$$V_p(t) = \int_0^{\infty} dV_p(\tau) e^{-\frac{\tau^2}{4t}} \dots\dots\dots\dots\dots\dots\dots\dots\dots\dots\dots\dots\dots\dots\dots\dots\dots\dots\dots\dots\dots\dots\dots\dots (3.18)$$

$dV_p(\tau)$ can be written in terms of the Dirac delta function as

$$dV_p(\tau) \cong \sum_m PV_m \delta(\tau - \tau_m) d\tau \dots\dots\dots\dots\dots\dots\dots\dots\dots\dots\dots\dots\dots\dots\dots\dots\dots\dots\dots\dots\dots\dots\dots (3.19)$$

Substituting **Eq. 3.19** in **Eq. 3.18**, we have

$$V_p(t) \cong \sum_m PV_m \int_o^{\infty} \delta(\tau - \tau_m) e^{-\frac{\tau^2}{4t}} d\tau \dots\dots\dots\dots\dots\dots\dots\dots\dots\dots\dots\dots\dots\dots\dots\dots\dots\dots\dots\dots (3.20)$$

The integral of a Dirac delta function becomes the integrand itself. Therefore, the final approximation for $V_p(t)$ is given by:

$$V_p(t) \cong \sum_j PV_j e^{-\frac{\tau_j^2}{4t}} \quad (3.21)$$

Where:

PV = pore volume of gridblock/node i; ft^3;

t = time

τ_i = Diffusive time-of-flight from node i

The summation term allows the analytical expression to be applied to our case where each discrete node carries a volume. So, the effective contribution of each node to the drainage volume varies with time as shown below where each node's pore volume is discounted with the exponential weight.

$$PV_{i_{eff}} = PV_i e^{-\frac{\tau_i^2}{4t}} \quad (3.22)$$

At small time, nodes far away from the seed-nodes, carrying large τ, have an insignificant weight, and at very large time, all connected nodes have weights close to 1, resulting in pseudo-steady state flow. Once $V_p(t)$ is estimated, the well-test derivative (W.T.D.) may be estimated as:

$$W.T.D. = -t \left.\frac{\partial p}{\partial t}\right|_{\tau=0} = 0 \cong t * 0.234 \frac{q_w}{V_p(t)} e^{-\frac{\tau^2}{4t}} \quad (3.23)$$

Where:

q_w = bbl / day = 1 for simplicity

t = time, hours

$V_p(t)$ = drained node volume as a function of time, ft^3

τ = diffusive time of flight at pressure-sink = 0

The radius of investigation has been defined as the distance of peak pressure disturbance from an impulse source or sink (Lee 1982). Mathematically, this refers to the distance where:

$$\frac{\partial^2 p}{\partial t^2} = 0 \ldots\ldots\ldots\ldots\ldots\ldots\ldots\ldots\ldots\ldots\ldots\ldots\ldots\ldots\ldots\ldots\ldots\ldots\ldots\ldots\ldots\ldots\ldots\ldots\ldots\ldots\ldots\ldots\ldots\ldots.\ldots.(3.24)$$

The derivative of **Eq. 3.16** with respect to t will hence be used to obtain the depth of investigation:

$$0 = \frac{\partial}{\partial t}\left[\frac{1}{V_p(t)}e^{-\frac{\tau^2}{4t}}\right] = \left(-\frac{1}{{V_p}^2}\frac{dV_p}{dt} + \frac{1}{V_p}\frac{\tau^2}{4t}\right)e^{-\frac{\tau^2}{4t}} \ldots\ldots\ldots\ldots\ldots\ldots\ldots\ldots\ldots\ldots\ldots\ldots\ldots(3.25)$$

Where the derivative of **Eq 3.18** is used to obtain:

$$\frac{dV_p}{dt} = \int_0^\infty \frac{\tau^2}{4t} dV_p(\tau)e^{-\frac{\tau^2}{4t}} \ldots\ldots\ldots\ldots\ldots\ldots\ldots\ldots\ldots\ldots\ldots\ldots\ldots\ldots\ldots\ldots\ldots\ldots\ldots\ldots\ldots\ldots.\ldots(3.26)$$

Substituting **Eq. 3.26** in **Eq. 3.25** results in analytical expression for the depth of investigation:

$$\tau^2 = \frac{1}{V_p(t)}\int_0^\infty \tau^2 dV_p(\tau)e^{-\frac{\tau^2}{4t}} \ldots\ldots\ldots\ldots\ldots\ldots\ldots\ldots\ldots\ldots\ldots\ldots\ldots\ldots\ldots\ldots\ldots\ldots\ldots\ldots\ldots.\ldots(3.27)$$

Here **Eq. 3.18** is used as the expression for the drainage volume as a function of time. In the grid or the lattice sense, the integrals in **Eq. 3.27** are approximated as summations over each block/node:

$$\tau^2(t) \approx \frac{\sum_j {\tau_j}^2 PV_j e^{-\frac{{\tau_j}^2}{4t}}}{\sum_j PV_j e^{-\frac{{\tau_j}^2}{4t}}} \ldots\ldots\ldots\ldots\ldots\ldots\ldots\ldots\ldots\ldots\ldots\ldots\ldots\ldots\ldots\ldots\ldots\ldots\ldots\ldots\ldots\ldots\ldots\ldots (3.28)$$

For a homogeneous reservoir **Eq. 3.27** is evaluated to be linearly related to time as:

$$\tau^2 = m * t \ldots\ldots\ldots\ldots\ldots\ldots\ldots\ldots\ldots\ldots\ldots\ldots\ldots\ldots\ldots\ldots\ldots\ldots\ldots\ldots\ldots\ldots\ldots\ldots\ldots\ldots\ldots\ldots\ldots\ldots\ldots.. (3.29)$$

Where:

$m = 2, 4, 6$ for 1D, 2D and 3D cases respectively.

This also means that for the classic flow regimes:

$$\frac{\tau^2}{4t} = n \ldots\ldots\ldots\ldots\ldots\ldots\ldots\ldots\ldots\ldots\ldots\ldots\ldots\ldots\ldots\ldots\ldots\ldots\ldots\ldots\ldots\ldots\ldots\ldots\ldots\ldots\ldots\ldots\ldots\ldots\ldots.. (3.30)$$

Where:

$n = \frac{1}{2}, 1, \frac{3}{2}$ for 1D, 2D and 3D cases respectively.

This suggests that a plot of τ^2 that reveals a linear relationship with time or a constant value obtained for $\frac{\tau^2}{4t}$ can be used as diagnostic to gauge the geometry of the flow into the source or sink. We will apply this result in the analysis of our model.

3.5.2 Results

Figure 31 shows the nodes found along an imaginary line in the z-direction through the center of the sample (to a tolerance) that were chosen as a set of seed-nodes (τ =0) for the Dijkstra's algorithm as pressure-sink nodes.

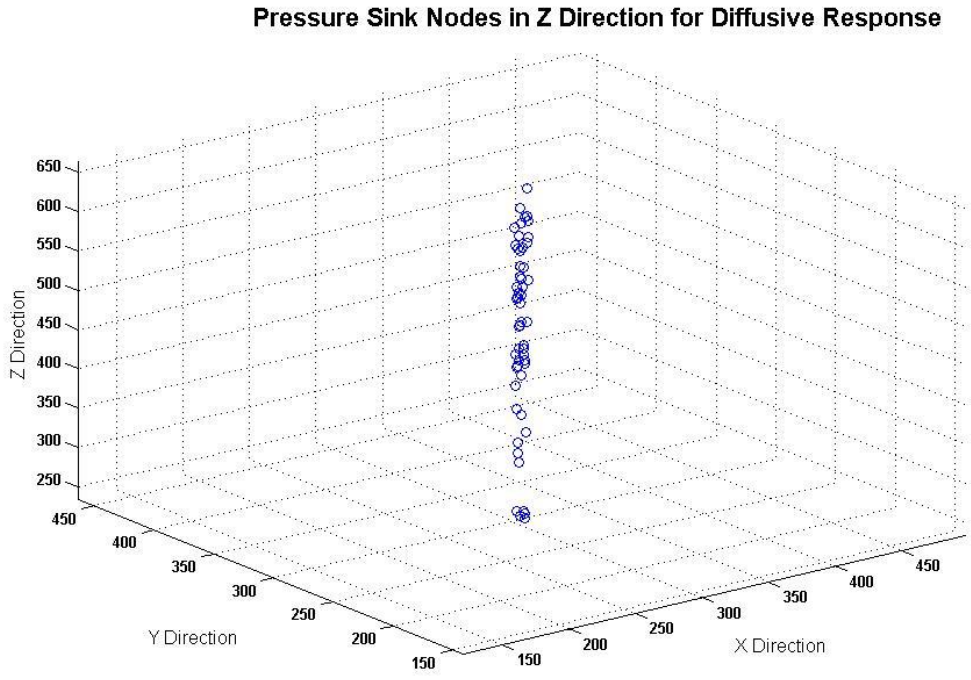

Figure 31 – Shows the location of the pressure-sink nodes. This is analogous to vertical "well" at which the pressure-transient response is measured.

Since the convective permeability estimate is also quite high and the size of the sample is so small, we expect the system to go to PSS fairly quickly. Considering that we have built an unstructured lattice, and the data-statistics suggest a high level of heterogeneity, we certainly don't expect radial flow. However we do expect a period when flow is infinite-acting. Finally, since the nodes themselves have finite volumes, we expect to see a unit-slope ("well-bore"-storage effects) in the very early-time as well. Essentially, we expect that the response will be Unit-slope → 0 slope → Unit slope. We can then estimate permeability using:

$$k = 0.234 * \frac{70.6qB\mu}{m'h} \quad \ldots\ldots (3.31)$$

Where:

q = flow rate, bbl /day = 1 for simplicity

m' = level of derivative.

h = thickness, ft

μ = viscosity, cp

However the result obtained is very different, as is shown in Figure 32 below.

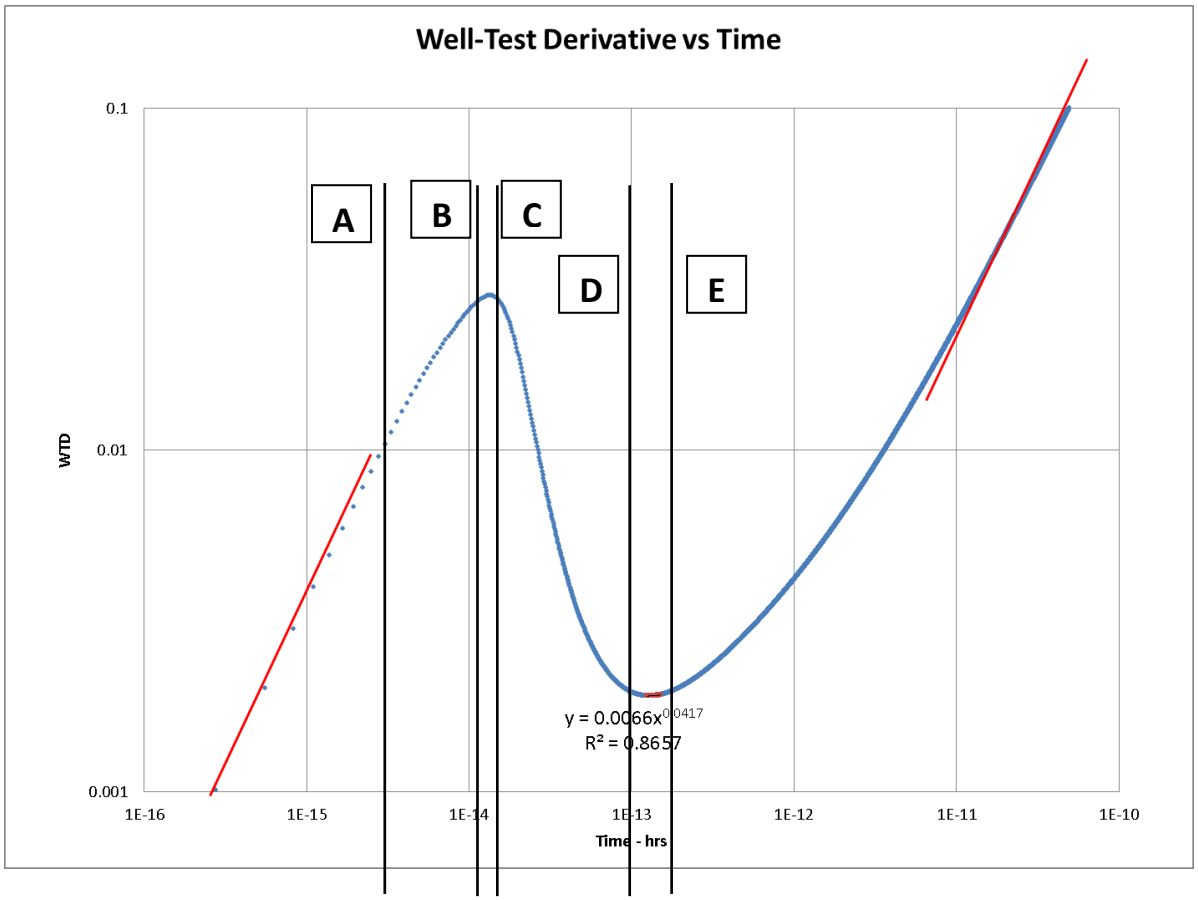

Figure 32 – Shows the pressure-transient response obtained for the line of pressure-sink nodes shown in Figure 31.

Some immediate observations are presented below:

1. There is certainly no justification for a period of "well-bore" storage effect lasting 3 log-cycles of time. I.e. this is not "node"-storage effect.

2. There is also no period where the system is infinite-acting. In fact estimates of permeability from the region D → E are 2 orders of magnitude more than the

convective permeability estimates (~61 Darcy). Clearly this portion of the data does not refer to an infinite-acting regime and is purely an inflection point.

3. Even at very late time, the gradient is only very nearly equal to a unit-slope but not exactly like what we observed at early-time. This suggests some kind of transient activity is still taking place within the rock.

A log-log $V_p(\tau)$ against τ plot was attempted in Figure 33 below. Considering that τ is a spatial co-ordinate, an exponent of around 1, 2, or 3 usually suggests something about the geometry of the flow: Linear: - $V \cong 2\pi x_f h * \tau$, Cylindrical: - $V \cong \pi * \tau^2 * h$, or Spherical: - $V \cong \frac{4}{3}\pi * \tau^3$. In our case, the exponent is in fact less than 1 and yet the correlation is an extremely strong one. This emphasizes the unstructured nature of the flow occurring in the rock. These conclusions also lead us to suspect that this is in fact a dual-porosity signature. This was unexpected considering the small dimensions of the sample.

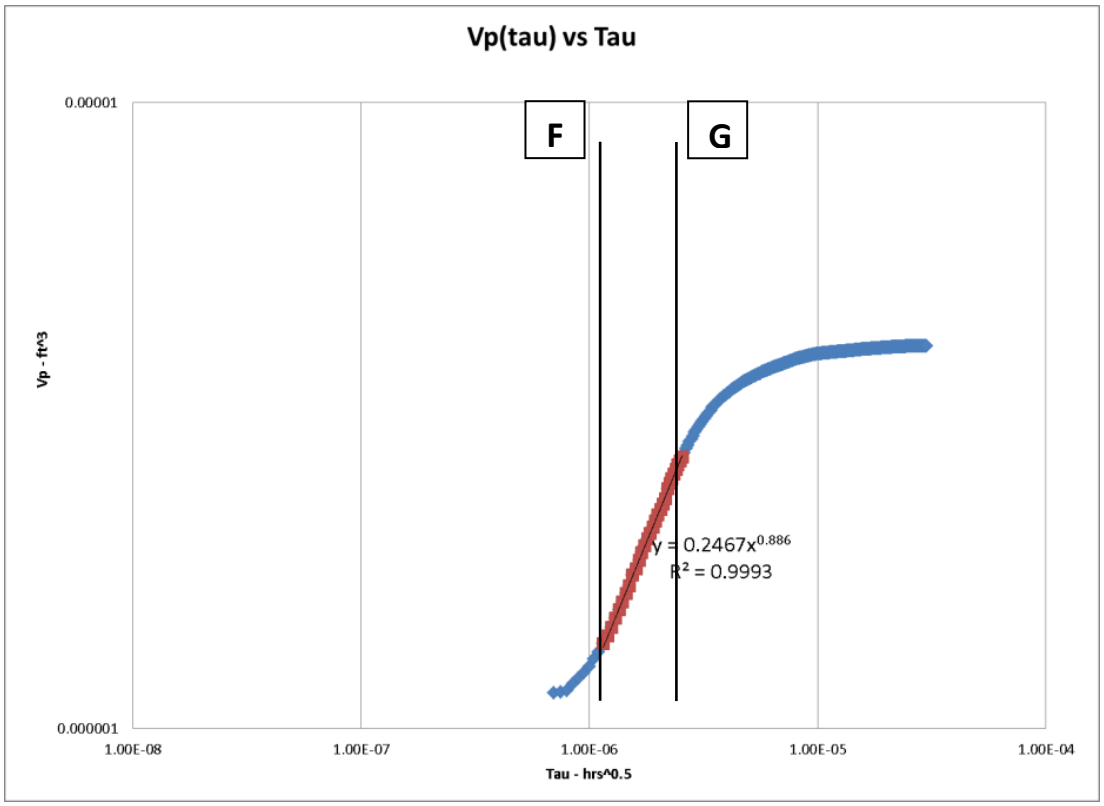

Figure 33 – Shows how the log-log plot of V_p (τ) against τ fails to evolve an exponent that reveals a recognizable geometry of the drainage.

A plot of the depth of investigation, τ^2 and τ^2 /4t, as suggested by **Eq. 3.29** and **Eq. 3.30**, can also suggest the nature of the flow. These are shown in Figure 34 and Figure 35. Figure 34 points out that the relationship between the depth of the investigation and time is non-linear. We note also that the plot of τ^2 /4t in Figure 35 does not suggest any progression of horizontal lines around ½, 1, or 3/2 which would indicate classic flow regimes. In late time however, as the denominator t grows much faster than τ^2, the term tends toward 0. The two figures together suggest that the geometry of the flow into the

sink nodes does not correspond to any classic or known flow geometries and thus also explains why the exponent from a log-log $V_p(\tau)$ against τ plot is not 1, 2 or 3.

We seek to visualize the geometry of the drainage at times A→E suggested in Figure 32 using **Eq. 3.21 - 3.22.** In the following figures, nodes were considered to contribute the drainage volume if at the time of evaluation they carried a weight > 0.05, shown below:

$$weight = e^{\frac{\tau^2}{4t}} \dots\dots\dots\dots\dots\dots\dots\dots\dots\dots\dots\dots\dots\dots\dots\dots\dots\dots\dots\dots\dots\dots\dots\dots\dots\dots\dots.. (3.32)$$

Figure 36 to Figure 40 highlight the drainage volumes as a function of time. Figure 41 highlights the drainage volume as a function of τ in the region suggested in Figure 33 above. The letters A to G represent actual times (t) or taus (τ), and not regions of the curves.

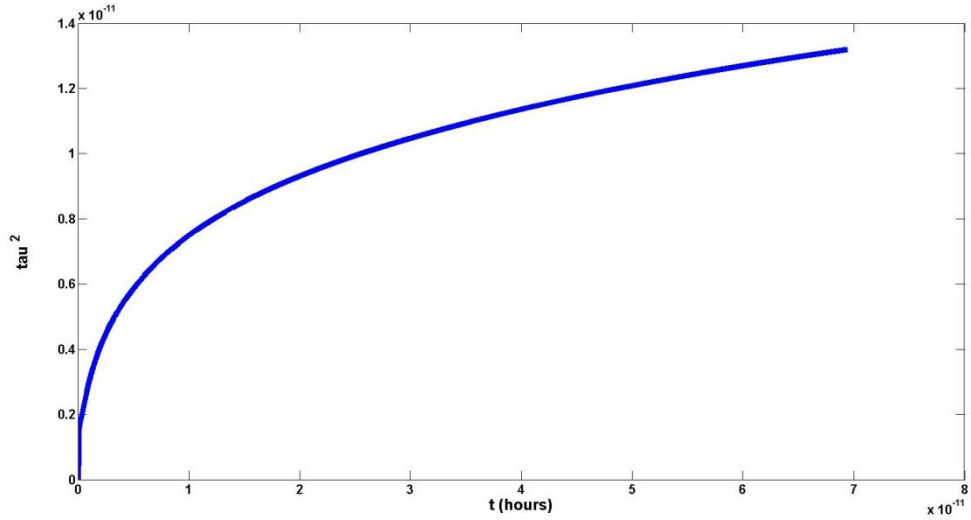

Figure 34 – Shows that the depth of investigation does not increase linearly with time, suggesting that the dominant flow regimes are not the classic ones.

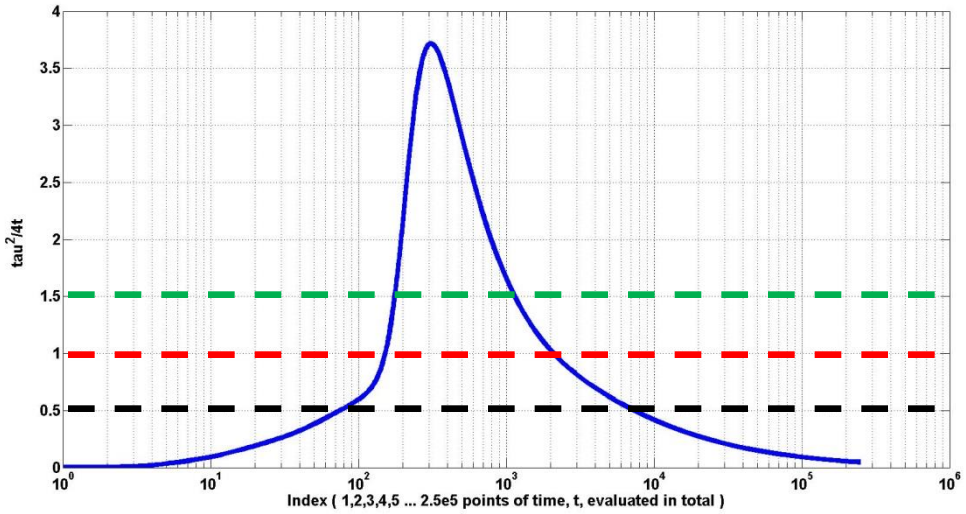

Figure 35 – Shows that τ^2 /4t does not evaluate out to the known constant values that would suggest classic flow regimes.

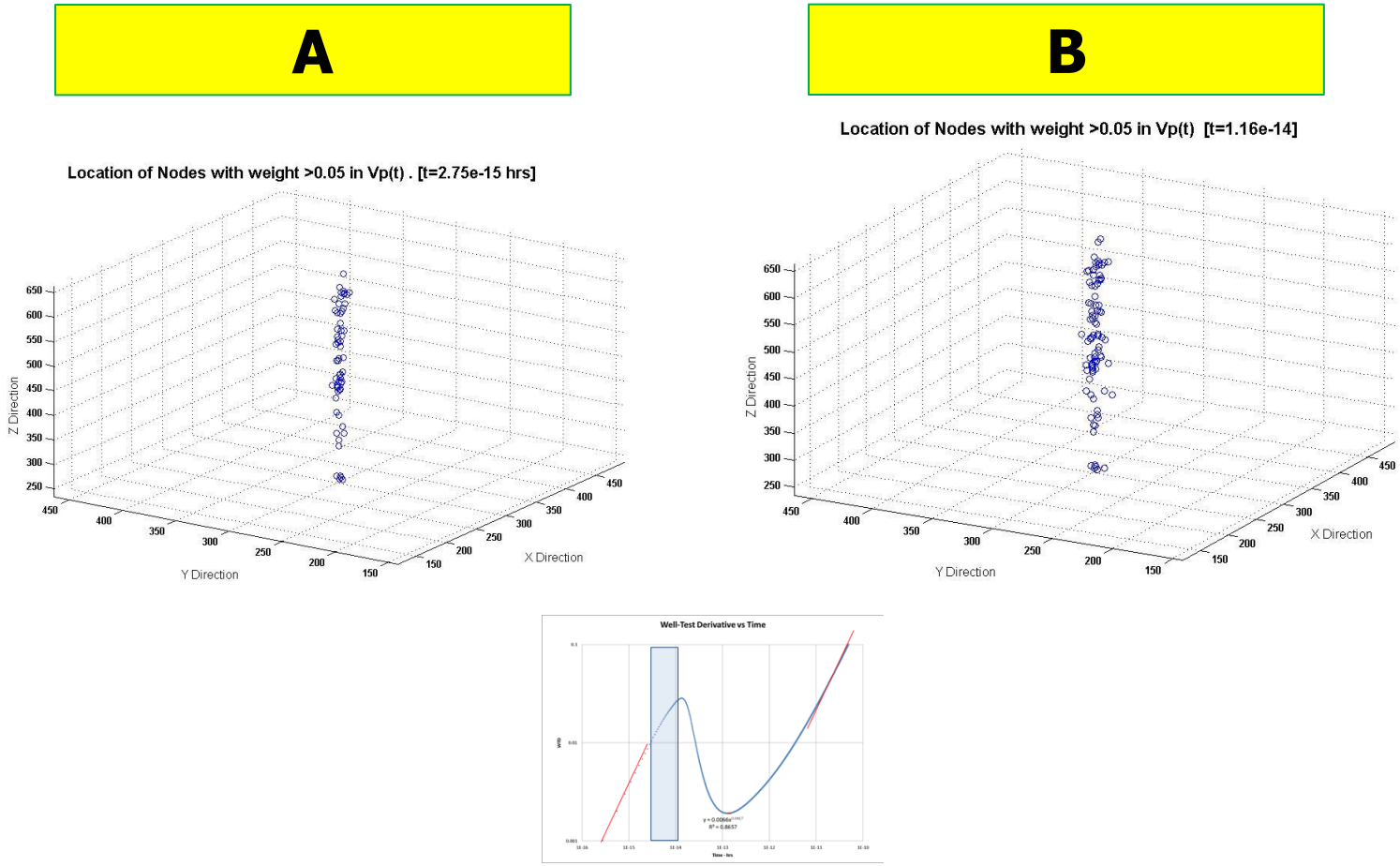

Figure 36 – Shows the drainage volumes from time A to time B, from just after the end of "node-storage" effect to the first inflexion point.

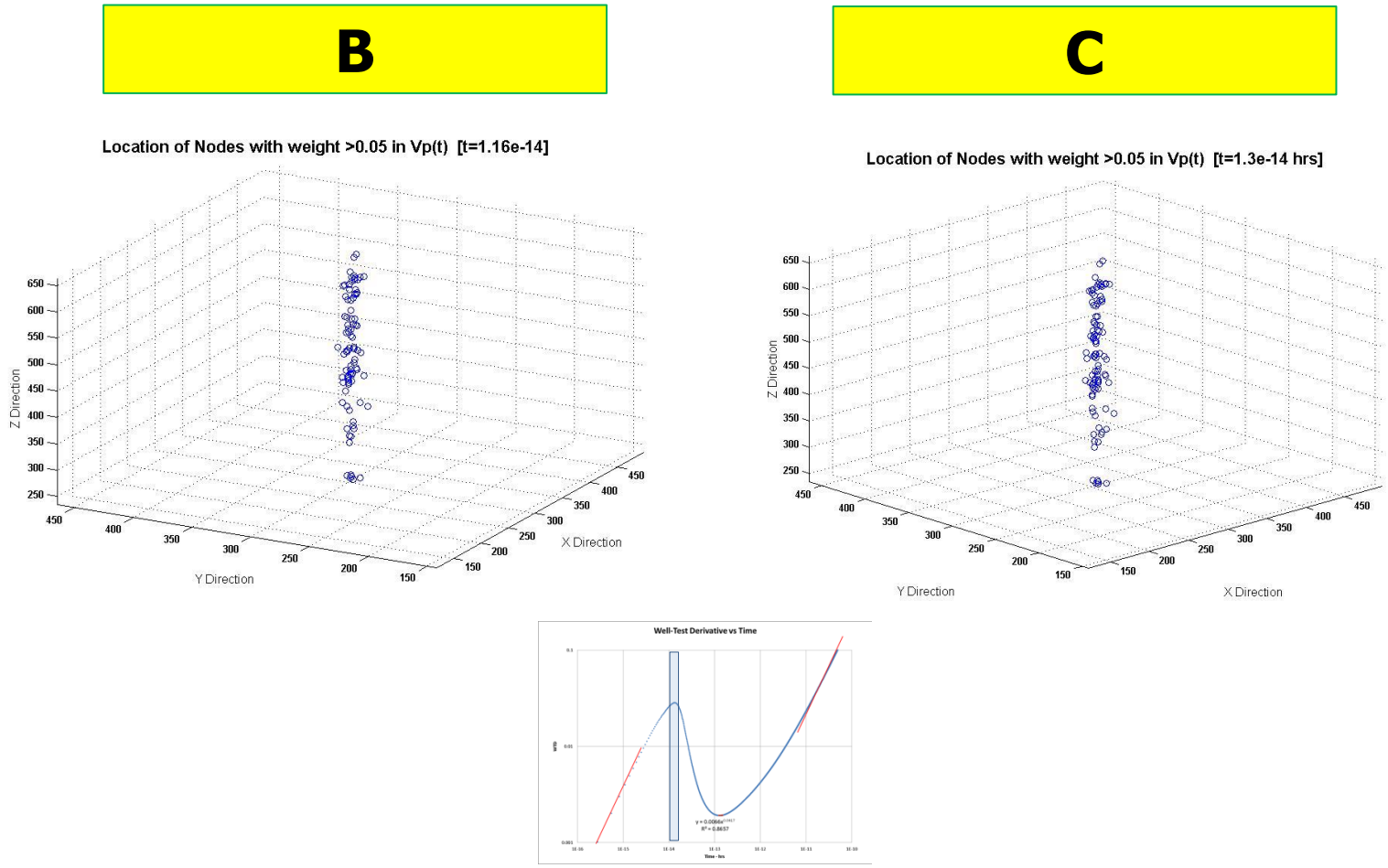

Figure 37 – Shows the drainage volumes from time B to time C, around the first inflexion point.

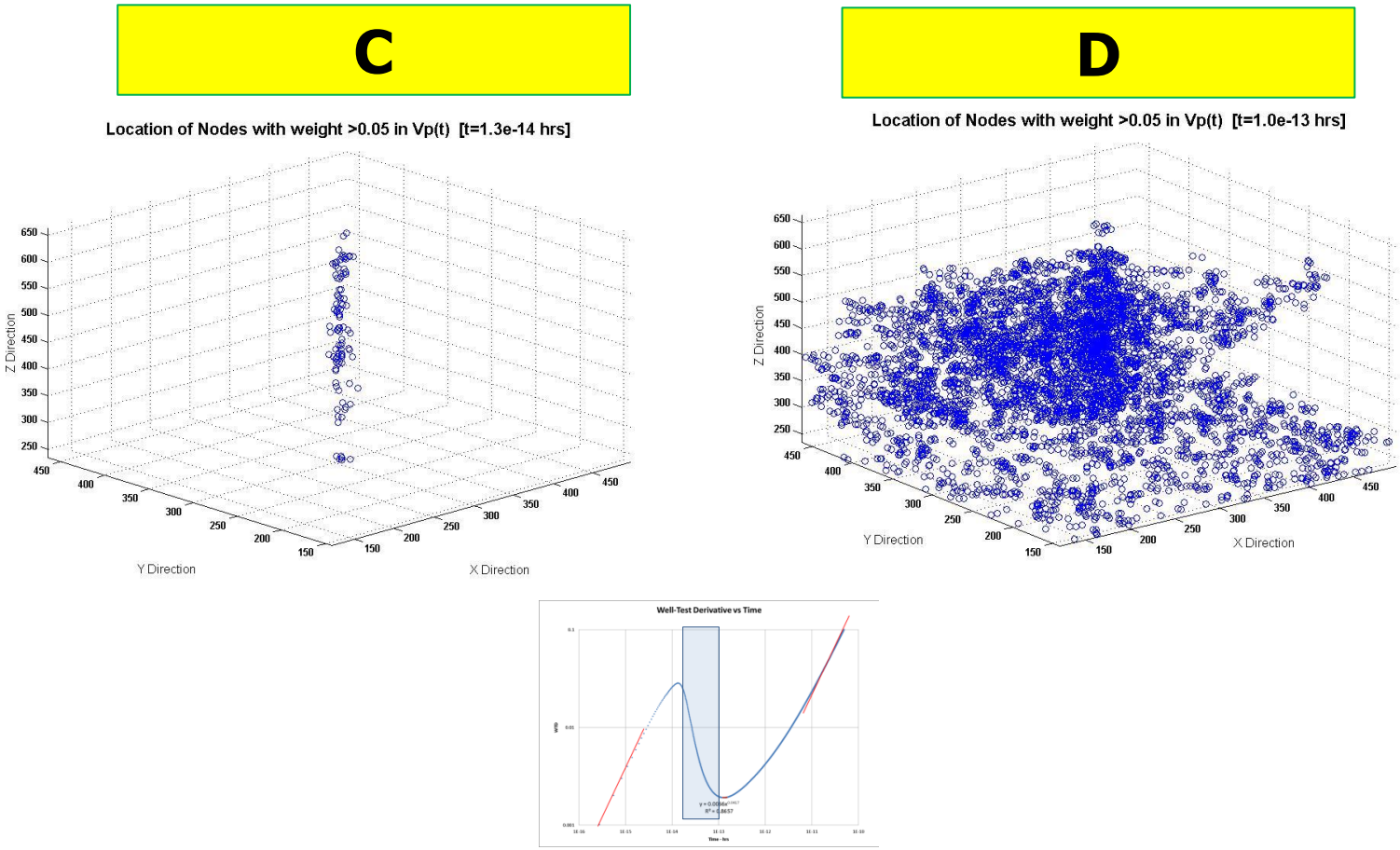

Figure 38 – Shows the drainage volumes from time C to time D, from the end of the first inflexion point to the beginning of the second, and reveals a highly connected sub-volume of the rock that connects one end of the rock to the other.

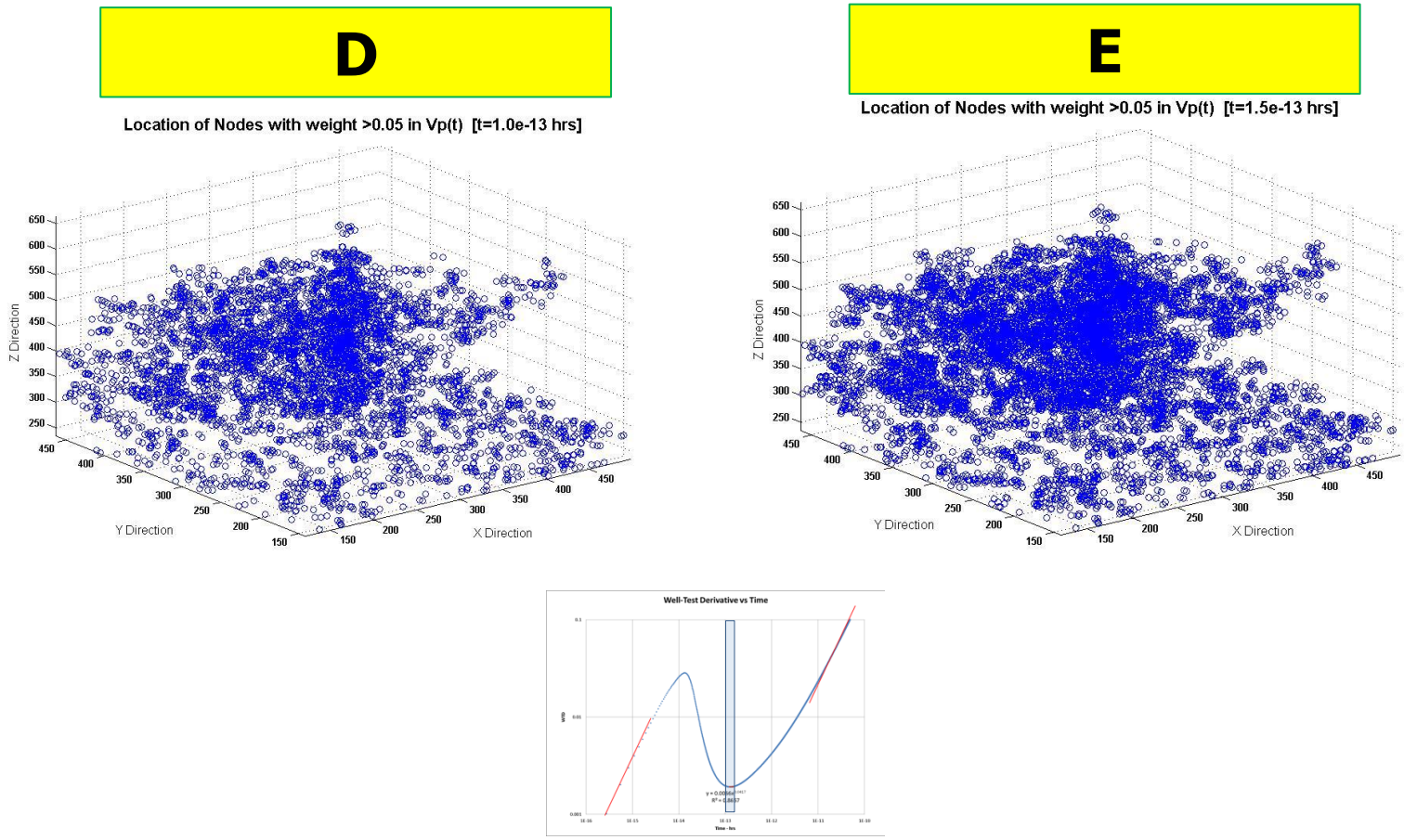

Figure 39 – Shows the drainage volumes from time D to time E, around the second inflexion point, and suggests that all additional volumes drain into the sub-volume suggested in Figure 38.

E

PSS

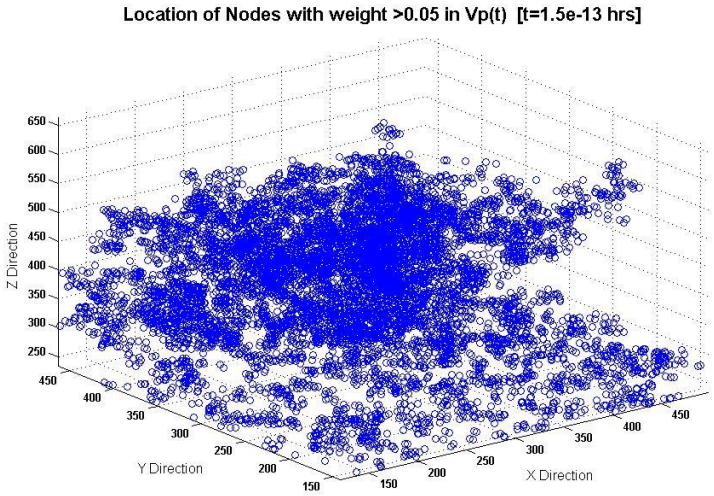

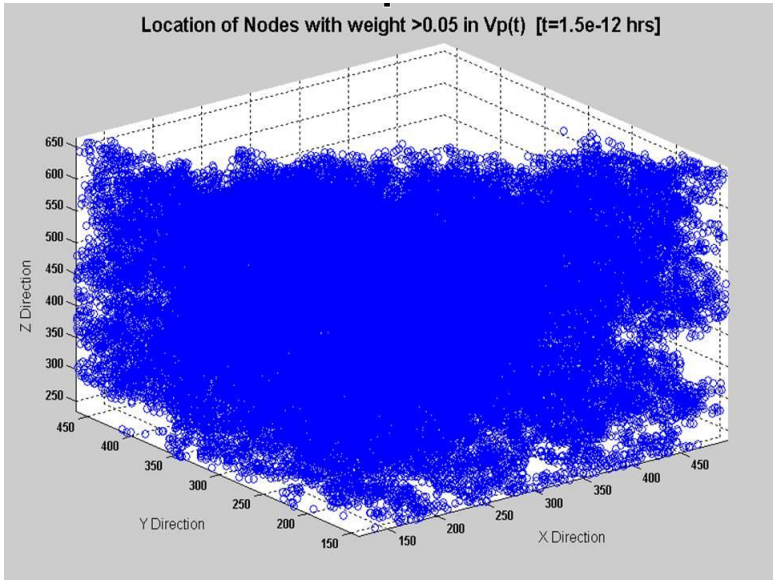

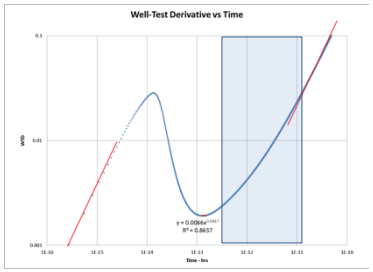

Figure 40 – Shows the drainage volumes from time E onwards and again suggests that the additional nodes drain into the sub-volume suggested in Figure 38.

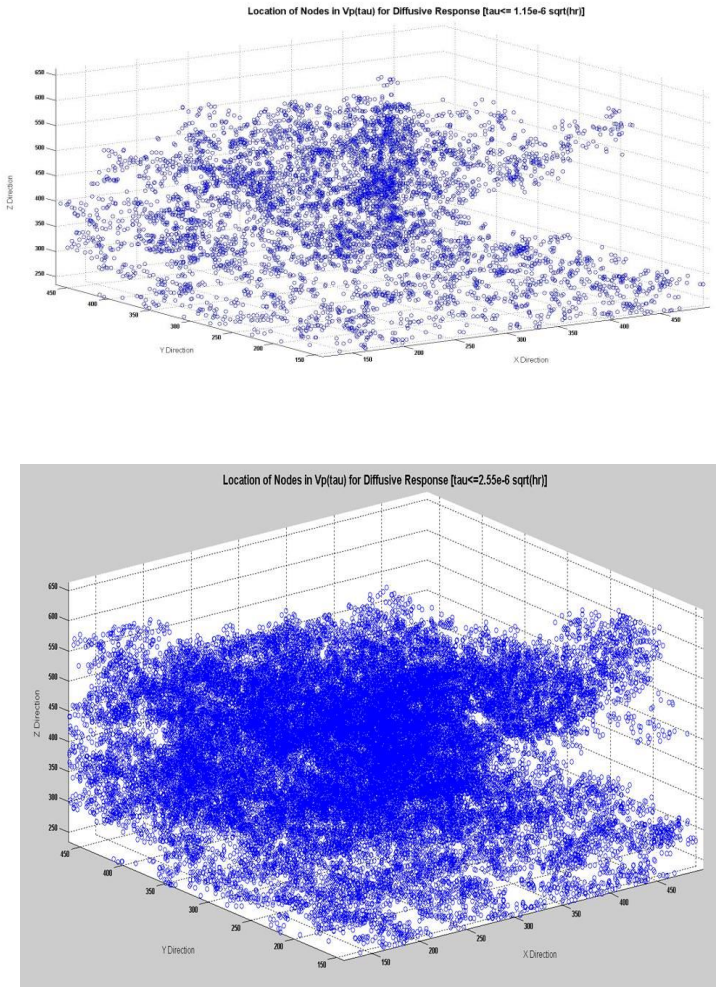

Figure 41 – Reaffirms the unstructured geometry of the propagating drainage volume from tau F to tau G and supports the idea that nodes drain into the highly-connected sub-volume of rock.

3.5.3 Discussion

The evolution of drainage volumes reveals the high level of unstructured-ness in such small sample of rock. The visualization of the flow-paths in the rock allows us to reach the following conclusions:

1. Figure 38, highlights a sub-volume of rock that effectively acts as a short circuit of connectivity.

2. Once the "depth-of-investigation" hits any node in that subset of nodes, the entire subset, which stretches from one end of the rock to the other, is activated. Because this sub-volume does not have any clear geometry of its own, the geometry of the subsequent flow is completely altered from the original.

3. This also suggests a system akin to a dual-porosity model. In our rock volume, the nodes of the sub-volume effectively become the new "seed-nodes" into which the rest of the rock drains. This explains the strong response on the log-log plot of $V_p(\tau)$ vs. τ. Essentially, there is a sequence to the flow: from the rest of the rock into the nodes of the sub-volume, and from the sub-volume into the original sink-nodes.

Lower-Limit τ - hrs^0.5	Upper-Limit τ - hrs^0.5	Number of Nodes	Avg Number of Connections Per Node
0.00E+00	5.00E-08	53	3.452830189
5.00E-08	1.00E-07	3	4
1.00E-07	1.50E-07	1	4
1.50E-07	2.00E-07	7	6.142857143
2.00E-07	2.50E-07	9	3.777777778
2.50E-07	3.00E-07	4	22
3.00E-07	3.50E-07	8	6
3.50E-07	4.00E-07	13	2.923076923
4.00E-07	4.50E-07	13	4
4.50E-07	5.00E-07	15	11.4
5.00E-07	5.50E-07	17	4.176470588
5.50E-07	6.00E-07	18	4.722222222
6.00E-07	6.50E-07	13	3.769230769
6.50E-07	7.00E-07	2022	12.71364985
7.00E-07	7.50E-07	50	2.86
7.50E-07	8.00E-07	182	3.346153846
8.00E-07	8.50E-07	260	5.811538462
8.50E-07	9.00E-07	366	3.672131148
9.00E-07	9.50E-07	427	3.93911007

Table 2 – Shows a table of the number of nodes and their average number of connections per node, for each increment of τ. Specifically, it shows that the sub-volume consists of around 2000 nodes, each with nearly 13 connections, much higher than the mean of 3 connections per node.

Table 2 shows the number of nodes and the average number of connections per node, for each increment of τ. The high-connectivity sub-volume is highlighted as consisting of approximately 2000 nodes each having about 13 connections. Essentially this high-connectivity sub-volume is shown in the top image of Figure 41. The fact that the number of nodes jumps nearly 2 orders of magnitude within such a small increment of τ (the highlighted black row) supports conclusion 2 and also highlights the bimodal nature

of the connectivity in the sample. The nodes encountered before and in the highlighted row refer to the primary pore-volumes, while all nodes encountered beyond the highlighted row are nodes in the secondary pore-volume. We recall the observation made from Figure 26 that the vast majority of the nodes have on average 5 or less connections. Yet it is worthwhile to point out that it is instead the small percentage of nodes with more than 12 connections (highlighted black row) that completely dominate and alter the flow behavior.

In discussing the impact of the high-connectivity sub-volume and its geometric implications, we revisit **Eq. 3.16**. The denominator $V_p(t)$ effectively controls the behavior of the well-test derivative. As highlighted by Figure 38, as soon as the depth-of-investigation hits any of the nodes in the high-connectivity region, there is a large and very quick increase in $V_p(t)$ that causes the well-test derivative to rapidly drop. Also, since this expansion of $V_p(t)$ is unstructured and lacks any distinct shape, the subsequent transient behavior beyond the inflexion point does not produce any power-law relationships with known exponents.

3.5.4 Further Analysis and Discussion: Nodes along Lines in the X and Y Directions

Armed with these conclusions, we seek to corroborate these findings via a different orientation of seed nodes. Identical calculations were performed for a line of sink-nodes through the center of the sample in the X direction (through the y-z plane) and in the Y direction (through the x-z plane).

Figure 42 shows the location of the pressure-sink nodes in a line in the X and Y directions, and Figure 43 shows the well-test-derivative response for each. Figure 44 shows the pressure-derivative response for all three directions on the same plot. While the sub-volume may have been reached at different times, the overall behavior is still similar.

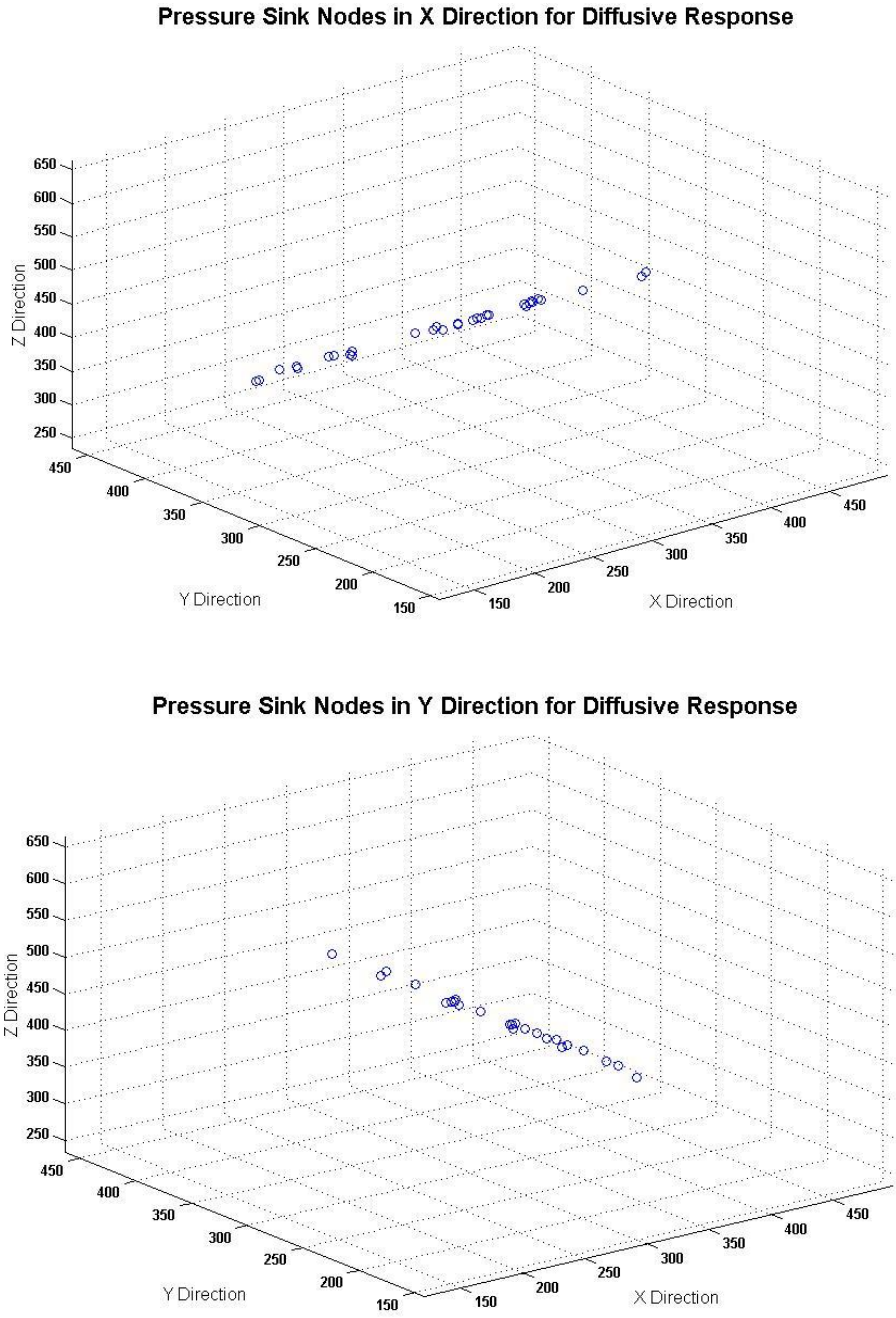

Figure 42 – Shows the location of the pressure-sink nodes. This is analogous to horizontal "well" (sans gravity effects) at which the pressure-transient response is measured.

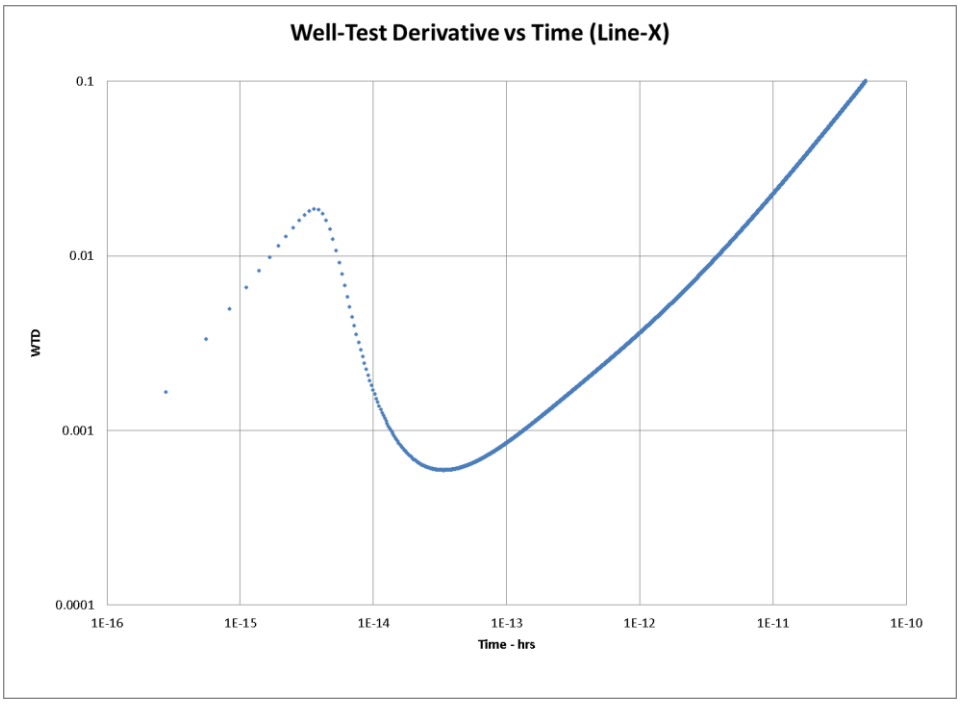

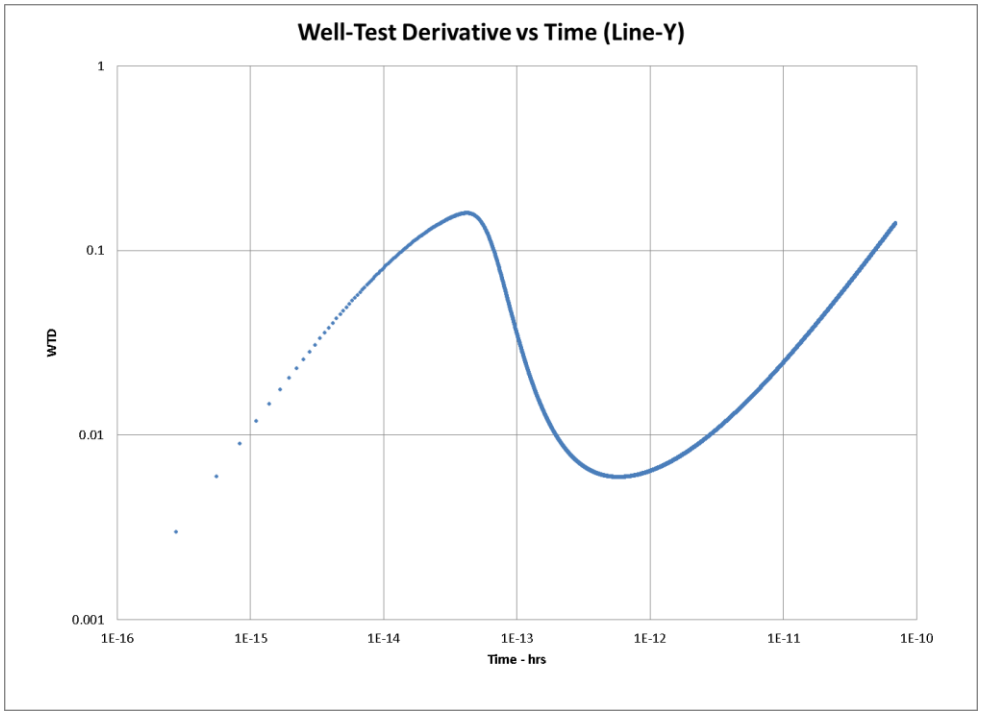

Figure 43 – Shows the well-test derivative obtained for the line of pressure-sink nodes in X and Y directions..

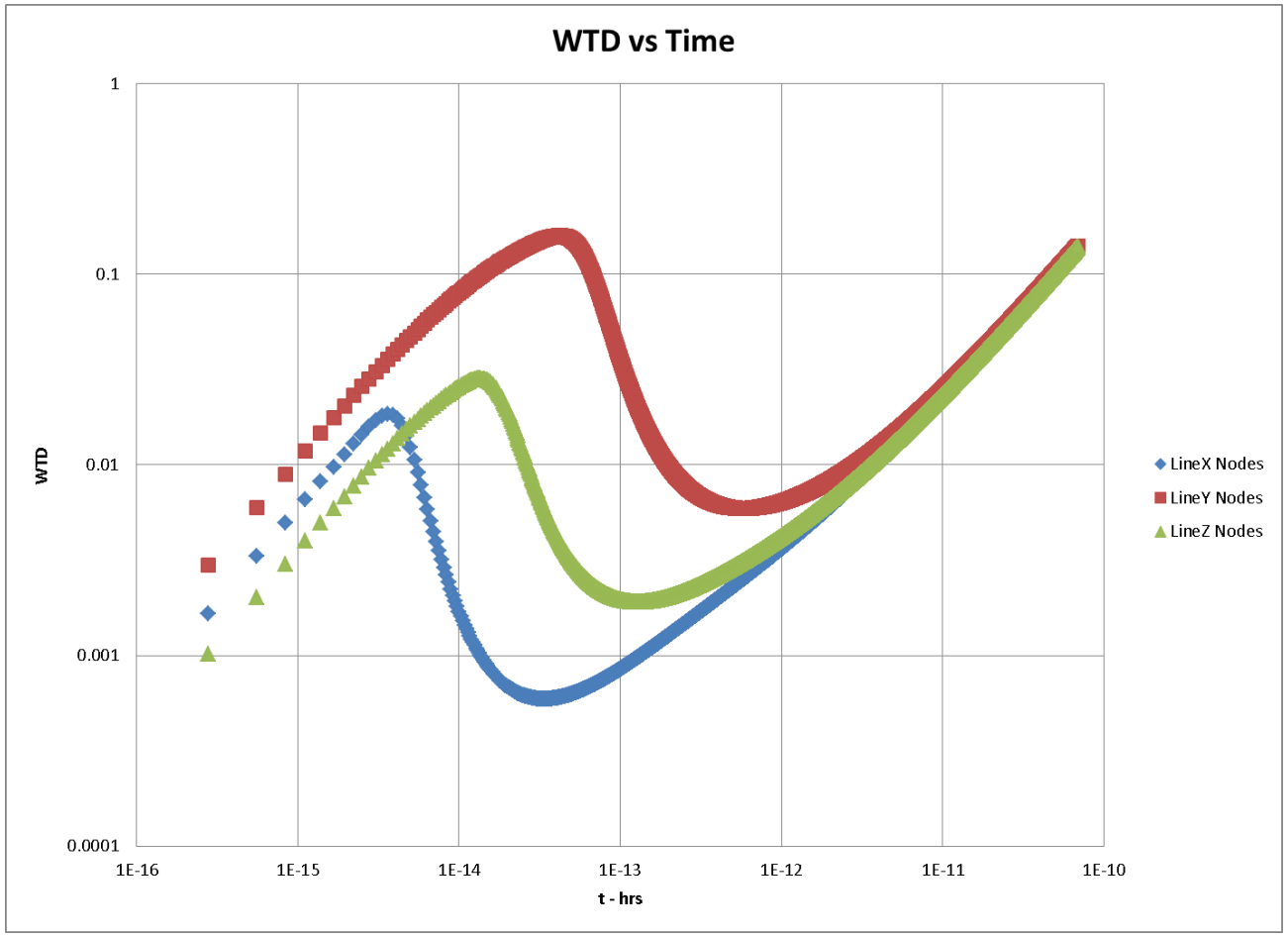

Figure 44 – Compares the pressure-derivative responses for sink nodes in a line for all three directions on the same plot.

The signatures obtained for both orientations of pressure-sink nodes are not surprising. The initial "well-bore" / "node" storage effects before a rapid decline as the highly connected sub-volume change the flow geometry completely. The time taken to the reach the first inflexion point – when the depth-of-investigation first reaches a node in the critical sub-volume triggering the dual porosity-type response – is much sooner for the line of nodes in the X direction than Y. Essentially, the only difference between the two can be attributed to how far the sink-nodes are from the critical sub-volume.

Figure 45 shows the $V_p(\tau)\ vs\ \tau$ plots on a log-log scale for each response. As expected, the exponent evolved for the sink-nodes in the X direction is not useful, and is similar to that obtained for the Z direction due to the unstructured nature of the flow from rock to sub-volume, and sub-volume to sink nodes.

Surprisingly however, the exponent evolved for the sink-nodes in the Y direction is approximately 1.2 which suggests some sort of linear-flow. While this may be a co-incidence, we can also speculate that this may be because the sink-nodes chosen for this direction are actually in the plane of the critical sub-volume, causing the system to in effect drain akin to a well with a vertical fracture. While the visual in 3D may be misleading, Figure 46 suggests that this may indeed be a valid approximation. If this is true, permeability may be approximated using a point in the half-slope region beyond the second inflexion point, with a half-length along the X direction. The equations used are as follows:

$$m_{lf} = 2\frac{\Delta p'}{\sqrt{\Delta t}} \dots\dots\dots\dots\dots\dots\dots\dots\dots\dots\dots\dots\dots\dots\dots\dots\dots\dots\dots\dots\dots\dots\dots\dots\dots\dots\dots\dots\dots\dots\dots .\dots\dots\dots\dots\dots\dots . (3.33)$$

$$x_f\sqrt{k} = \left(\frac{4.064 * 0.234 * \Delta qB}{m_{lf}h}\right)\left(\frac{\mu}{\Phi c_t}\right)^{0.5} \dots\dots\dots\dots\dots\dots\dots\dots\dots\dots\dots\dots\dots\dots\dots\dots\dots\dots (3.34)$$

Where:

Δt = time where ½ slope occurs = 1.91e-12 hrs

$\Delta p'$ = Well-test-derivative value = 8.13e-3, psi

h =vertical thickness, ft = 0.028 ft

x_f = half-length, ft = ½ of x-dimension of sample = 0.025ft

μ = viscosity, cp = 0.2

c_t = rock compressibility, 1/psi = 3e-5

Φ = effective porosity of sample = 0.28

The permeability from the above calculation is equal to **1291 md**. This is quite close to the conventional permeability estimates. However, we note that as the half-slope (slope = .5) region was very brief [1.5 e-12 → 5 e-12] about half a log-cycle; it is possible that this value refers only to the part of the rock immediately adjacent to the critical sub-volume. However, it is also likely to just be a short-lived transient response building towards finite-volume effects.

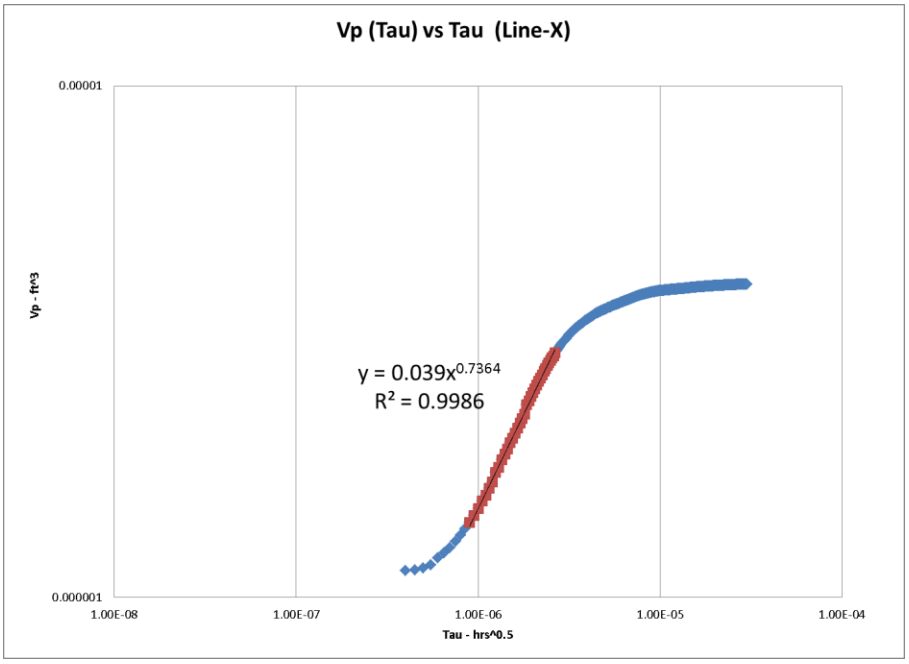

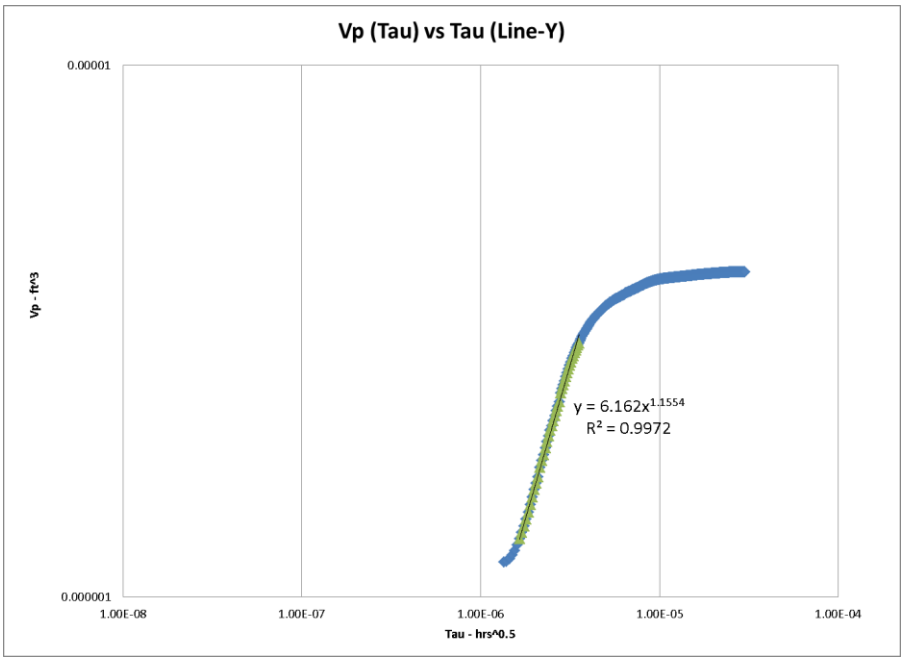

Figure 45 – Shows the log-log plots of V_p (τ) against τ for the sink-nodes in each direction. For the Line-Y case, the exponent is greater than and close to 1, indicating some sort of known geometry in the flow.

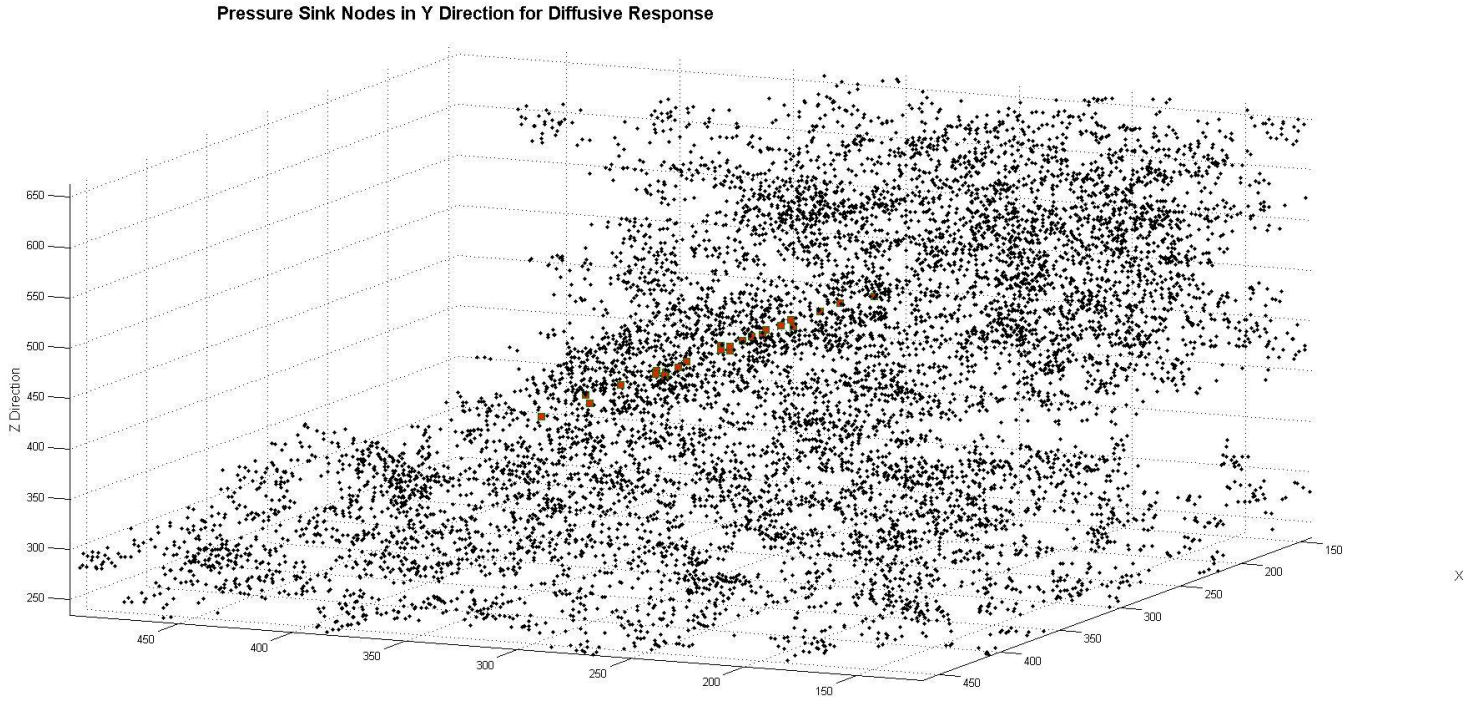

Figure 46 – Suggests that the nodes chosen for the Line-Y direction may indeed be in the plane of the critical sub-volume, from a different view. The red squares are the pressure-sink nodes and the black dots the drained nodes.

3.5.5 Further Analysis and Discussion: Point Node or Nodes along Planes

The same analysis is performed for a plane of sink-nodes in all three planes: YZ, XZ and XY (the inlet nodes for convective permeability calculations) perpendicular to the X, Y and Z directions. Since the number the seed-nodes will be high and covers a vast area, we expect to hit the critical sub-volume very quickly. The location of the seed nodes is shown in Figure 47.

The well-test derivatives for each direction are shown in Figure 48 . As expected all three of them are very similar. There is little or no "node-storage" effect, possibly because the nature of the skeletonization procedure in AVIZO produces nodes on the very edge of the data set with little volume. More importantly, we observe the same inflexion points in all three signatures as the critical volume is reached and distorts the geometry of flow accordingly. Again as a result of this unstructured-manner of flow, we fail to evolve any reasonable exponent from the transient period. Figure 49 superposes all three responses on the same plot, and shows that once the critical sub-volume is reached, the response is identical.

Figure 50 shows the log-log plots of $V_p(\tau)$ against τ for the diffusive floods in each direction. The exponent evolved is again does not suggest a familiar geometry, and is in fact less than 1. However that all the three exponents are nearly identical suggests that the overall geometry of the flow from rock to sub-volume, and from sub-volume to the plane is identical to all three planes. The exponent is more sensitive to the orientation of

a line of nodes inside the rock as opposed to an adjacent face. Appendixes A, B, C contain the drainage volumes visualization for seed nodes on each plane.

The motivation for attempting just a single point node as a sink node to evaluate the pressure-derivative response is as follows. Probe permeameters use a point to inject fluid into the media, and approximate all transient (non-uniform) flow-geometry as hemi-spherical to obtain the estimate (Manrique et al. 1994). A sink node was placed in the middle of the core and the well-test derivative for flow into this node was calculated. This is shown in Figure 51. The response is very similar to that obtained for the sink nodes on a line, as expected. We observe that no -0.5 exponent is evolved which would indicate spherical flow. This is confirmed in Figure 52, which shows a plot of $V_p(\tau)$ against τ and does not show an exponent close to 3. The permeability calculated by assuming a hemispherical permeability is shown in Figure 53. Before the high-connectivity volume is reached, the permeability is estimated to be approximately **500 – 1000 md**. The calculations employed are described below:

$$m_{pp} = 2\sqrt{\Delta t}\Delta p' \ldots\ldots\ldots\ldots\ldots\ldots\ldots\ldots\ldots\ldots\ldots\ldots\ldots\ldots\ldots\ldots\ldots\ldots\ldots\ldots\ldots\ldots\ldots\ldots\ldots\ldots\ldots\ldots.(3.35)$$

$$k_{spherical} = \left(\left(\frac{2453 * 0.234 * qB\mu}{m_{pp}}\right)(\phi\mu c_t)^{0.5}\right)^{2/3} \ldots\ldots\ldots\ldots\ldots\ldots\ldots\ldots\ldots\ldots\ldots\ldots\ldots(3.36)$$

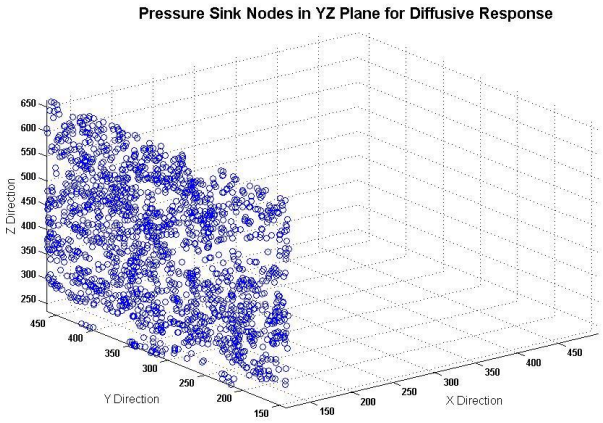

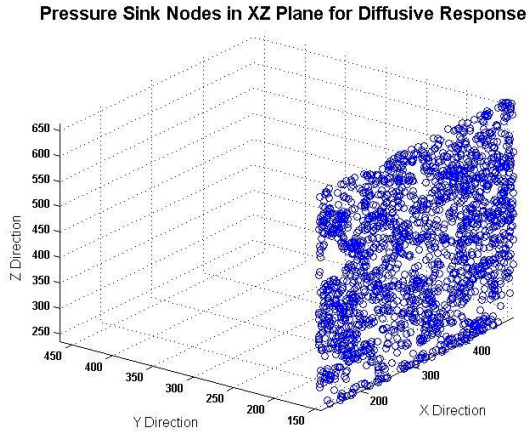

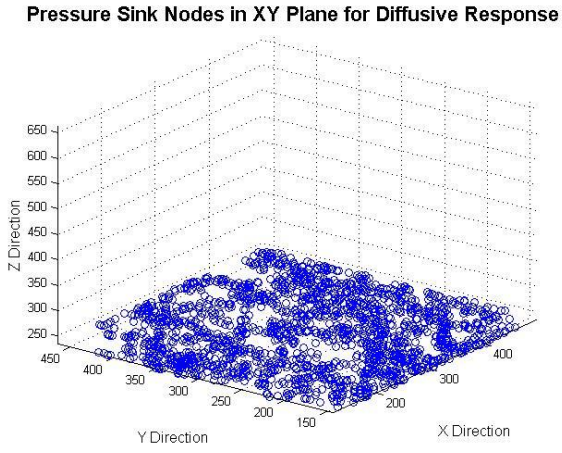

Figure 47 – Shows the pressure-sink nodes for the diffusive flood in each direction.

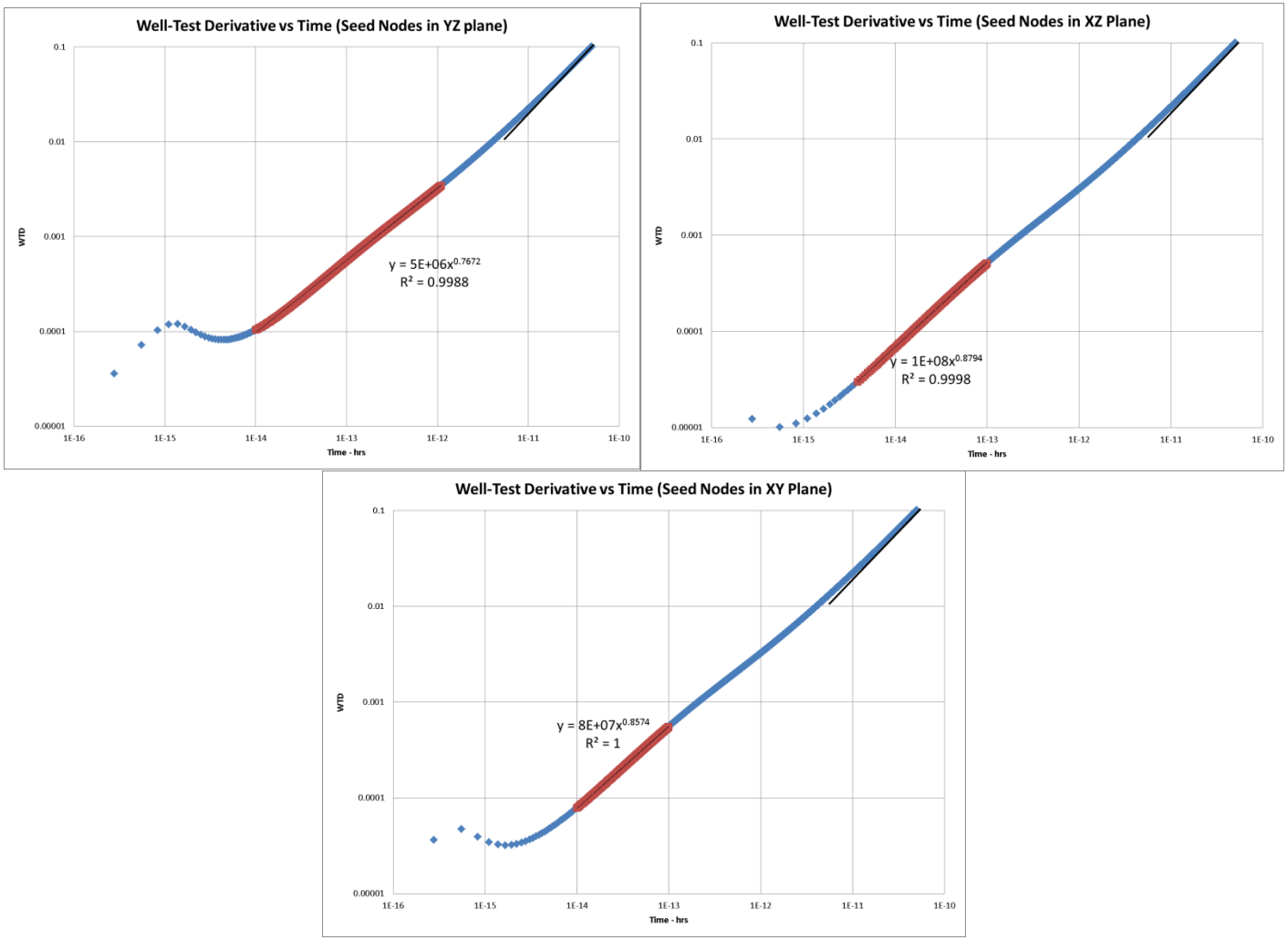

Figure 48 – Shows how the well-test derivative signature obtained for seed-nodes in all three planes is very similar.

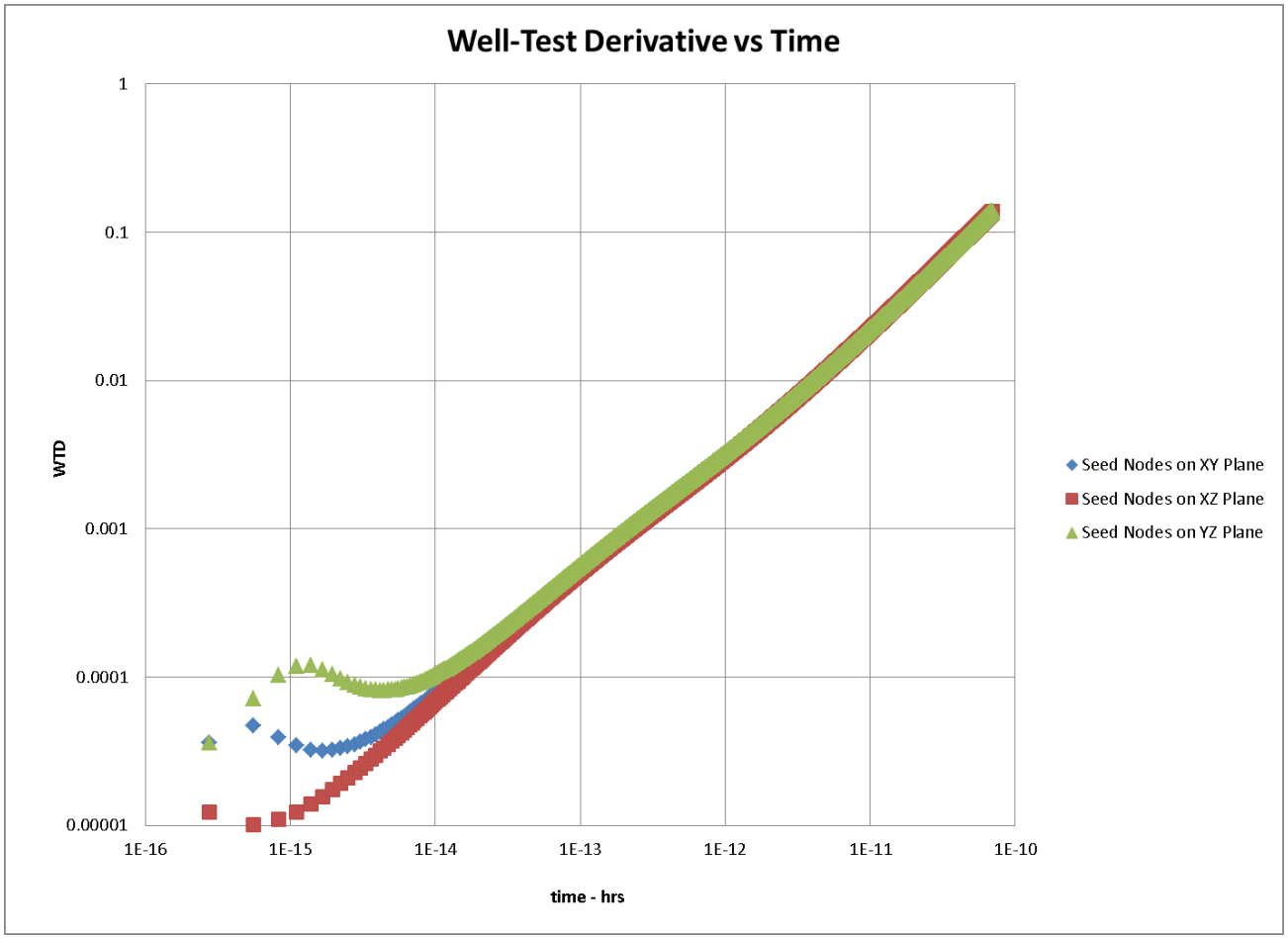

Figure 49 – Shows the pressure derivative response from nodes on each plane on the same plot. Once the critical sub-volume is reached, all the responses become identical.

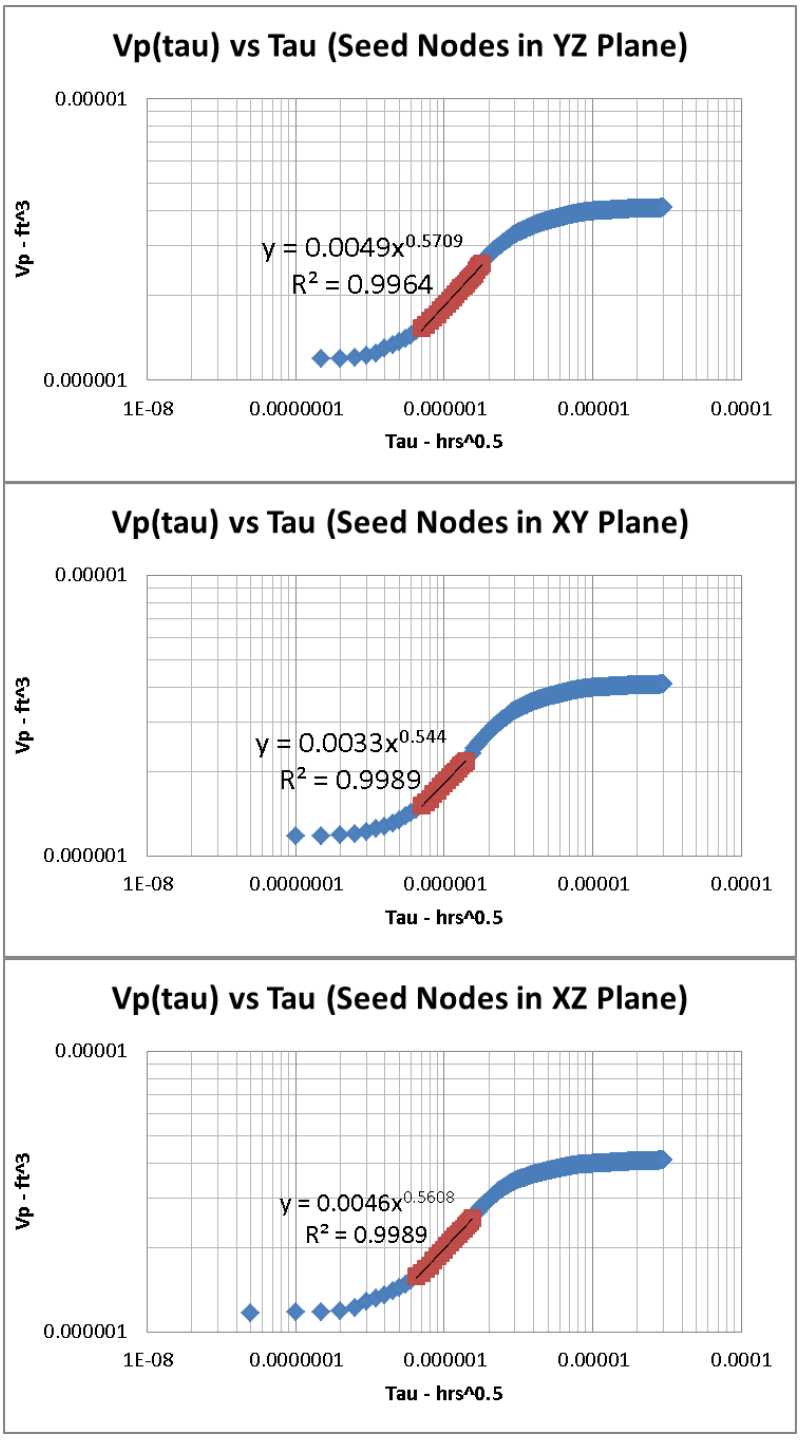

Figure 50 – Shows the log-log plots of V_p (τ) against τ for the seed-nodes in each plane. The same exponent is evolved for each case, suggesting that the overall pattern of flow in each case is similar.

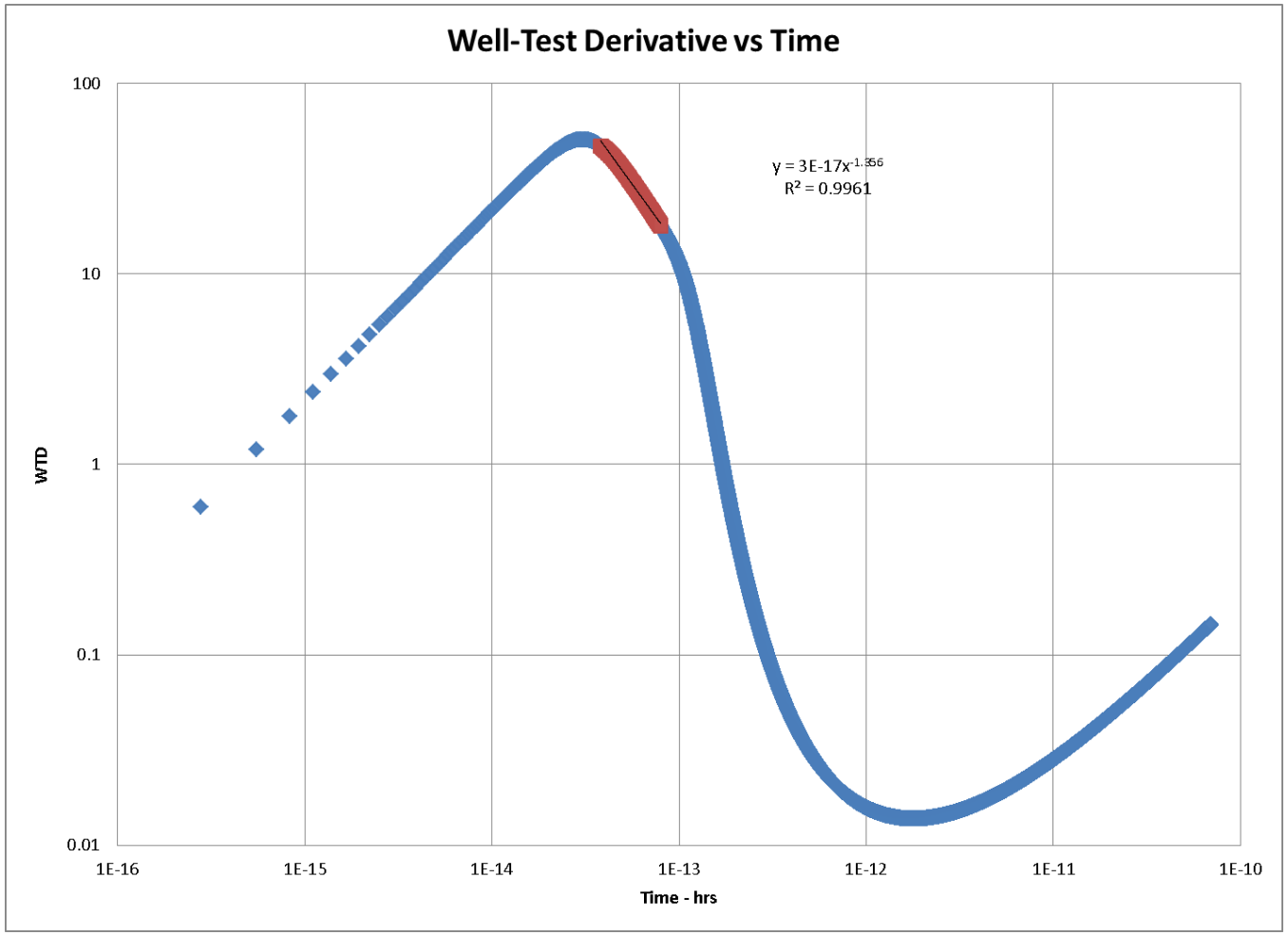

Figure 51 – Shows the pressure-derivative response for a point sink node. We fail to observe an exponent that suggests spherical-flow Overall, the behavior observed is again similar to that for a line of nodes.

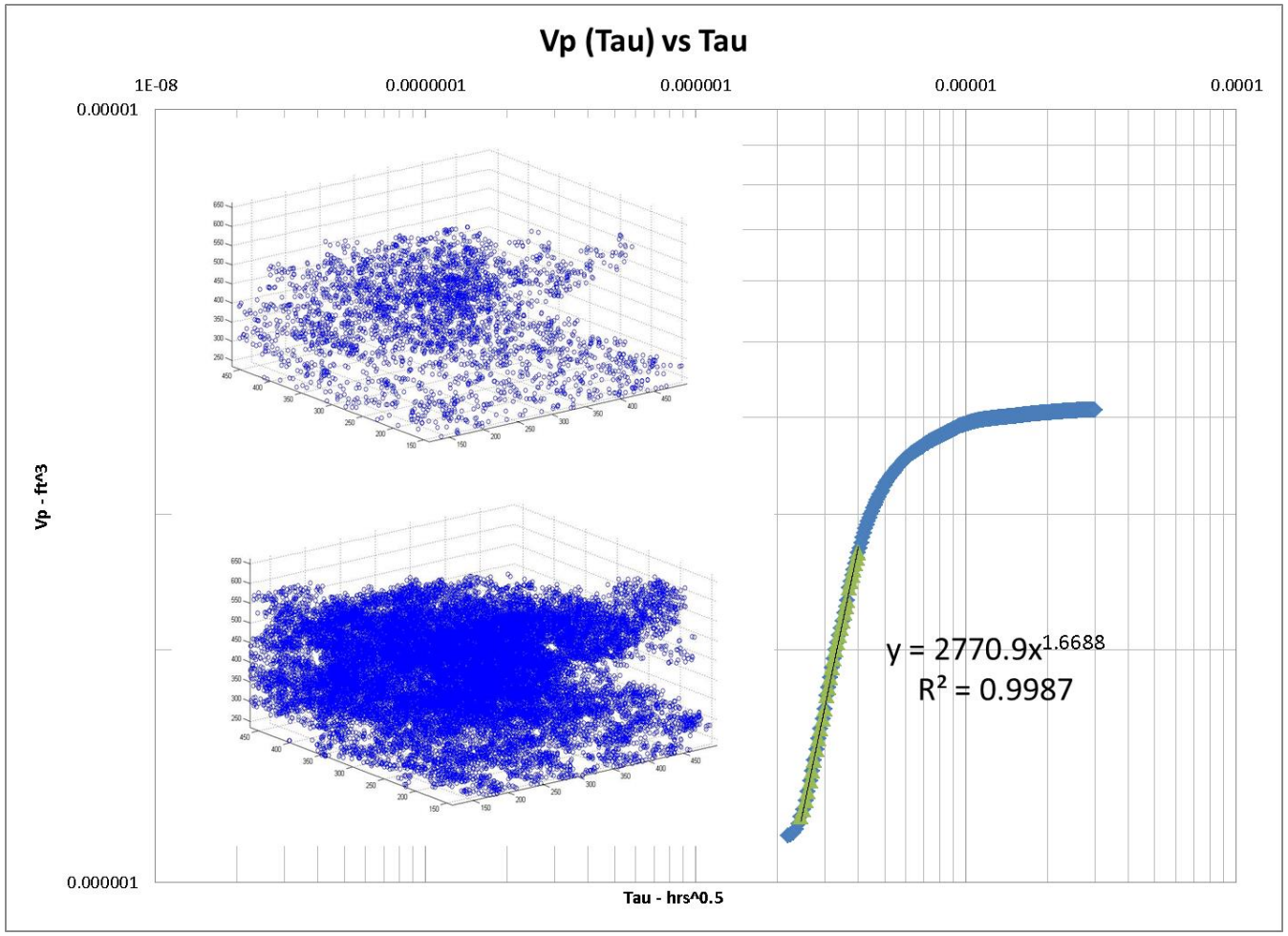

Figure 52 – Shows how a power-law fit to the Vp (τ) vs τ plot fails to evolve an exponent suggesting any known geometry. The visualization of nodes in Vp (τ) for the range of τ fit to the power-law again highlights the critical sub-volume.

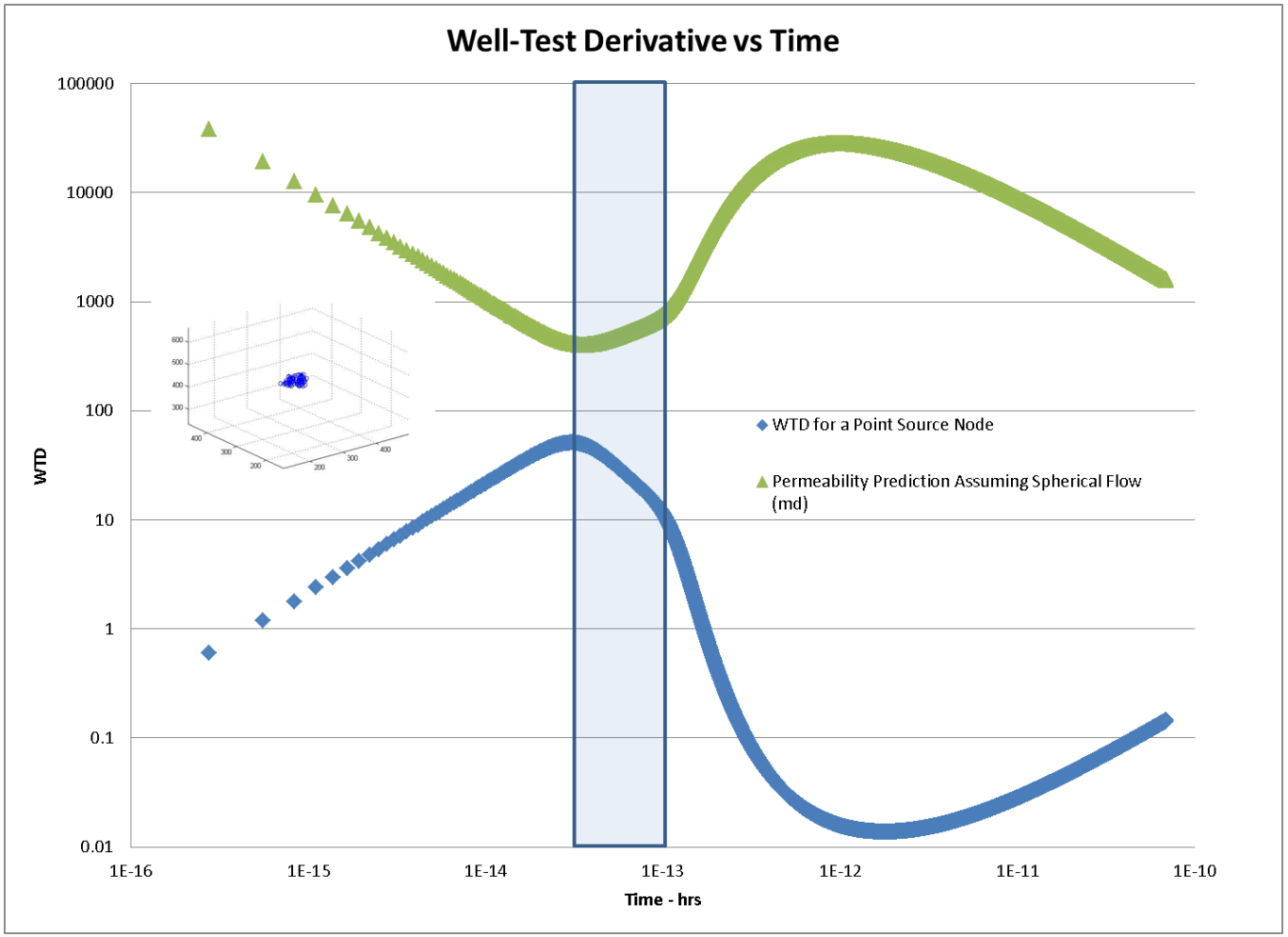

Figure 53 – Shows the permeability evaluated at each time, assuming spherical flow. Between the time after node-storage effects and the critical sub-volume is reached, the permeability appears to be around 0.5 – 1 Darcy. The nodes accounting for this calculation are shown.

3.6 Dual Porosity Interpretation

The signature of the well-test derivative obtained for a set of sink-nodes along a line in all three directions is also very suggestive of a secondary pore-volume feeding into a primary pore-volume, in a dual porosity flow. A dual porosity system is characterized by the storativity, ω, and the dimensionless inter-porosity transfer parameter, λ:

$$\omega = \frac{\Phi_{primary} c_{primary}}{\Phi_{primary} c_{primary} + \Phi_{secondary} c_{secondary}} \quad \ldots\ldots (3.37)$$

$$\lambda = \alpha * \frac{k_{secondary}}{k_{total\ system}} * r_w^2 \quad \ldots\ldots (3.38)$$

Here α is a parameter proportional to the contact area between the primary and secondary pore-volumes.

The storativity relates to the pore-volume ratios between primary and the whole system and controls how steeply the well-test derivative declines, while the transfer parameter relates to how quickly the fluid transfers between the primary and secondary pore-volumes, and dictates the timing of the inflexion points of the well-test derivative. (Warren and Root 1963). This is illustrated in Figure 54, which shows a (dimensionless) log-log plot of the well-test derivative with time for varying values of ω and λ.

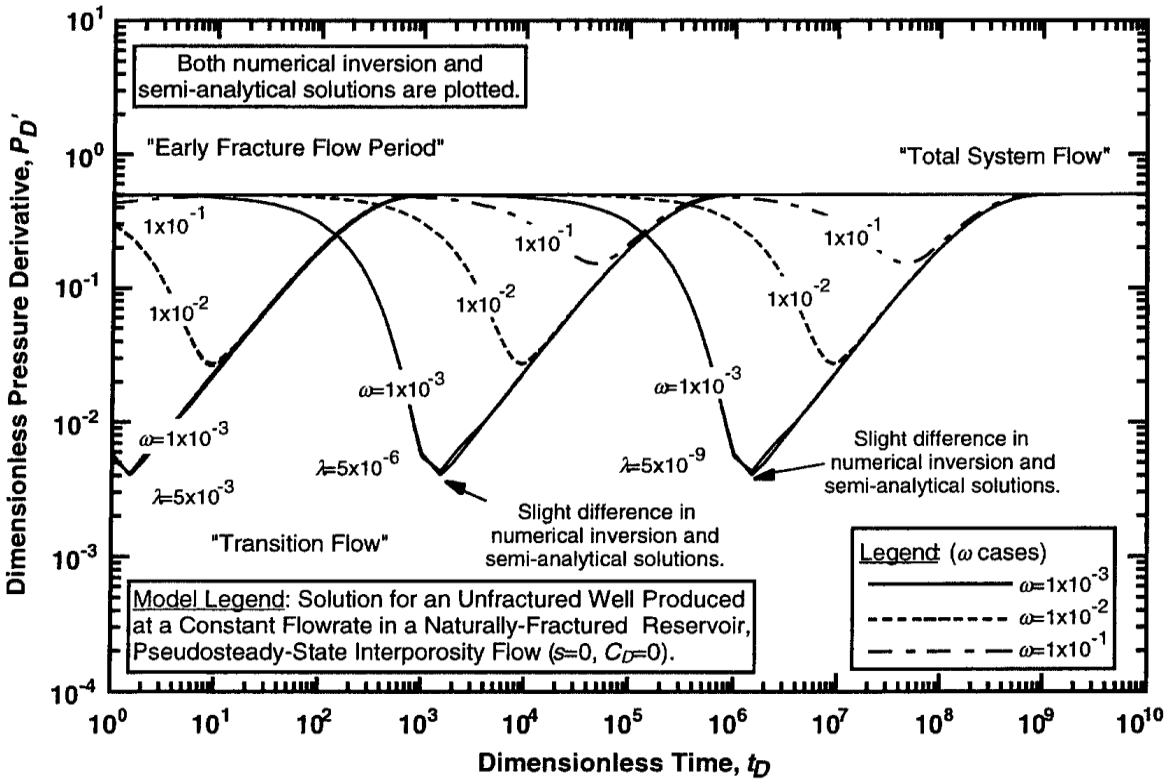

Figure 54 – Shows how ω relates to how steeply the well-test derivative declines and λ relates to how soon the secondary pore-volume is reached or drained. (Warren and Root 1963)

From left to right, the typical PSS inter-porosity dual porosity signature reads as: drainage from the primary pore-volumes only (horizontal line) → the secondary pore-volume begins to drain into the primary (curvature) → the whole system drains as a unit (horizontal line). In the case of our sample, the finite size effects are obtained very quickly, so the second horizontal line is masked by PSS flow, which shows up as a unit slope. Secondly, as Figure 38 to Figure 40 show, the drainage from the secondary pore-volumes also occurs very quickly (showing up in the drop in the derivative response)

and is the dominant flow characteristic; resulting in a masking of the first horizontal line as well. A qualitative comparison in Figure 44 shows that the rate of decline of the well-test derivative, upon the onset of drainage from the secondary pore-volumes, is very steep, and confirms that majority of the fluid is contained in the secondary porosity. I.e. the storativity is very low. The masking of the horizontal lines however, poses an unsurmountable challenge to a quantitative estimate of ω and λ via type-curves. A physical match to a (Stewart and Asharsobbi 1988) type curve however, was still attempted by calculating the level of the derivative, assuming that the "total system permeability" was equal to the **average convective permeability estimate, of 1423 md.** This effectively gives us the vertical match point, the curve is slid horizontally until a suitable match is obtained. This value is obtained by re-arranging the following equation for permeability from an infinite-acting region:

$$k = \frac{70.6qB\mu}{m'h} \ldots\ldots\ldots\ldots\ldots\ldots\ldots\ldots\ldots\ldots\ldots\ldots\ldots\ldots\ldots\ldots\ldots\ldots\ldots\ldots\ldots\ldots\ldots\ldots\ldots\ldots\ldots\ldots\ldots\ldots. (3.39)$$

Where,

m' = level of derivative

h = length of line of nodes, ft

The level of derivative for the set of sink nodes in each direction is shown below:

Level of Derivative	value
m'(x)=	0.09
m'(y)=	0.11
m'(z)=	0.08

Table 3 – Shows the level of the derivative calculated for the well-test responses for a line of sink-nodes in each direction, assuming the permeability to be 1423 md.

ω is read off from the type-curve match, while λ is calculated from a match point, using the equation below.

$$\lambda = \frac{4}{\left(0.0002637 \frac{k}{\phi \mu c_t r_w^2} \frac{[t]_{MP}}{\left[\frac{t_D \lambda}{4}\right]_{MP}}\right)} \ldots\ldots\ldots\ldots\ldots\ldots\ldots\ldots\ldots\ldots\ldots\ldots\ldots\ldots\ldots\ldots\ldots\ldots\ldots\ldots. (3.40)$$

Where,

k = average convective permeability = 1423 md

ϕ = effective porosity = 0.278

r_w = tolerance used in finding the sink nodes on an imaginary line = 2.47E-4, 2.11E-4, 2.81E-4 ft for X, Y and Z directions respectively.

$[\quad]_{MP}$ = values of x-axis match point on either type curve or the plotted data.

Unfortunately, the extreme small-size of our sample means that PSS begins to feature very early so that there is no clear “total-system flow”. This means that finite-size effects of the sample begin to mask the slope soon after the second inflexion point. In light of

the above, two means have been employed to obtain a match to the type-curves. First, is by sliding horizontally till the steepness of the descent and the location of the second inflexion point are aligned. The second method involves matching all three curves to approximately the same value of storativity ratio ω, the reasoning being that the rate of decline of the derivative, or the steepness, is the same for all three curves, as shown by Figure 44.

For the first method of matching to the type curves, the results obtained for λ and ω, along with the average are shown in Table 4 and Table 5 below. **The average value of ω is 1.17e-3 and the average value of λ is 3.12e-2.** Figure 55 to Figure 57 show the matches obtained for the line of nodes in each direction, using this method.

For the second method, **ω was fixed at a value of 1e-3.** Figure 58 to Figure 60 shows the matches to the type curve obtained using this method. Table 6 and Table 7 show the values obtained for λ and ω, for the line of nodes in each direction. **The average value of λ is 4.71e-2.** However, there is much higher variability in this estimate than in the first approach.

The relatively high value of the inter-porosity transfer co-efficient suggests that the fluid transfer between the secondary and primary pore-volumes is very effective. The small value of the storativity ratio means that most of the pore-volume is located within the secondary porosity. This is also consistent with our assessment upon visualizing drainage volumes.

ω may also be estimated as a ratio of the pore-volume drained up to when the depth of investigation reaches the high-connectivity sub-volume – primary drained pore-volumes – and the whole pore-volume. This primary drainage volume can be calculated either by evaluating the volume drained up to a time chosen just beyond the first inflexion point as inter-porosity flow fully develops, or at the value of τ when the highly-connected sub-volume is reached. Table 2 highlights this value of τ for the line of nodes in the Z direction. The times, t, and τ chosen for the set of line-nodes in each direction and their corresponding values obtained for ω are shown in Table 9. The values calculated were found to corroborate well with the values obtained from the type curves.

Estimate of λ	Value
Line of Nodes in X Direction	5.99E-02
Line of Nodes in Y Direction	5.56E-03
Line of Nodes in Z Direction	2.82E-02
Average	**3.12E-02**

Table 4 – Shows the estimate of λ obtained for the well-test response in each direction, with the first method of matching to the type-curve.

Estimate of ω	Value
Line of Nodes in X Direction	5.00E-04
Line of Nodes in Y Direction	1.50E-03
Line of Nodes in Z Direction	1.50E-03
Average	**1.17E-03**

Table 5 – Shows the estimate of ω obtained for the well-test response in each direction, with the first method of matching to the type-curve.

Estimate of λ	Value
Line of Nodes in X Direction	1.09E-01
Line of Nodes in Y Direction	3.97E-03
Line of Nodes in Z Direction	2.82E-02
Average	**4.71E-02**

Table 6 – Shows the estimate of λ obtained for the well-test response in each direction, with the second method of matching to the type-curve.

Estimate of ω	Value
Line of Nodes in X Direction	1.00E-03
Line of Nodes in Y Direction	1.00E-03
Line of Nodes in Z Direction	1.00E-03
Average	**1.00E-03**

Table 7 – Shows the estimate of ω that was fixed for the second method of matching to the type-curve.

Direction of Sink Nodes	tau-chosen (√hrs) to evaluate Vp(Primary)	time-chosen (hrs) to evaluate Vp(primary)
X	3.50E-07	5.00E-15
Y	1.30E-06	6.80E-14
Z	6.50E-07	1.70E-14

Table 8 – Shows the values of τ and time, t, chosen to evaluate the primary drained volume, V_p (primary).

Direction of Sink Nodes	Numerical ω (ratios of Vp(τ))	Numerical ω (ratios of Vp(t))	Type-curve ω
X	6.00E-04	8.04E-04	5.00E-04
Y	8.29E-03	1.40E-03	1.50E-03
Z	3.05E-03	1.34E-03	1.50E-03
Average	**3.98E-03**	**1.18E-03**	**1.17E-03**

Table 9 – Shows that the values of ω calculated numerically corroborate those found from a match to the type-curves using the first method.

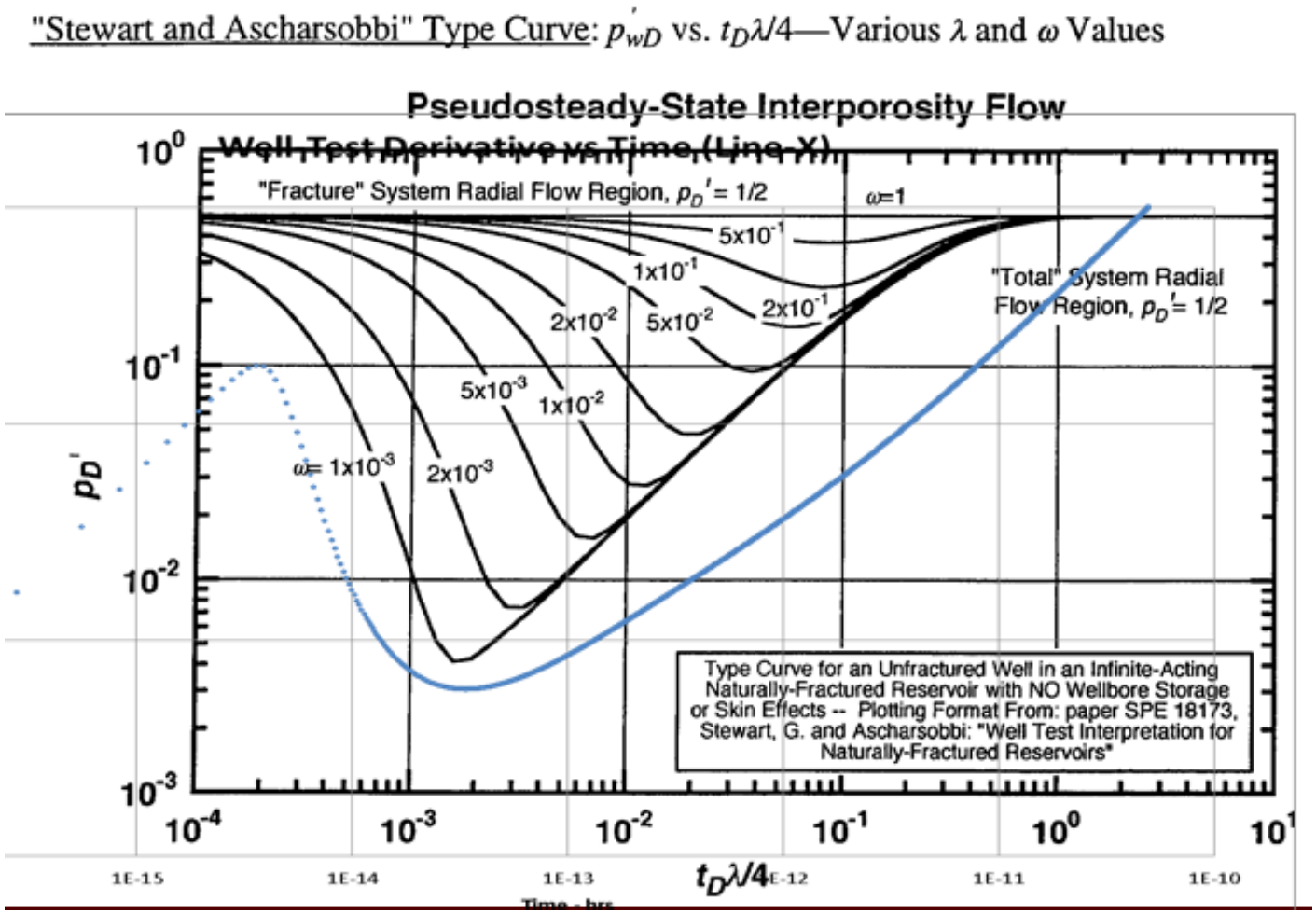

Figure 55 – Shows the type-curve match of the pressure derivative response for a line of nodes in X direction, using the first method. ω is approximately 5e-4.

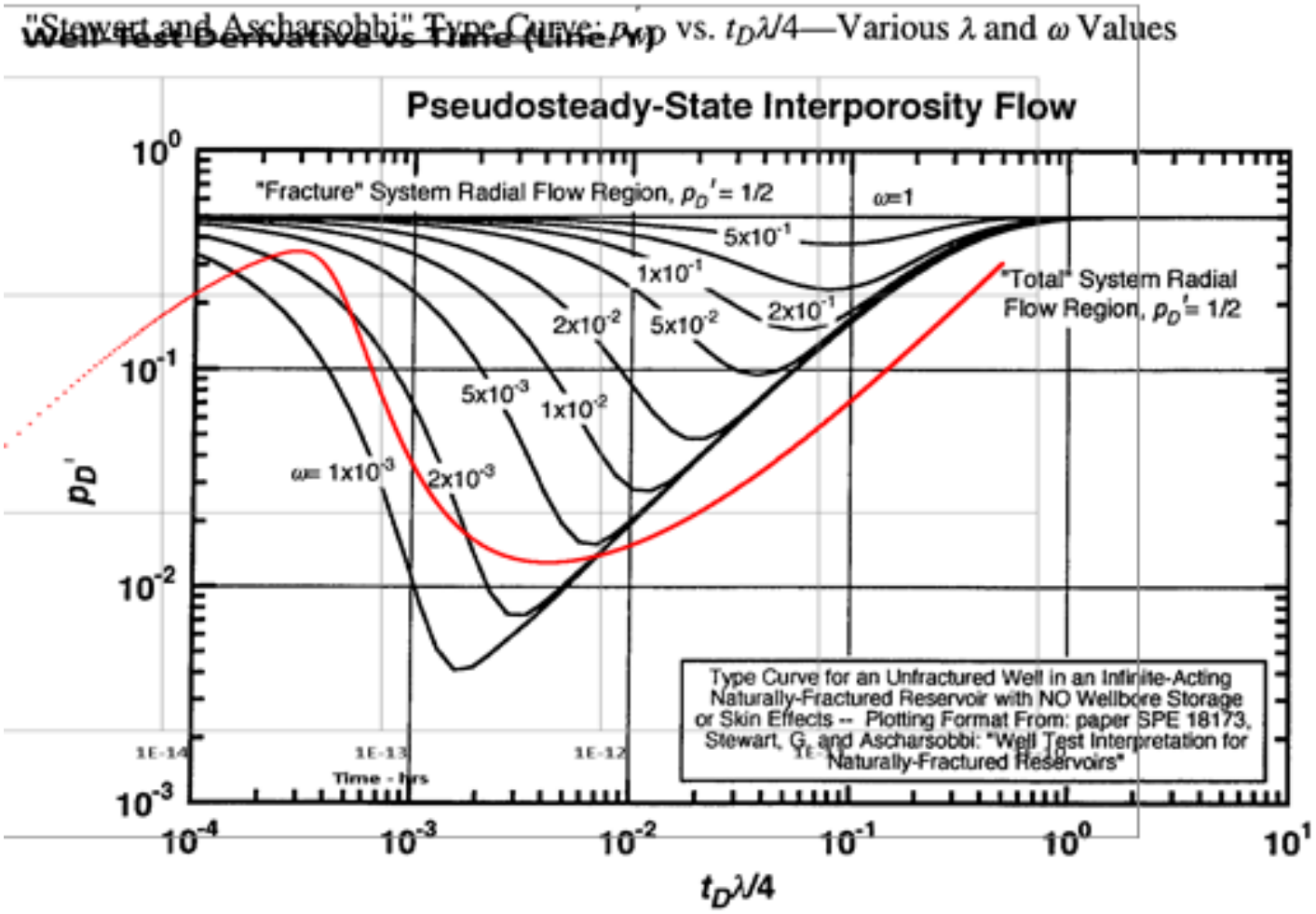

Figure 56 – Shows the type-curve match of the pressure derivative response for a line of nodes in Y direction, using the first method. ω is approximately 1.5e-3.

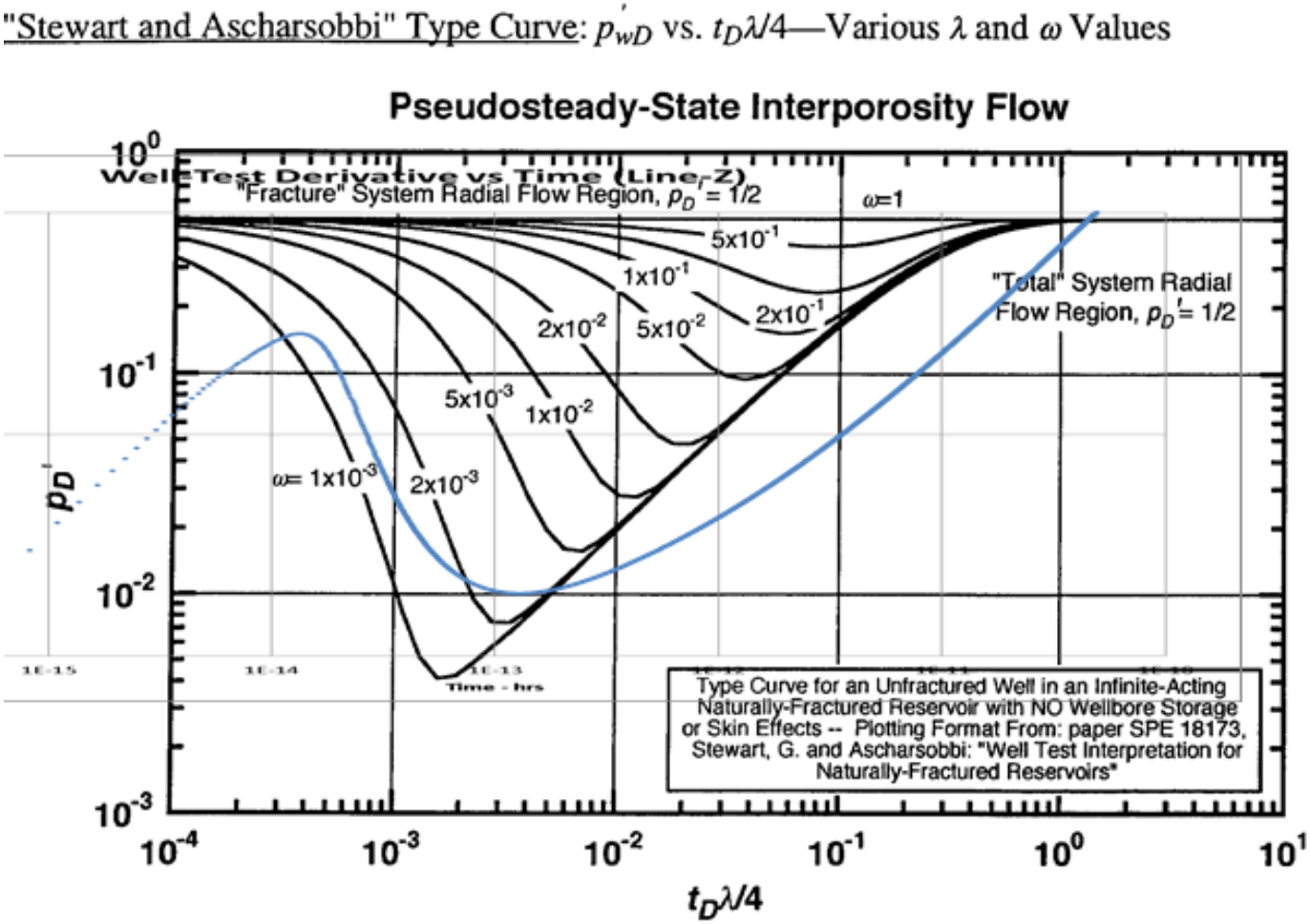

Figure 57 – Shows the type-curve match of the pressure derivative response for a line of nodes in Z direction, using the first method. ω is approximately 1.5e-3.

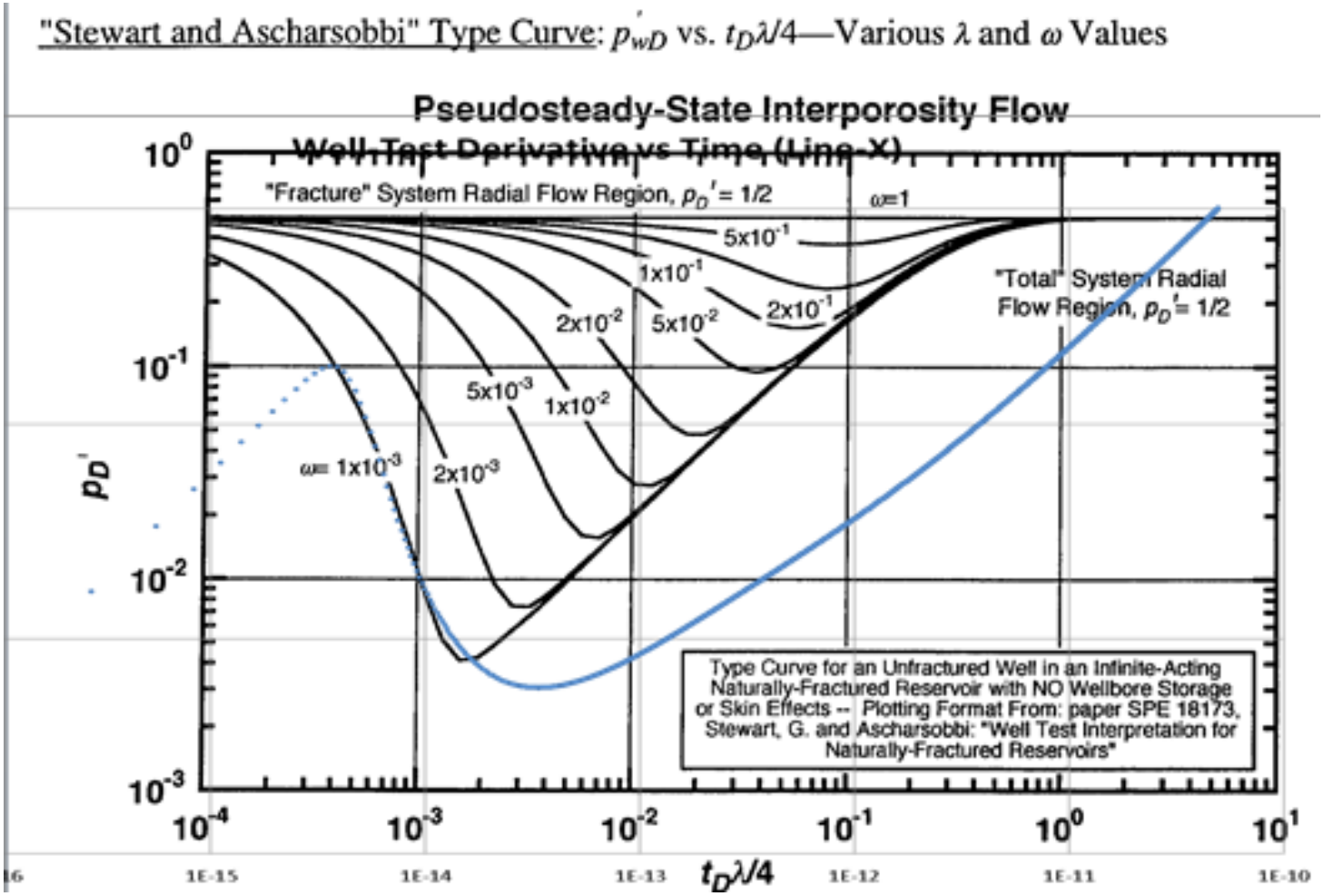

Figure 58 – Shows the type-curve match of the pressure derivative response for a line of nodes in X direction, using the second method. ω is 1e-3.

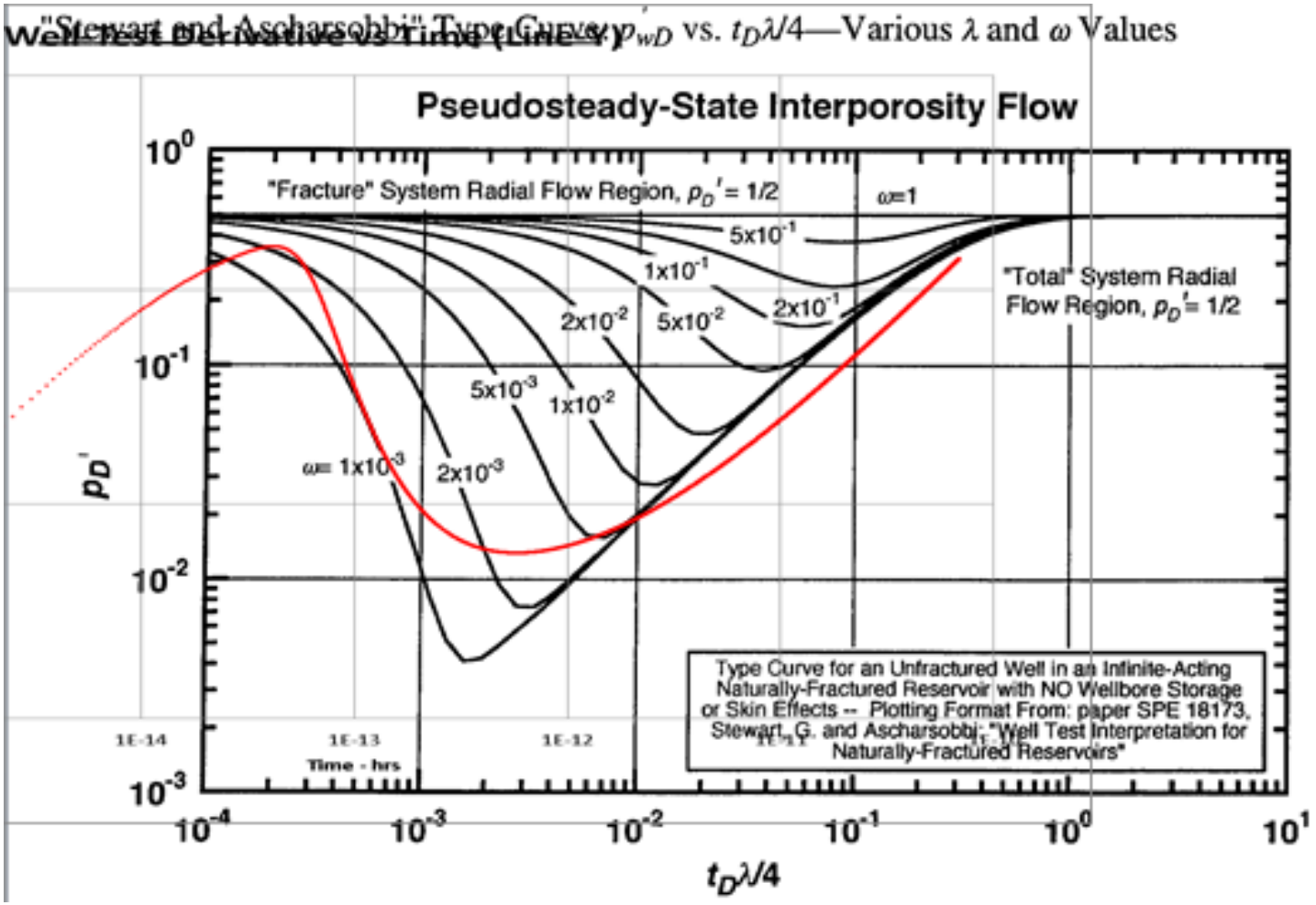

Figure 59 – Shows the type-curve match of the pressure derivative response for a line of nodes in Y direction, using the second method. ω is 1e-3.

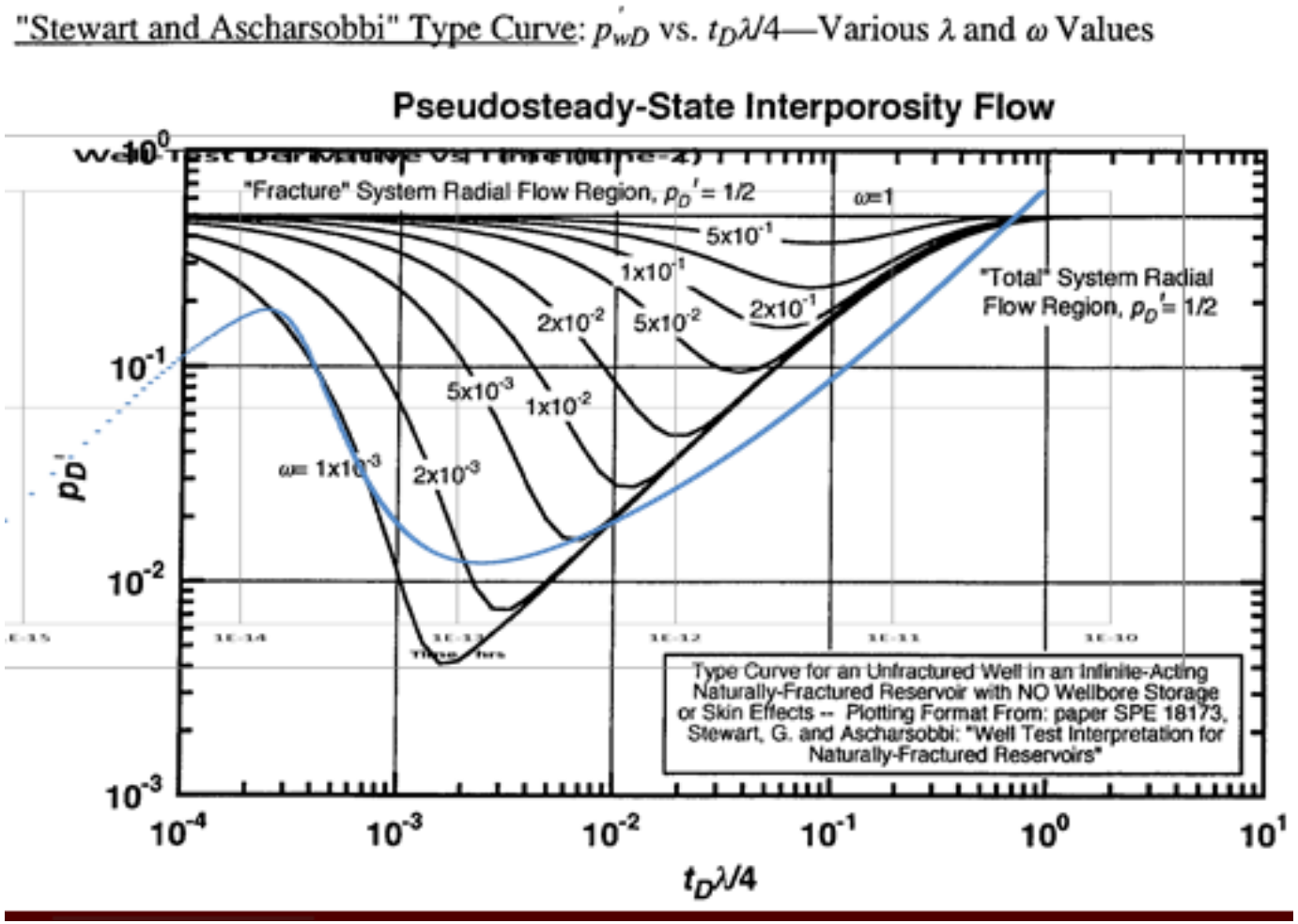

Figure 60 – Shows the type-curve match of the pressure derivative response for a line of nodes in Z direction, using the second method. ω is 1e-3.

.

3.7 Summary and Conclusions

The observations obtained from the analysis done on the μ-CT scan data are summarized below.

1. An unstructured, lattice representation of a carbonate sample has been illustrated as applicable and being very useful in studying the flow characteristics in this type of rock.

2. The statistics extracted after skeletonization into nodes and bonds indicate that even within a sample of the carbonate rock only a few millimeters in dimension, there is considerable heterogeneity, and possibly even bimodality.

3. A lattice-system has been shown to be a useful means to represent the rock when there is a broad distribution in bond lengths, radii and co-ordination numbers of nodes.

4. The effective porosity of the rock is 27.8%.

5. Permeability was determined from a *digital* coreflood to be an **average of 1423md**. The permeabilities value for each direction is found as:

Direction	Permeability, md
x	**1367**
y	**1682**
z	**1219**

Table 1 – Shows the permeability obtained from a convective core-flood in each direction.

6. A study of the diffusive process in the rock using an unstructured lattice was very illuminating, and well-suited to the highly un-geometric flow occurring in the rock.

7. Flow in the rock occurs primarily through a high-connectivity sub-volume that lacks a well-defined geometry. Log-log plots of the transient-response produce a dual-porosity signature, and fail to provide known (geometric) exponents.

8. However, where the pressure-sink nodes are seemingly aligned with the sub-volume, the system briefly exhibits fracture-linear behavior. The permeability thus extracted is equal to **1291 md**, which is comparable to the estimate obtained from the core-flood.

9. Permeability of a small portion of the rock, (before the sub-volume was reached) assuming spherical flow to a point sink node was calculated to be between **500 to 1000 md.**

10. The dual-porosity analysis via type-curves reveals that **the ω is around 1e-3 and the value of λ ranges from 3e-2 to 5e-2**. That even a millimeter-dimension sample of the carbonate rock should exhibit dual-porosity behavior demonstrates the complex pore-space types highlighted in Figure 8.

11. The reservoir consists of the matrix blocks, vugs and fractures identified in Figure 7, in what was thought to be a triple-porosity system. However, as the μ-CT sample analysis shows, the **matrix itself exhibits dual-porosity behavior**.

CHAPTER IV

SUMMARY AND RECOMMENDATIONS FOR FUTURE WORK

4.1 Summary and Conclusions

The unique nature of heterogeneous connectivity in carbonate rocks has been highlighted, and consequently an unstructured lattice representation consisting of a network of nodes and bonds, has been motivated as being a more natural than a grid-based system. A comparison between calculations for convective and diffusive properties on grid and their equivalents on a lattice was performed and provided comparable results. Additionally, a μ-CT scan data of a carbonate rock from an outcrop was then digitally reduced to an unstructured lattice of nodes and bonds. Convective and diffusive flow calculations were then subsequently performed with the goal of extracting permeability and other transport properties. Permeability from a digital core-flood was determined in all three directions. The diffusive process and a visualization of drainage volume propagation in the rock however, while proving inconclusive in evolving a value of infinite-acting radial flow permeability, were very useful in illustrating the highly un-geometric nature of fluid flow in the rock, and as a consequence, the suitability of the lattice and unstructured representation.

4.2 Recommendations for Future Work

This work was designed to be a preliminary study that evaluated the applicability of an unstructured representation and also to provide the groundwork for other graduate students to build upon. The ultimate goal is to be able to characterize a carbonate reservoir via multiple lattices of nodes superposed onto each other to honor both the geologic features and their un-structuredness of connectivity. The following suggest some additional future work:

1. With the diffusive time-of-flight populated on the lattice, calculate the pressure response. This and the derivative information together may be useful to fit a dual porosity model in ECRIN.

2. The network statistics extracted from the matrix portion of the carbonate rock should be used to create an upscaled representation of the matrix rock at a larger length-scale.

3. If carbonate reservoir field data is available, an attempt to model the reservoir using an exclusively lattice approach followed by a comparison of history-matches to production data with grid-based models will be definitive in exploring the utility and fully illustrating the unstructured approach.

4. The workflow shown in this thesis may also be applied to shale core samples to study their flow behavior.

REFERENCES

Ahr, W.M. 2008. *Geology of Carbonate Reservoirs: The Identification, Description and Characterization of Hydrocarbon Reservoirs in Carbonate Rocks*: Wiley. Original edition. ISBN 9780470369258.

Al-Kharusi, A.S. and Blunt, M.J. 2008. Multiphase Flow Predictions from Carbonate Pore Space Images Using Extracted Network Models. *Water Resources Research* **44** (6): W06S01. DOI: 10.1029/2006wr005695

Bakke, S. and Øren, P.-E. 1997. 3-D Pore-Scale Modelling of Sandstones and Flow Simulations in the Pore Networks. *SPE Journal* **2** (02): 136-149. DOI: 10.2118/35479-pa

Berg, R.R. 1970. Method for Determining Permeability from Reservoir Rock Properties. *Trans. Gulf Coast Assoc. Geol. Soc.* **20**: 303-317.

Biswal, B., Øren, P.-E., Held, R.J. et al. 2009. Modeling of Multiscale Porous Media. *Image Analysis and Stereology* **28**: 23-34.

Choquette, P.W. and Pray, L.C. 1970. Geologic Nomenclature and Classification of Porosity in Sedimentary Carbonates. *AAPG Bulletin* **54** (2): 207-244.

Datta-Gupta, A. 2013. Fast Marching Method: A New Paradigm for Modeling Unconventional Reservoirs. In *CHBE Seminar Series*: Rice University.

Datta-Gupta, A. and King, M.J. 2007. *Streamline Simulation : Theory and Practice*. Spe Textbook Series; 11; . Richardson: Tex. Society of Petroleum Engineers. Original edition. ISBN 9781555631116; 1555631118.

Dijkstra, E.W. 1959. A Note on Two Problems in Connexion with Graphs. *Numerische Mathematik* **1**: 269--271.

Goode, D.J. 1990. Particle Velocity Interpolation in Block-Centered Finite Difference Groundwater Flow Models. *Water Resources Research* **26** (5): 925-940. DOI: 10.1029/WR026i005p00925

Gupta, A. and Poppelreiter, M. 2010. Innovative Field Camp for Education and Industry-Academic Collaboration in Geology-Based Reservoir Model Building for Carbonate Reservoirs in the Middle East. Paper presented at the SPE Annual Technical Conference and Exhibition, Florence, Italy. Society of Petroleum Engineers. DOI: 10.2118/134453-ms.

Gurpinar, O., Kalbus, J., and List, D. 1999. Numerical Modeling of a Triple Porosity Reservoir. Paper presented at the SPE Asia Pacific Improved Oil Recovery Conference, Kuala Lumpur, Malaysia. Society of Petroleum Engineers. DOI: 10.2118/57277-ms.

Iwere, F.O., Apaydin, O.G., Moreno, J.E. et al. 2004. The Challenges of Numerical Simulation of a Complex Fractured Carbonate Reservoir with Available Disparate Data Sets. Paper presented at the SPE International Petroleum Conference in Mexico, Puebla Pue., Mexico Society of Petroleum Engineers. DOI: 10.2118/91691-ms.

Jiang, Z., Dijke, M.I.J., Wu, K. et al. 2012. Stochastic Pore Network Generation from 3d Rock Images. *Transport in Porous Media* **94** (2): 571-593. DOI: 10.1007/s11242-011-9792-z

Kulkarni, K.N., Datta-Gupta, A., and Vasco, D.W. 2000. A Streamline Approach for Integrating Transient Pressure Data into High Resolution Reservoir Models. Paper presented at the SPE European Petroleum Conference, Paris, France. Society of Petroleum Engineers. DOI: 10.2118/65120-ms.

Lee, J. 1982. *Well Testing*. Spe Textbook Series. Richardson, TX: Society of Petroleum Engineers. Original edition. ISBN 0895203170; 9780895203175 LCCN: 83-101508.

Longman, M. 1981. *Carbonate Diagenesis as a Control on Stratigraphic Traps : With Examples from the Williston Basin : Presented at the 1981 Aapg Fall Education Conference in Calgary, Canada* Original edition. ISBN 0-89181-170-2.

Lønøy, A. 2006. Making Sense of Carbonate Pore Systems. *AAPG Bulletin* **90** (9): 1381-1405. DOI: 10.1306/03130605104

Lucia, F.J. 1995. Rock-Fabric/Petrophysical Classification of Carbonate Pore Space for Reservoir Characterization. *AAPG Bulletin* **79** (9): 1275-1300.

Lucia, F.J., Kerans, C., and Jennings, J.W., Jr. 2003. Carbonate Reservoir Characterization. *Journal of Petroleum Technology* **55** (06): 70 - 72. DOI: 10.2118/82071-jpt

Manrique, J.F., Kasap, E., and Georgi, D.T. 1994. Geometric Factors for Probe Permeameter Measurements on Heterogeneous Rocks. Paper presented at the Permian Basin Oil and Gas Recovery Conference, Midland, Texas Society of Petroleum Engineers. DOI: 10.2118/27650-ms.

McIlreath, I.A. and Morrow, D.W. 1990. *Diagenesis*. Geoscience Canada Reprint Series. St John's, Nfld., Canada: Geological Association of Canada, Dept. of Earth Science, Memorial University of Newfoundland. Original edition. ISBN ISBN: 0919216404; 9780919216402; National Library: 900903775 LCCN: 91-199219.

Nairn, A.E.M. and Alsharhan, A.S. 2003. *Sedimentary Basins and Petroleum Geology of the Middle East*. Amsterdam: New York : Elsevier. Original edition. ISBN 0444824650; 9780444824653.

Narayanan, K. and Deans, H.A. 1988. A Flow Model Based on the Structure of Heterogeneous Porous Media. Paper presented at the SPE Annual Technical Conference and Exhibition, Houston, Texas. Society of Petroleum Engineers. DOI: 10.2118/18328-ms.

Palaz, I. and Marfurt, K.J. 1997. *Carbonate Seismology*. Geophysical Developments Series. Tulsa, OK: Society of Exploration Geophysicists. Original edition. ISBN 1560800380 (hc); 9781560800385 (hc); 9780931830419 (series); 0931830419 (series); 9781560802099 (electronic) LCCN: 96-38273.

Pollock, D.W. 1988. Semianalytical Computation of Path Lines for Finite-Difference Models. *Ground Water* **26** (6): 743-750. DOI: 10.1111/j.1745-6584.1988.tb00425.x

Ramakrishnan, T.S., Ramamoorthy, R., Fordham, E. et al. 2001. A Model-Based Interpretation Methodology for Evaluating Carbonate Reservoirs. Paper presented at the SPE Annual Technical Conference and Exhibition, New Orleans, Louisiana Society of Petroleum Engineers. DOI: 10.2118/71704-ms.

Schlumberger. 2007. Distribution of Oil from Carbonate Sources around the World. http://www.slb.com/services/technical_challenges/carbonates.aspx.

Sethian, J. 1999. Fast Marching Methods. *SIAM Review* **41** (2): 199-235. DOI: doi:10.1137/S0036144598347059

Stewart, G. and Asharsobbi, F. 1988. Well Test Intepretation for Naturally Fractured Reservoirs. Paper presented at the SPE Annual Technical Conference and Exhibition, Houston, Texas Society of Petroleum Engineers. DOI: 10.2118/18173-ms.

Vasco, D.W., Keers, H., and Karasaki, K. 2000. Estimation of Reservoir Properties Using Transient Pressure Data: An Asymptotic Approach. *Water Resources Research* **36** (12): 3447-3465. DOI: 10.1029/2000wr900179

Vaughan, R.L., Khan, S.A., Weber, L.J. et al. 2004. Integrated Characterization of Uae Outcrops: From Rocks to Fluid Flow Simulation. Paper presented at the Abu Dhabi International Conference and Exhibition, Abu Dhabi, United Arab Emirates Society of Petroleum Engineers. DOI: 10.2118/88730-ms.

Warren, J.E. and Root, P.J. 1963. The Behavior of Naturally Fractured Reservoirs. *Society of Petroleum Engineers Journal* **3** (03): 245-255. DOI: 10.2118/426-pa

Xie, J., Gupta, N., King, M.J. et al. 2012. Depth of Investigation and Depletion Behavior in Unconventional Reservoirs Using Fast Marching Methods. Paper presented at the SPE Europec/EAGE Annual Conference, Copenhagen, Denmark Society of Petroleum Engineers. DOI: 10.2118/154532-ms.

Zhang, Y., Yang, C., King, M.J. et al. 2013. Fast-Marching Methods for Complex Grids and Anisotropic Permeabilities: Application to Unconventional Reservoirs. Paper presented at the SPE Reservoir Simulation Symposium, The Woodlands, Texas, USA Society of Petroleum Engineers. DOI: 10.2118/163637-ms.

Zhou, Y. 2013. Improved Upscaling & Well Placement Strategies for Tight Gas Reservoir Simulation and Management; Doctoral dissertation, Texas A & M University.

APPENDIX A

DRAINAGE VOLUMES FOR SEED NODES ON YZ PLANE

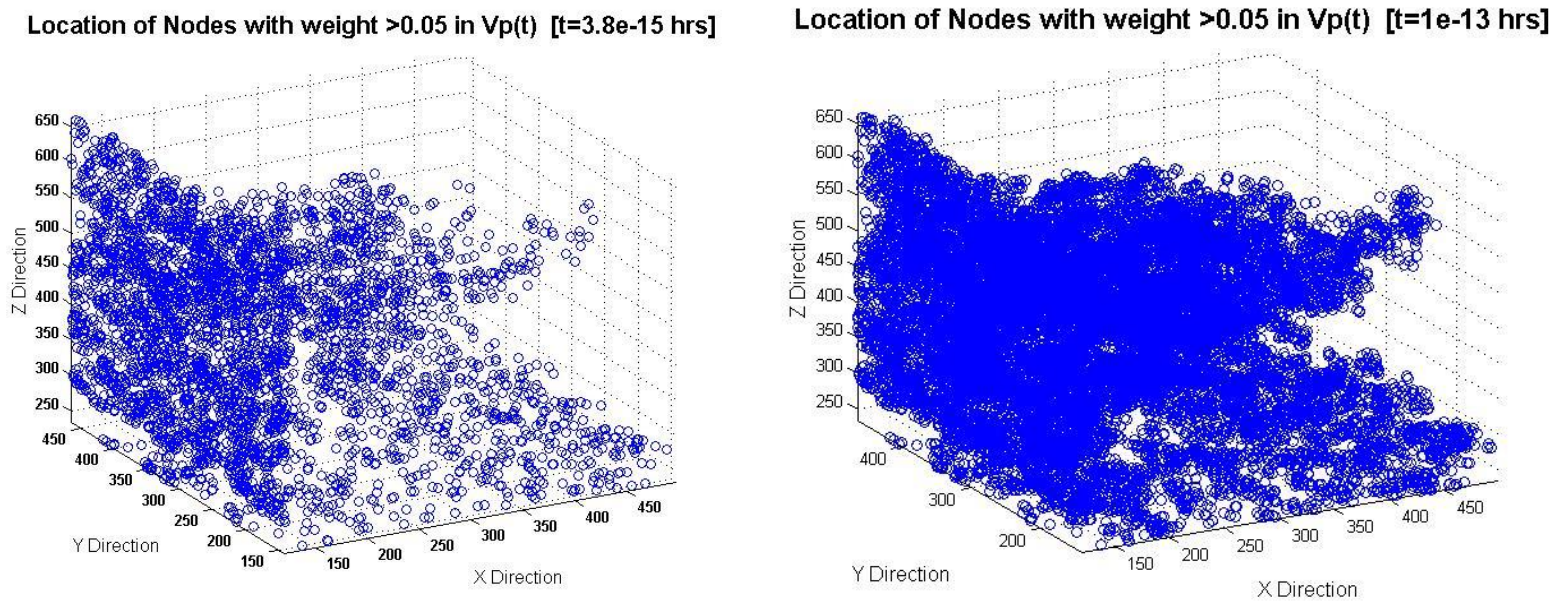

Figure 61 – Shows the location of the nodes in V_p (t) during the transient phase, for seed nodes on the YZ Plane.

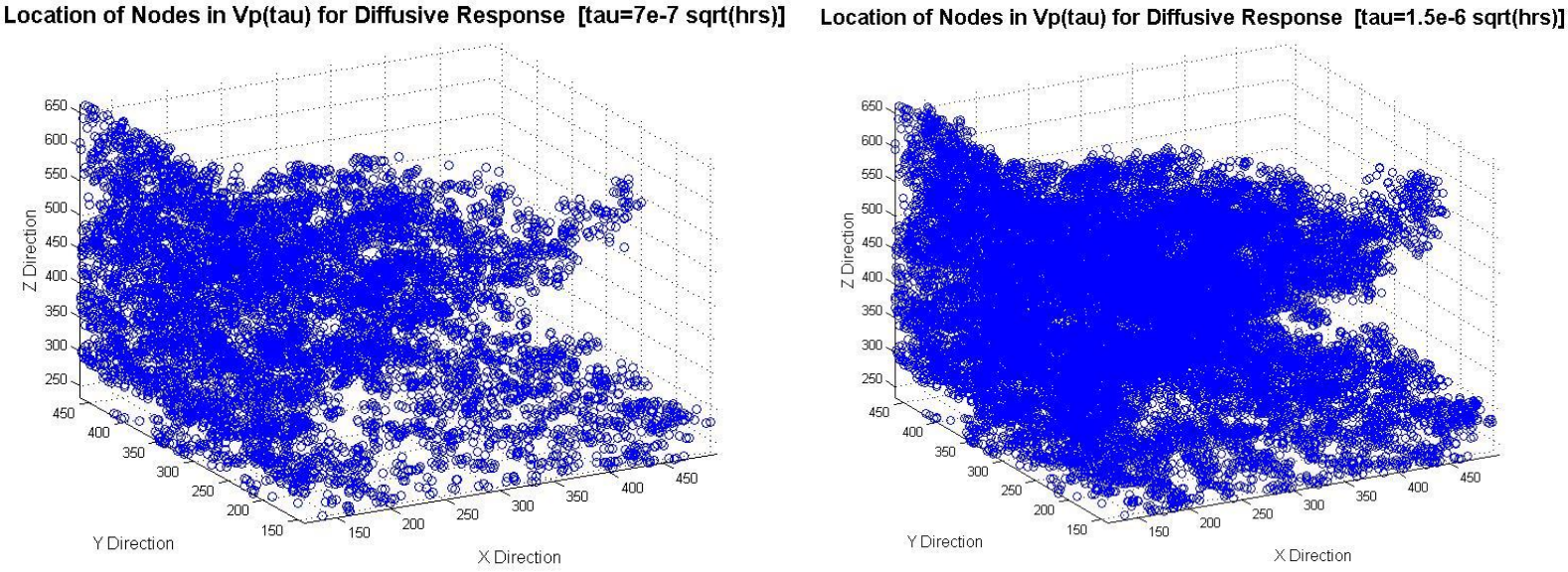

Figure 62 – Shows the location of the nodes in V_p (τ) during the transient phase, for seed nodes on the YZ Plane.

APPENDIX B

DRAINAGE VOLUMES FOR SEED NODES ON XZ PLANE

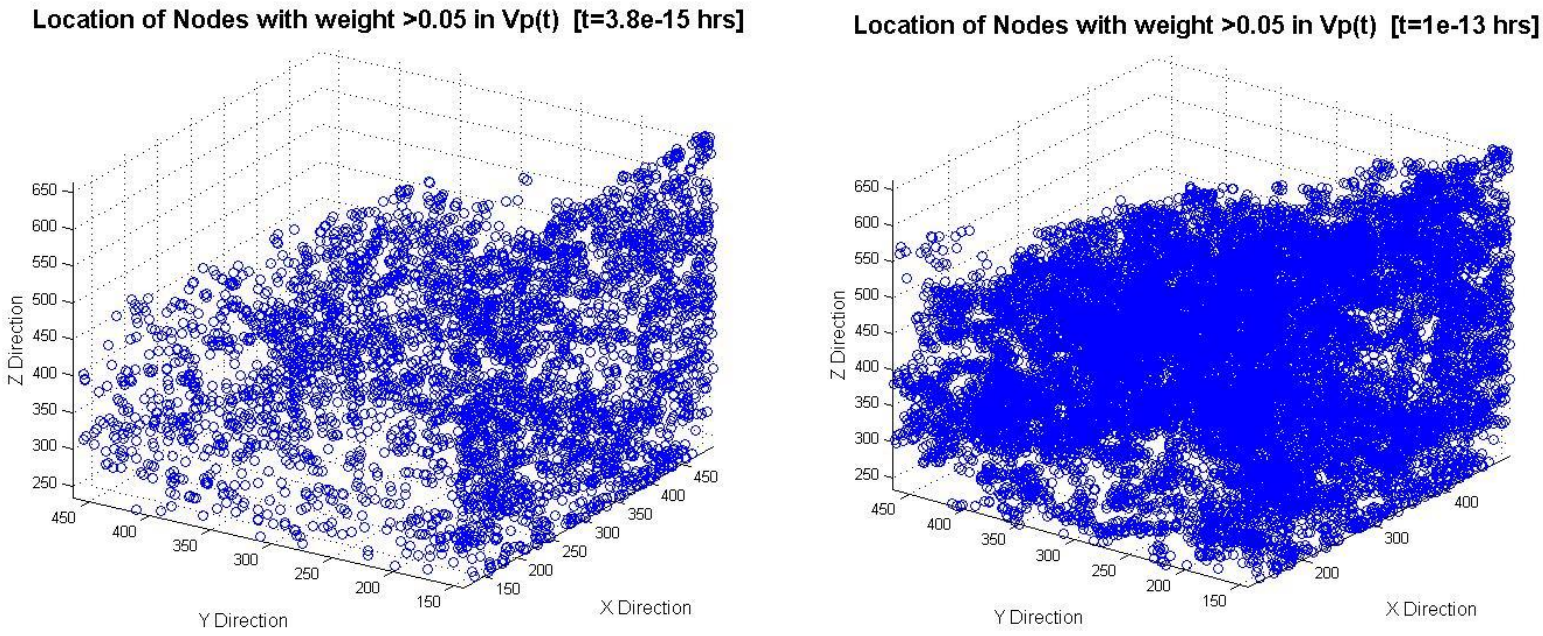

Figure 63 – Shows the location of the nodes in V_p (t) during the transient phase, for seed nodes on the XZ Plane.

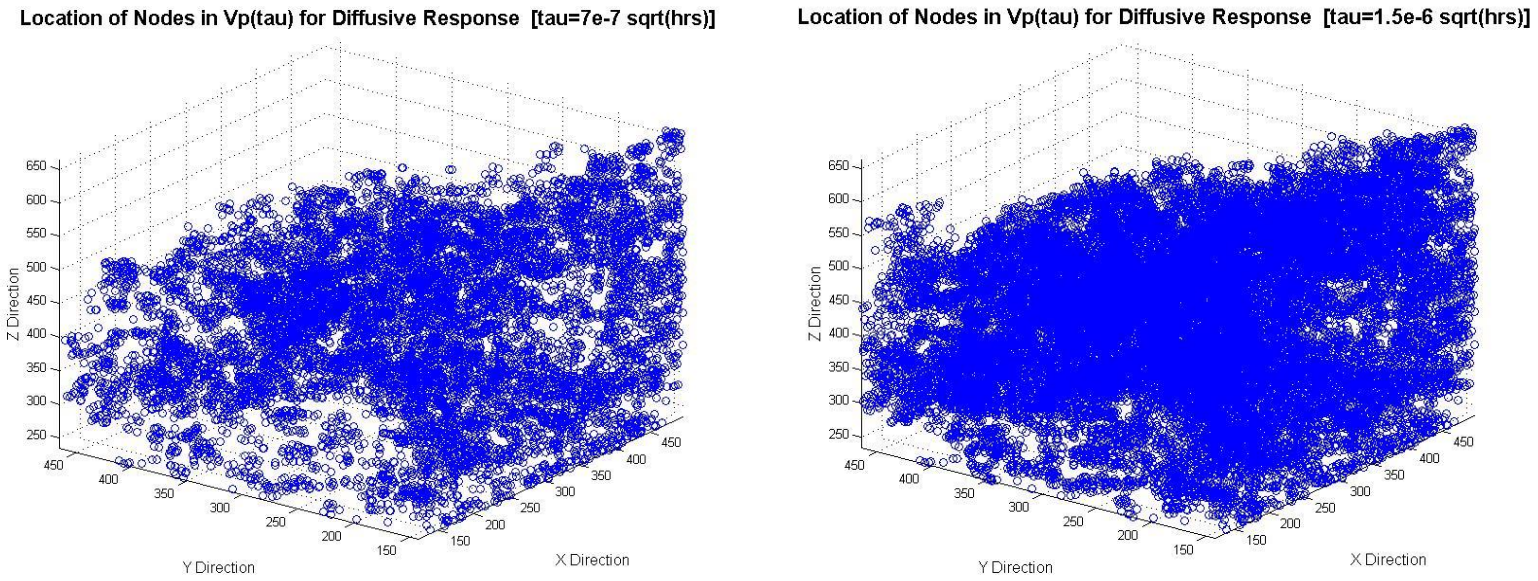

Figure 64 – Shows the location of the nodes in V_p (τ) during the transient phase, for seed nodes on the XZ Plane.

APPENDIX C

DRAINAGE VOLUMES FOR SEED NODES ON XY PLANE

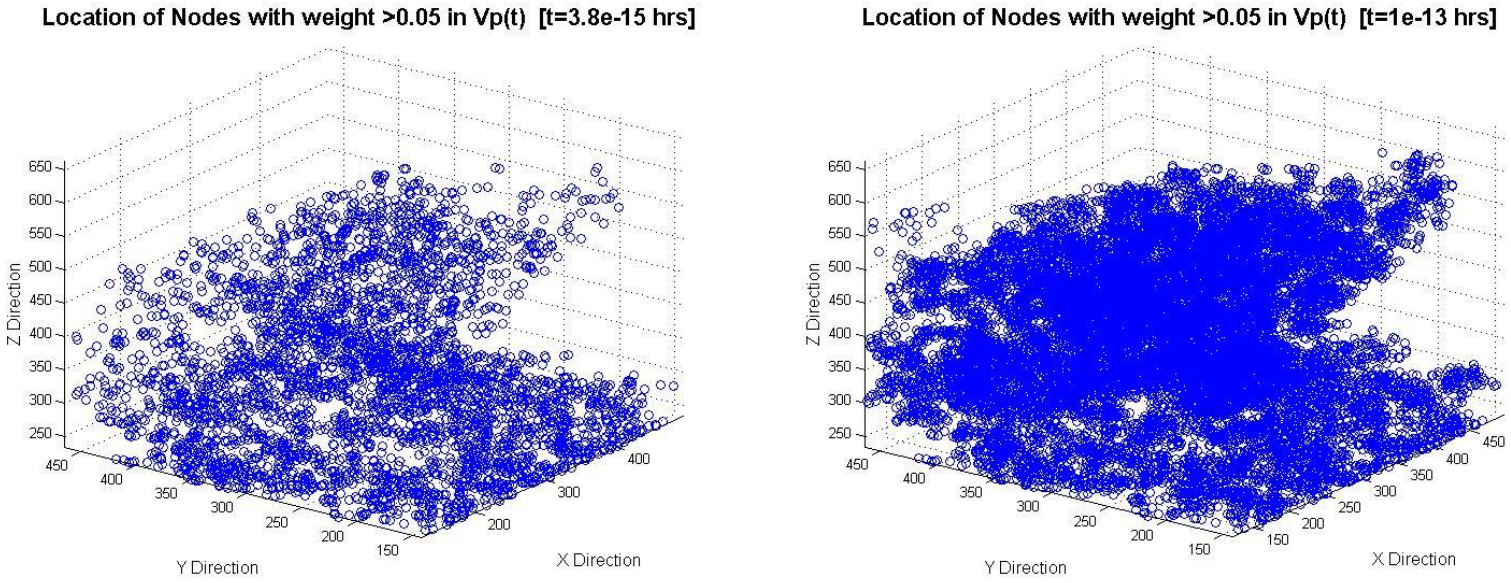

Figure 65 – Shows the location of the nodes in V_p (t) during the transient phase, for seed nodes on the XY Plane.

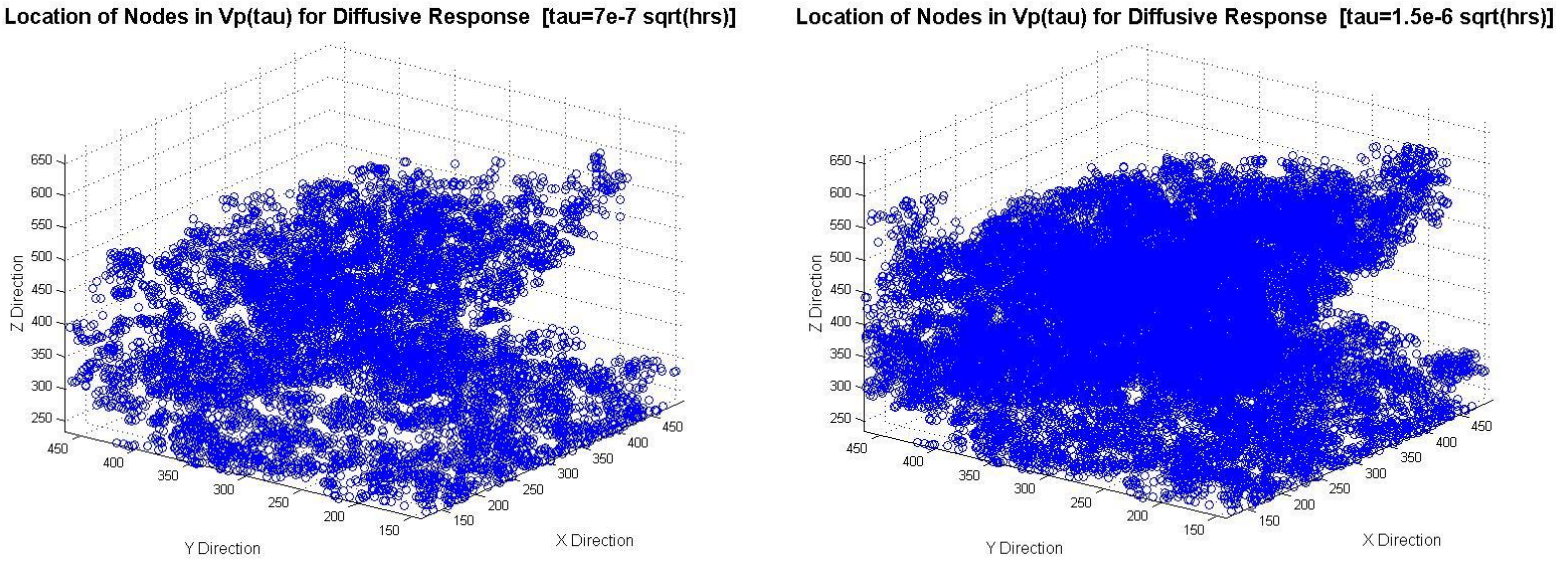

Figure 66 – Shows the location of the nodes in V_p (τ) during the transient phase, for seed nodes on the XY Plane.